UNIVERSITÀ
DEGLI STUDI
DI PADOVA

Sede Amministrativa: Università degli Studi di Padova
Dipartimento di Fisica e Astronomia "Galileo Galilei"

CORSO DI DOTTORATO DI RICERCA IN ASTRONOMIA
CICLO XXXII

HIGH SENSITIVITY STUDIES OF PULSAR WIND NEBULAE WITH CTA AND ASTRI MINI-ARRAY

Tesi redatta con il contributo finanziario dell'Istituto Nazionale di Astrofisica (INAF)

Coordinatore: Ch.mo Prof. Giampaolo Piotto
Supervisore: Dott. Luca Zampieri
Co-Supervisore: Dott.ssa Patrizia Caraveo

Dottorando: Michele Fiori

Abstract

PhD Thesis

High Sensitivity Studies of Pulsar Wind Nebulae with CTA and ASTRI Mini-array

Michele Fiori

In this Thesis, I present some perspective studies of a particular class of Galactic sources, the Pulsar Wind Nebulae (PWNe), in the most energetic part of the electromagnetic spectrum, the Very-High-Energy γ-rays. These sources represent the most numerous class of identified Galactic VHE γ-ray sources. They are highly magnetized nebulae powered by young and energetic pulsars. Inside them, charged particles are effectively accelerated to very high energies emitting photons up to $\sim$ 100 TeV. This investigation aims at assessing the capabilities of observing these sources with the future Imaging Atmospheric Cherenkov Telescopes (IACTs): The Cherenkov Telescope Array (CTA) and the ASTRI Mini-array. These facilities will be used for testing the various theoretical models of the γ-ray emission from these powerful sources. To assess the capabilities of CTA and the ASTRI Mini-array I have simulated and analyzed two young PWNe: SNR G0.9+0.1 and MSH 15-52. To better understand this class of objects and to make predictions on the shape at the VHE part of their spectrum, a one-zone time-dependent leptonic model has been implemented. In this model, the temporal evolution of the leptonic population is computed taking into account the continuous input of energy from the central pulsar and the interaction of the nebula with the surrounding ejecta of the Supernova Remnant (SNR). I have also carried out a detailed study of the systematic uncertainties that affect the estimate of the spectral parameters for observations with the CTA South array. In the context of the ASTRI Mini-array, I worked on testing the data analysis chain, simulating the same sources mentioned above. The purpose of this work was to select the most interesting targets for future observations and to test the performance of the array. A preliminary list of PWNe that could be studied from the Northern hemisphere with the ASTRI Mini-array is also reported.

Acknowledgments

I have received a great deal of support and assistance in carrying out this work.

First of all, I would like to thank my supervisor, Dr. Luca Zampieri, whose experience, competence and professionalism have been invaluable for my learning process. This goal has been reached also, and mainly, thanks to his wise guidance.

A special thanks goes to my co-supervisor, Dr. Patrizia Caraveo, for her useful comments.

I would also like to thank the external referees of this Thesis, Dr. Elena Amato and Dr. Roberta Zanin, for their comments and suggestions that certainly helped to improve the final outcome of my work.

Another person to whom I am very thankful is Dr. Aleksandr Burtovoi. Without his patience in the listening to all my doubts and problems and his ability to solve them this work would never have been finished in just three years. I would also like to thank Dr. Cornelia Arcaro for helping me finish all those analyses that I would never have had time to complete.

Outside the working context, there are still many people who I need to thank. First of all, my girlfriend Camilla who has always believed in me and supported me throughout this adventure. A big thanks also goes to all my friends that in these years have remained close to me even if I was physically (and mentally) far away.

Last but not least, my family. They have always believed in me and in my abilities and have never questioned my life choices, even when these choices have taken me far from home.

Thank you all for everything!

Contents

List of Figures

List of Tables

Chapter 1

Introduction

γ-ray astrophysics is a relatively new field for Astronomy. In order to obtain the first direct measurements of γ-rays from a celestial source astronomers had to wait the launch of the first detectors on balloons or satellites that could be placed above all, or most of, the atmosphere. The first detection of a Very-High-Energy (VHE) γ-ray source from the ground, with a Cherenkov telescope, had to wait even more, until 1989, with the detection of the Crab Nebula (Weekes et al. 1989).

Nowadays, VHE γ-ray Astronomy is growing quickly thanks to the current generation of imaging Cherenkov telescopes, like MAGIC (Aleksić et al. 2016), VERITAS (Park & VERITAS Collaboration 2015) and HESS (Hinton & the HESS Collaboration 2004; Hofverberg et al. 2013), and the current generation of water Cherenkov detectors, like HAWC (Abeysekara et al. 2013) and the Pierre Auger Observatory (Pierre Auger Collaboration et al. 2008). The VHE sources known to date are ~ 220 (Wakely & Horan 2008) and this number has steadily increased in the last few years. With the next generation of instruments, like the CTA (Hinton et al. 2013) and the ASTRI Mini-array (Pareschi et al. 2013), this number is expected to increase further.

VHE γ-rays originate in nuclear decay processes, nuclear interactions, and interactions in strong magnetic fields. The study of the sources that emit γ-rays offers a direct view of the most violent processes and the most powerful accelerators in the Universe. One class of these extreme emitters are the Pulsar Wind Nebulae, sources where particles are efficiently accelerated and confined inside a nebula. Accelerated leptons interact with magnetic fields and low-energy radiations fields resulting in the production of non-thermal

radiation up to $\sim$ 100 TeV (Rieger et al. 2013).

In this chapter I will briefly review the field of VHE astrophysics (in Section 1.1), the techniques for the detection of γ-rays from the ground (in Section 1.2) and the main projects for the next generation of imaging Cherenkov telescopes (the CTA in Section 1.3 and the ASTRI Mini-array in Section 1.4). In Chapter 2 I provide an introduction to the main physical processes that give origin to the emission observed in PWNe.

1.1 Very-High-Energy Astrophysics

Astrophysicists consider as γ-rays all the photons with energies greater than about 100 keV. The most energetic photons of the electromagnetic spectrum, above 100 GeV, are referred to as Very-High-Energy (VHE) γ-rays. VHE photons can be detected from Earth using the optical Cherenkov radiation (see section 1.2). The photons between $\sim$ 100 keV and $\sim 10 - 100$ GeV can be observed only from space, as in the atmosphere they are absorbed because of the photoelectric effect, Compton scattering and pair production (Longair 2011).

1.1.1 Cosmic-rays

Cosmic-rays (CRs) are charged particles and γ-ray photons that collide with the Earth atmosphere from all directions in space. The discovery of CRs is historically attributed to Victor Hess, who measured the increasing ionization of the atmosphere with increasing altitude using a balloon (Hess 1912). However, this was not the first evidence of CRs since both Theodor Wulf in 1909 (Wulf 1909) and Domenico Pacini in 1912 (Pacini 1912) performed measurements of the ionization of air or water as a function of height/depth from sea level. The CRs are divided into two categories, the primary CRs and the secondary CRs. The primary CRs are those that come directly from space and hit the atmosphere generating the secondary CRs. The majority of the primary CRs are made by protons and electrons. Only a small part of these CRs are γ-ray photons.

The isotropic spectrum of primary CRs has been measured since the realization of the first particle detectors mounted on satellites in the early '60s. The shape of this spectrum is well described with a power law with an index around 3 on average. Figure

1.1 (Evoli 2018) shows the CRs spectrum. The spectrum spans from 10^9 eV to more than 10^{20} eV. At lower energies ($< 10^{10}$ eV) the dominant contribution comes from the solar wind. Below the so-called "knee" ($\sim 10^15$ eV) the spectrum is dominated by the emission of astrophysical sources in our Galaxy while above it the dominant contribution is of extragalactic origin (De Angelis & Pimenta 2018). At even higher energies another change in slope is observed, the "ankle" ($\sim 10^18$ eV). The origin of the "ankle" is still not fully understood.

1.1.2 VHE sources

VHE astrophysics grew significantly only in the very last few years. The reason is that at these energies the fluxes are low and the relatively high background of other types of CRs makes the detection of TeV γ-ray photons quite difficult. The first experiment that successfully detected an astrophysical source, at TeV energies, is the 10 meter Whipple observatory in 1989, that observed the VHE emission coming from the Crab Nebula (Weekes et al. 1989). Since then the capabilities to detect and to study VHE emitting sources has rapidly grown, thanks to the imaging atmospheric Cherenkov telescope (IACT) technique (see Figure 1.2). In section 1.2 we will briefly introduce this technique and the major current and future experiments.

The VHE sky nowadays counts more than 200 sources. The mechanisms that can produce γ-rays in these sources are of leptonic or hadronic (or both) origin. The leptonic mechanisms (Longair 2011) are Bremsstrahlung emission (for extremely relativistic particles), Inverse Compton (IC) emission and Synchrotron-Self-Compton (SSC) emission. The hadronic mechanisms are mostly related to the decay of pion π^0 that can produce a $\gamma\gamma$ pair (Cui 2009).

Typical bright sources at TeV energies are Pulsars, Pulsar Wind Nebulae (PWNe, see section 2), Supernova Remnants (SNR), TeV binary systems, blazars, radio galaxies, and Starburst galaxies (Rieger et al. 2013). Here we briefly describe the γ-ray properties of these sources.

- **Pulsars**
  Pulsars are highly magnetized and rapidly rotating Neutron Stars (NSs). Most of the rotational energy of the pulsar is converted in Poynting flux, while a small fraction

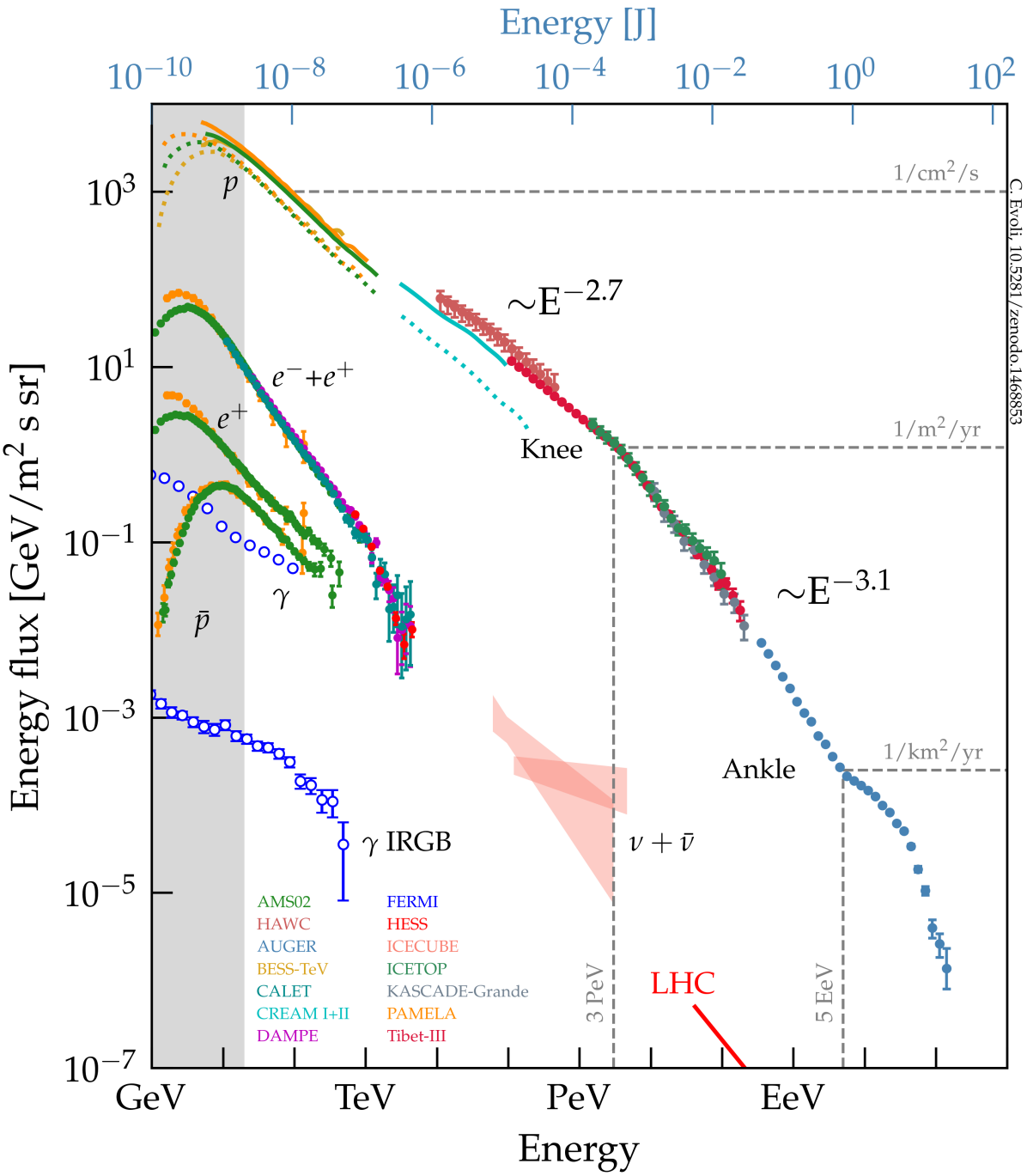

Figure 1.1: CRs spectrum as measured on Earth (Evoli 2018). The contribution of protons (p), electrons (e^-), positrons (e^+), antiprotons ($\bar{p}$) and photons at low energy are also reported.

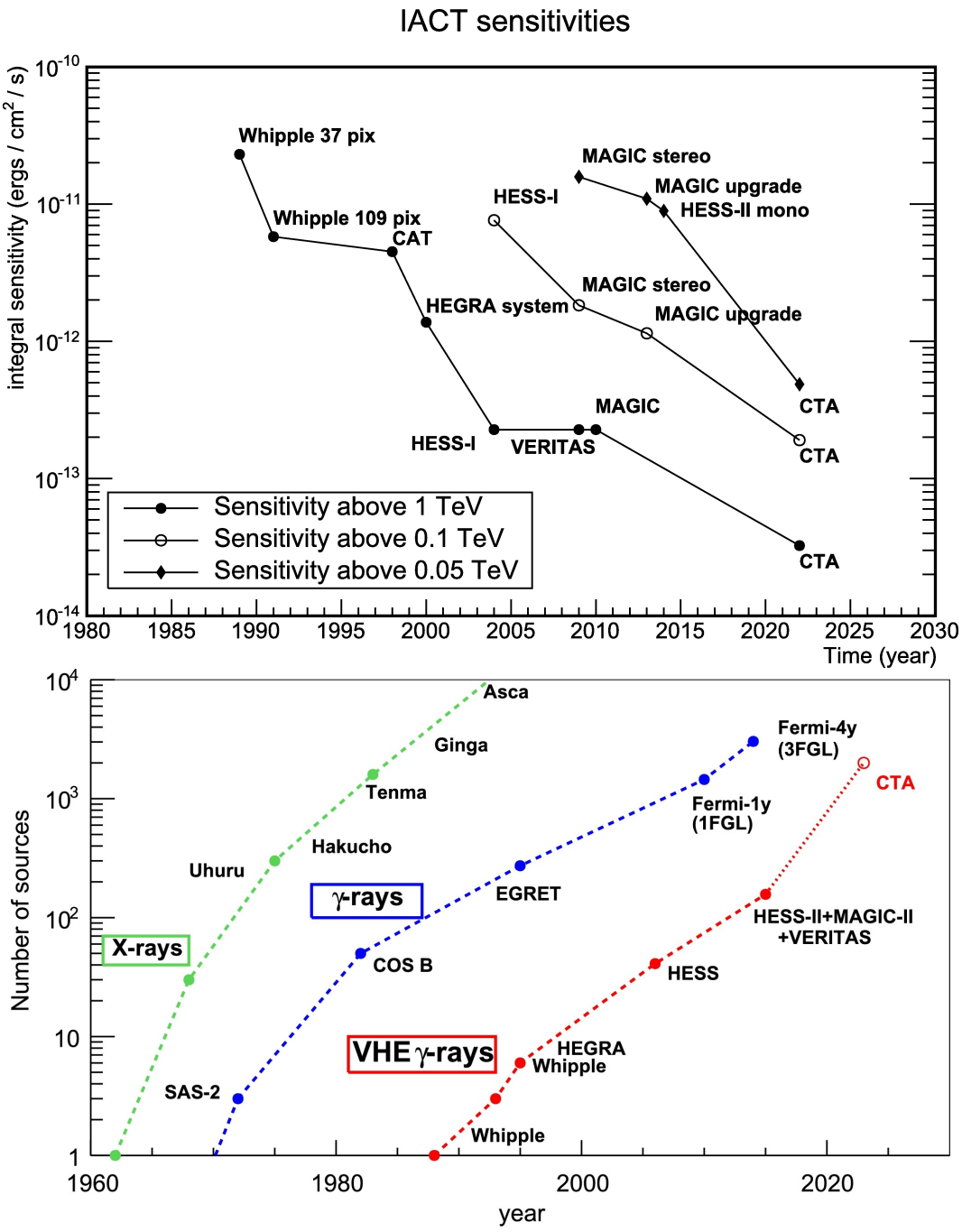

Figure 1.2: Sensitivity improvement for ground-based detection of astrophysical sources (de Naurois & Mazin 2015). The first panel is shown the improvement of the integral sensitivity with IACTs after the first detection in 1989 (Weekes et al. 1989) at different energy thresholds. The lower panel is shown the number of discovered sources compared to the ones discovered in the X-rays and in the lower energy γ-rays.

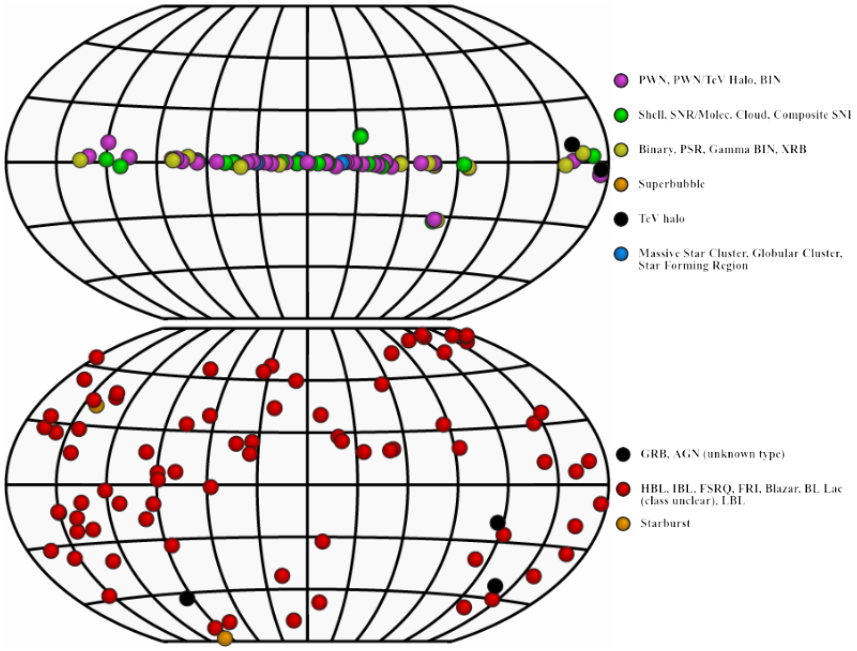

Figure 1.3: Known sources at TeV energies from the TeVCat catalog (Wakely & Horan 2008). Galactic sources are in the upper panel, while extragalactic sources are in the lower panel.

goes into kinetic energy of accelerated electrons and positrons. The acceleration of these particles near the magnetosphere is believed to be the mechanism that produces the pulsed emission seen in γ-rays (Muslimov & Harding 2003; Cheng et al. 2000; Coroniti 1990). *Fermi*-LAT observed about 230 pulsars at energies above 100 MeV (Fermi-LAT collaboration 2019a). 12 of these γ-ray pulsars show pulsations at $E > 25$ MeV (Ackermann et al. 2013) but only 3 out of 12 have been observed at even higher energies with IACTs, the Crab Pulsar (VERITAS Collaboration et al. 2011), the Geminga Pulsar (López Moya 2019) and the Vela Pulsar (H. E. S. S. Collaboration et al. 2018a). However, in a recent work Burtovoi et al. (2017) showed that 8 out of the 12 pulsars could possibly be detected with the future generation of IACTs.

- **Pulsar Wind Nebulae**

  PWNe are very bright TeV sources. Inside these nebulae leptons, coming from the pulsar magnetosphere, are accelerated up to relativistic velocities, and the interaction with magnetic and radiation fields produces non-thermal radiation up to 100 TeV. PWNe will be extensively discussed in section 2.

- **Supernova Remnants**
  Supernova (SN) explosions occurring at the end of the life of massive stars generate ejecta that expands into the surrounding medium (Janka et al. 2007; Müller 2017). Particles are accelerated at the shock front of the SNR (theory of diffusive shock acceleration; Blandford & Eichler 1987) and interact with the ambient medium, giving origin to non-thermal emission. TeV emission allows a more unbiased study of the particle acceleration since it does not depend on the magnetic field, at variance with the X-ray emission. Comparing the TeV flux to the flux in other energy bands provides a crucial means to distinguish the contribution of the leptonic component from that of the hadronic component in the emission from the SNR shell (Nakamori et al. 2015). The luminosity of SNRs at TeV energies is maximum at around 10^3-10^4 years after the supernova explosion.

- **TeV binary systems** In particular cases, some X-ray binary systems can emit radiation up to TeV energies. X-ray binaries (Tauris & van den Heuvel 2006) are objects composed by an accreting compact object (either a NS or a BH) and a donor star, that can be a low-mass star (Low-Mass X-ray Binaries; LMXBs) or a high-mass star (High-Mass X-ray Binaries; HMXBs). TeV emission can arise from the jet in the system (*microquasar* scenario; see e.g. Khangulyan et al. 2008) or from the interaction between the pulsar wind and the companion star (see e.g. Sierpowska-Bartosik & Torres 2008). Only a few objects are known to emit at TeV energies nowadays, but more are likely to be discovered in the future thanks to CTA (Paredes et al. 2013).

- **Extra-galactic sources** The vast majority of TeV detected extra-galactic sources are Blazars (Prandini 2017). Blazars are a sub-class of Active Galactic Nuclei (AGN), sources where a Super-Massive Black Hole (SMBH) is fueled by an accretion disk and where a jet is launched in direction of the observer. Due to the extreme-relativistic regime of the particles in these jets, Doppler boosting induces a strong magnification of the flux from these sources. Studying the TeV emission can provide crucial information on the acceleration processes and the relative contribution of the leptonic and hadronic components in these sources (Boettcher 2010). Other extra-galactic sources are other types of AGNs (like radio galaxies), Starburst galaxies and γ-ray bursts (the first detection of a GRB at sub-TeV energies was done with MAGIC; GRB 190114C, Mirzoyan 2019). One important factor to remember

when studying distant sources at VHEs is the γ-ray horizon. VHE photons are known to interact with the less energetic photons (optical and infrared photons) of the Extra-galactic Background Light (EBL; Stecker et al. 1992). Depending on the energy of the TeV photons and on the distance of the source emitting it, there is a certain probability that the photon interacts with photons of the EBL creating an electron-positron pair. This means that for very distant objects ($z \gtrsim 1$) all the TeV photons are absorbed before reaching the Earth.

1.2 Ground-based γ-ray detection

The ground-based techniques for the observations of VHE γ-rays are based on the detection of secondary CRs, at variance with the space-based techniques where the satellite detects directly the primary CRs. The energetic range detectable depends on the technique and the properties of the detectors, but in total it goes from a few tens of GeV up to hundreds of TeV.

1.2.1 Cherenkov radiation

The physical process that permits the detection of secondary CRs at the ground is the Cherenkov radiation, discovered in 1934 (Cherenkov 1934). When a charged particle moves at speed higher then the velocity of light inside a medium, the so-called Cherenkov light is emitted. The light is emitted in a coherent cone with an opening angle θ (Figure 1.4; De Angelis & Pimenta 2018):

$$\cos\theta = \frac{c}{v \cdot n} \tag{1.1}$$

where n is the refractive index of the medium, c the speed of light in vacuum and v the velocity of the charged particle. The Cherenkov effect becomes important when the refractive index of the medium is $n > 1$ and the medium is transparent. In the visible band ($300 - 700$ nm) the Cherenkov emission is brighter in the ultraviolet region of the EM spectrum (the observed Cherenkov light is blue) since the number of photons emitted per unit frequency and unit length is proportional to $1/\lambda^2$. The emitted photons are ~ 40/m in air and ~ 500/cm in water.

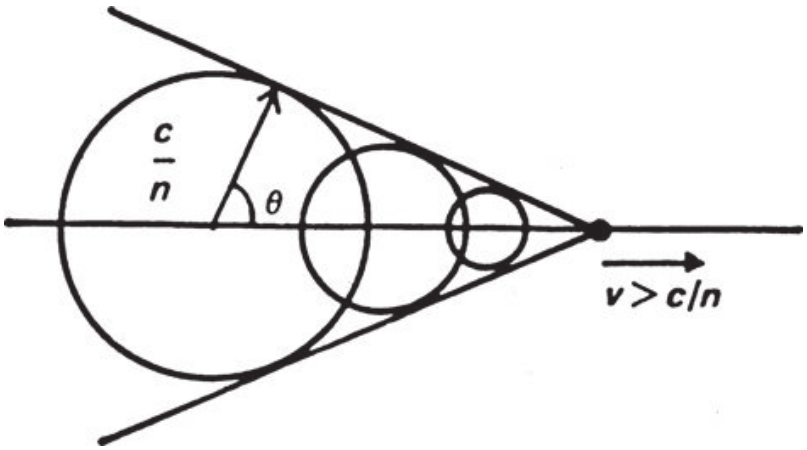

Figure 1.4: Coherent radiation of a charged particle moving at constant velocity ($v > c/n$) through a medium with refractive index n (Longair 2011).

1.2.2 Extensive Air Showers

When a primary CR enters in the atmosphere the interaction between the high-energy particle and a nucleus in the air produces a shower of secondary particles (Engel et al. 2011), that is called Extensive Air Shower (EAS).

In the case of VHE photons as primary CRs hitting the atmosphere an EM shower is generated. When a γ-ray photon hits a nucleus it can create an $e^+ - e^-$ pair. If the electrons and positrons have enough energy, they can emit radiation by bremsstrahlung. These photons can undergo again pair creation and so on. Finally, a shower made by electrons, positrons and photons is produced (see left panel in Figure 1.5). The first interaction generally happens at 20-30 km of altitude in the atmosphere and is not dependent on the energy of the incoming photon. These EM showers are roughly symmetric with respect to the incident direction of the progenitor photons (Lopez-Coto 2015).

In the case of hadrons as primary CRs hitting the atmosphere a hadronic shower is generated. In this case, the first interaction is caused by the strong force and mostly heavy baryons are created. In the $\sim 90\%$ of the cases a pion is created, while in the $\sim 10\%$ of the cases a kaon is produced. These secondary hadrons undergo further collisions. The process is stopped when the energy per particle reaches the minimum energy required to generate a pion ($\sim$ 1 GeV). Inside the shower, the pions can also decay into photons, electrons, positrons, and muons producing secondary showers (Lopez-Coto 2015).

In Figure 1.5 we show the EAS generated by a γ-ray photon compared to the EAS

generated by a hadron. Comparing a hadron and a γ-ray photon with the same energy, the hadronic shower is wider.

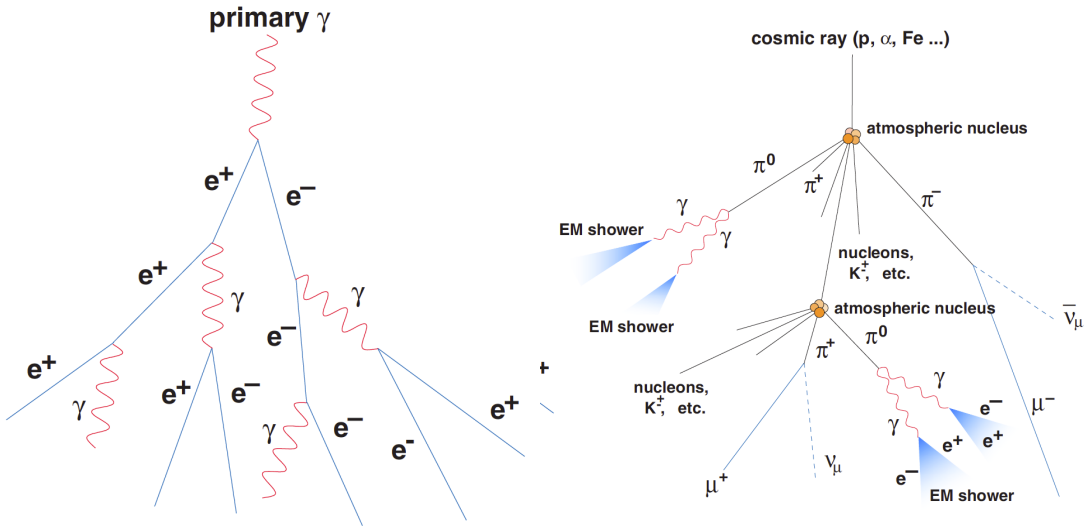

Figure 1.5: Schematic view of an EASs in case the primary CR is a photon (left) or a hadron (right) (Wagner 2006).

The particles generated in the EASs are highly relativistic. This means that they can move through the atmosphere at speed higher than the speed of light in that medium, and thus produce Cherenkov light. The light pool at the ground of a shower initiated by a VHE photon of 1 TeV is of about 120 m, with almost constant photon density. At 2000 m above sea level this density is of about 150 photons per square meter (De Angelis & Pimenta 2018).

1.2.3 Ground-based detectors

There are two different types of ground-based detectors (de Naurois & Mazin 2015). The first type directly detects the shower tail measuring the particles that reach the ground. The basic idea is to sample the charged particles of EASs using arrays of detectors spread on a very large area. The most successful way of revealing such particles is through a water Cherenkov detector, where the charged particles enter in the water producing Cherenkov light. This flashes of light are then detected through photomultipliers (Di Sciascio 2019). The weaknesses of this technique are that the energy detection threshold is high (only the most energetic CRs can induce a shower that reaches the ground) and that the spatial

resolution is quite low. However, the duty cycle of these instruments can be almost 100% and they have a very large field of view (Holder 2014).

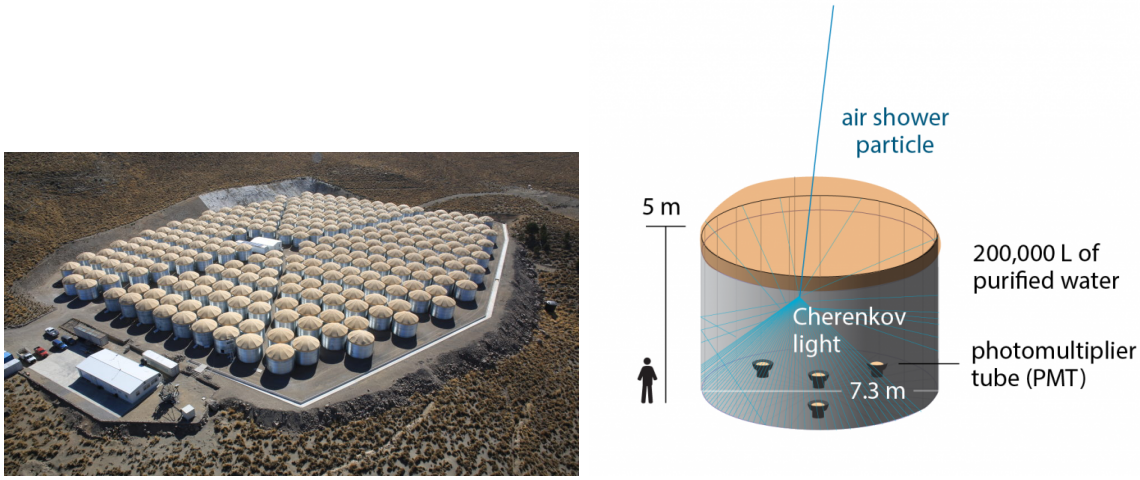

Figure 1.6: The High Altitude Water Cherenkov (HAWC) detector (Abeysekara et al. 2013) for detecting EASs in water (Di Sciascio 2019).

Imaging Atmospheric Cherenkov Telescopes

The second way of detecting VHE γ-rays is to catch with IACTs the Cherenkov light of showers that do not reach the ground. With this technique, optical telescopes are used to catch the very faint and fast Cherenkov flashes of light produced by the EASs. Later, the arrival directions and the energies of the incident primary CRs are reconstructed from the distribution of the detected flashes.

The telescopes are typically made with a parabolic or a spherical mirror that can directly focus the photons onto a Photo-Multiplier Tube (PMT). The size of the mirror of these telescopes is of the order of 10 meters since the intensity of the light coming from the shower is very low. The duration of the signal is very short (less than 30 ms) and so the detector needs to be very fast. The duty cycle is quite low compared to a water Cherenkov detector (around $10 - 15\%$) since the background has to be low and therefore the telescopes work only in moonless nights. However, this technique has several advantages: the energy range is very extended (down to ~ 100 GeV); it is much easier to distinguish between hadronic and EM showers (the shape of the Cherenkov light detected at ground depends on the particle species); the angular resolution is quite good (around

0.1°); the energy resolution ($\sim 15\%$) and the sensitivity are significantly better than those of water detectors (Spurio 2018).

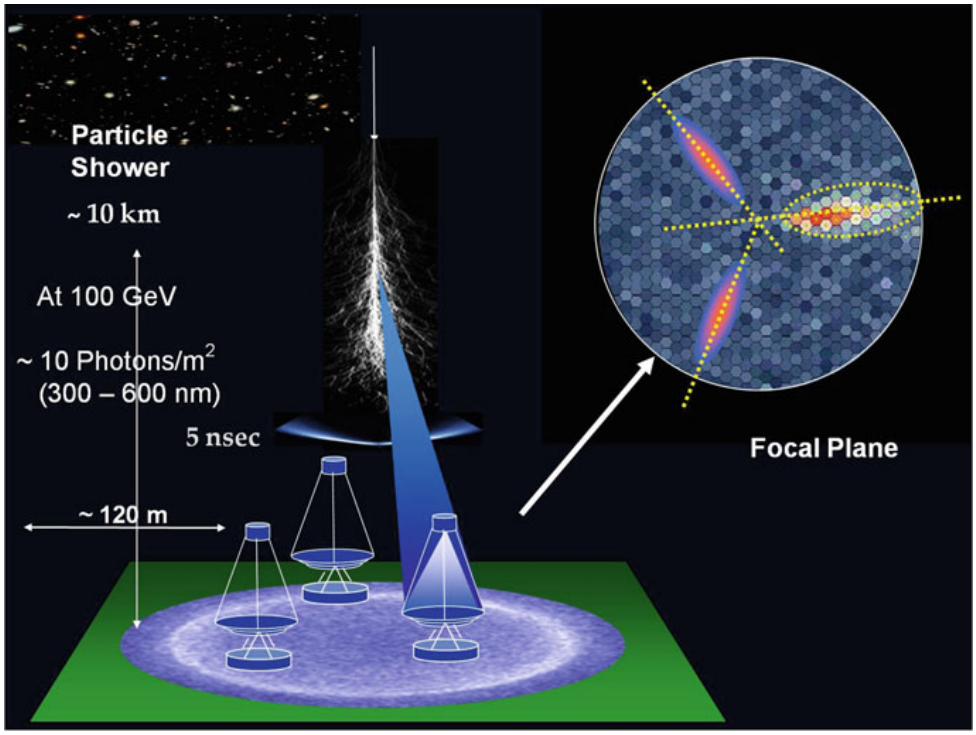

Figure 1.7: Scheme of stereoscopic imaging atmospheric Cherenkov telescopes (Spurio 2018).

The best results are obtained using more telescopes. With two or more telescopes that detect a flash from the same shower, it is possible to do a better reconstruction of the arrival direction and the type of particle signal, discarding events like those produced by single muons (Hillas 2013). This is how the major IACTs facilities work nowadays.

The main Cherenkov telescopes arrays are (Funk 2015):

- The Major Atmospheric Gamma-ray Imaging Cherenkov (MAGIC; Aleksić et al. 2016) telescope, located in La Palma (Canaries Islands) at the observatory of the Roque de los Muchachos at an altitude of $\sim$ 2400 m. It consists of two telescopes with a diameter of $\sim$ 17 m and covers an energy range between 50 GeV and 30 TeV.
- The High Energy Stereoscopic System (HESS; Hinton & the HESS Collaboration 2004), located in the Khomas Highland (Namibia) at an altitude of $\sim$ 1800 m. Originally the system had four telescopes with a diameter of $\sim$ 12 m and a low

energy threshold of $\sim$ 100 GeV. Later a fifth telescope was added to the array (HESS II; Hofverberg et al. 2013). The new telescope has a diameter of $\sim$ 28 m and lowered the energy threshold to $\sim$ 30 GeV.

- The Very Energetic Radiation Imaging Telescope Array System (VERITAS; Park & VERITAS Collaboration 2015), located in Mount Hopkins (Arizona, USA) at an altitude of $\sim$ 1300 m. It consists of four telescopes with a diameter of 12 m (as in the phase I of HESS) and has a lower energy threshold of $\sim$ 85 GeV.

All the know-how developed for the construction, the implementation and utilization of these facilities is now being transferred to the production of a new and ambitious project, the Cherenkov Telescope Array (CTA).

1.3 The Cherenkov Telescope Array

The leading project for the next generation of ground-based observatories at VHE γ-rays is the Cherenkov Telescope Array (CTA)[1]. It will consist of more than 100 telescopes in the two hemispheres and will have unprecedented sensitivity and energy coverage in the VHE γ-rays (Ong & CTA Consortium 2017).

Although in recent years the field of the VHE astrophysics has made great progress thanks to the facilities presented in the previous section, a further improvement in sensitivity is needed to increase the number of sources that can be detected and to perform detailed morphological studies of extended sources. Also, the energy threshold needs to be lowered to observe more extra-galactic sources and to enlarge the pool of the ground-based detected γ-ray pulsars. Furthermore, detecting transient sources (like GRBs) requires an instrument that can observe on shorter time-scales (Bigongiari & CTA Consortium 2016).

A worldwide consortium of scientists, about 1500 members from more than 200 institutes in 31 countries, is developing the CTA project. The project will consist of two arrays of Cherenkov telescopes, with various sizes, that will observe the whole sky and will have the wide energy range needed to study the most extreme processes in the Universe.

The CTA Observatory (CTAO) consists of two different arrays locations and two office

[1] www.cta-observatory.org/

Figure 1.8: The MAGIC (upper panel; credit: The MAGIC Collaboration), the HESS (mid panel; credit: The HESS Collaboration) and the VERITAS (lower panel; credit: The VERITAS Collaboration) facilities.

locations. The CTAO Headquarter is located in Bologna (Italy) while the Science Data Management Centre (SDMC) is located in Berlin-Zeuthen (Germany). The Northern array site will be in La Palma at the Observatory of the Roque de Los Muchachos (Canary Islands) at the same site of the MAGIC telescopes. The Southern array will be constructed in Chile in the Atacama desert, nearby to the European Southern Observatory (ESO) Paranal site. The two arrays will consist of a different number of telescopes.

In order to realize observatory that can cover an energy range between 10 GeV to 300 TeV, telescopes with different dish sizes are needed. The bigger telescopes provide the needed sensitivity at low energies, while the smaller ones, that cover a very big area (approximately a square kilometer), provide the sensitivity at high energies. The telescopes that will be constructed are (Acharya et al. 2013):

- **Large Size Telescopes (LSTs)**. These telescopes (4 for each array) will have a parabolic dish of 23 m diameter with a carbon-fiber structure and will be equipped with a PMT camera with 4.3 deg field of view (Mazin et al. 2017). Owing to the large size of the mirror the LSTs will be capable to catch the faint light coming from the lower energy CRs hitting the atmosphere. The best sensitivity of the LSTs will be in the energy range between 10-20 GeV and 150 GeV.

- **Medium Size Telescopes (MSTs)**. These telescopes (25 at CTA-South and 15 at CTA-North) will have a 12 m dish and a Davies-Cotton (Davies & Cotton 1957) design. They will be equipped with a PMT camera with a field of view of ~ 7.5 deg (Pühlhofer 2017). The best sensitivity of the MSTs will be in the energy range between 150 GeV and 5 TeV.

- **Small Size Telescopes (SSTs)**. Three prototypes are proposed for the SSTs. All of them have a primary dish of 4 m and a Silicon Photo-Multiplier (SiPM) camera with a field of view close to 10 deg. Two configurations (ASTRI and GCT) have a dual-mirror (Schwarzschild-Couder optical design) and one configuration (SST-1M) has a single mirror (Montaruli et al. 2015). Seventy telescopes will be installed at CTA-South, to study mostly Galactic sources, and will be sensitive in an energy range between 5 TeV and 300 TeV. These telescopes will also cover a very wide area on the ground (~ 4 km^2) to catch all the rare very high energy CRs that enter in the atmosphere.

The layout of the arrays were optimized to maximize the overall performances using

Monte Carlo simulations and considering the properties of the selected sites for CTA (Bernlöhr et al. 2013; Hassan et al. 2015; Hassan et al. 2017; Maier et al. 2017; Acharyya et al. 2019). In the North site, the array will consist of 4 LSTs and 15 MSTs with a configuration severely constrained by external factors (orography, roads, and buildings; Cumani et al. 2017). The South array will consist of 4 LSTs, 25 MSTs and 70 SSTs with a configuration optimized to cover uniformly an area of ~ 4 km^2 (Cumani et al. 2017). Figure 1.9 shows the layout of the two arrays (upper panels), the expected sensitivity limit for 50 hours observations with the two arrays (mid panel), and the expected angular resolution for the South array (lower panel) in comparison with the performances of the current generation of γ-ray observatories.

The CTA Consortium has defined a series of core programs to be addressed during the first ten years of operation of the two arrays. These core programs will be projects with a high scientific impact that can be accomplished only with a considerable amount of time. They are called Key Science Projects (KSPs; Hinton et al. 2013) and are excellent scientific cases for the γ-ray community and the wider community, that have a clear added value for the CTA project (CTA Consortium 2019). A detailed schedule of these KSPs has been already implemented to demonstrate the feasibility of the plan considering an approximate 40% of the shared observing time for ten years. The KSPs are the Dark Matter Program, the Galactic Center Survey, the Galactic Plane Survey, the Large Magellanic Cloud Survey, the Extragalactic Survey, Transients observation, the Cosmic-ray PeVatrons, the Star-Forming Systems, the Active Galactic Nuclei, and the Clusters of Galaxies (Vercellone 2017; Ong & CTA Consortium 2017).

1.4 The ASTRI Mini-array

Within the framework of the CTA Consortium, there are other collaborations working on the design of all the hardware and software that will be part of the CTA. This is because of the worldwide structure of the project and the enormous efforts needed to develop all the CTA sub-systems (telescopes, acquisition systems, managing and control infrastructures, software for the analysis of the data and much more). Among these collaborations there is one lead by the Istituto Nazionale di Astrofisica (INAF; Italy), that is developing one of the three SSTs prototypes, the "Astrofisica con Specchi a Tecnologia Replicante Italiana" project (ASTRI; Pareschi et al. 2013).

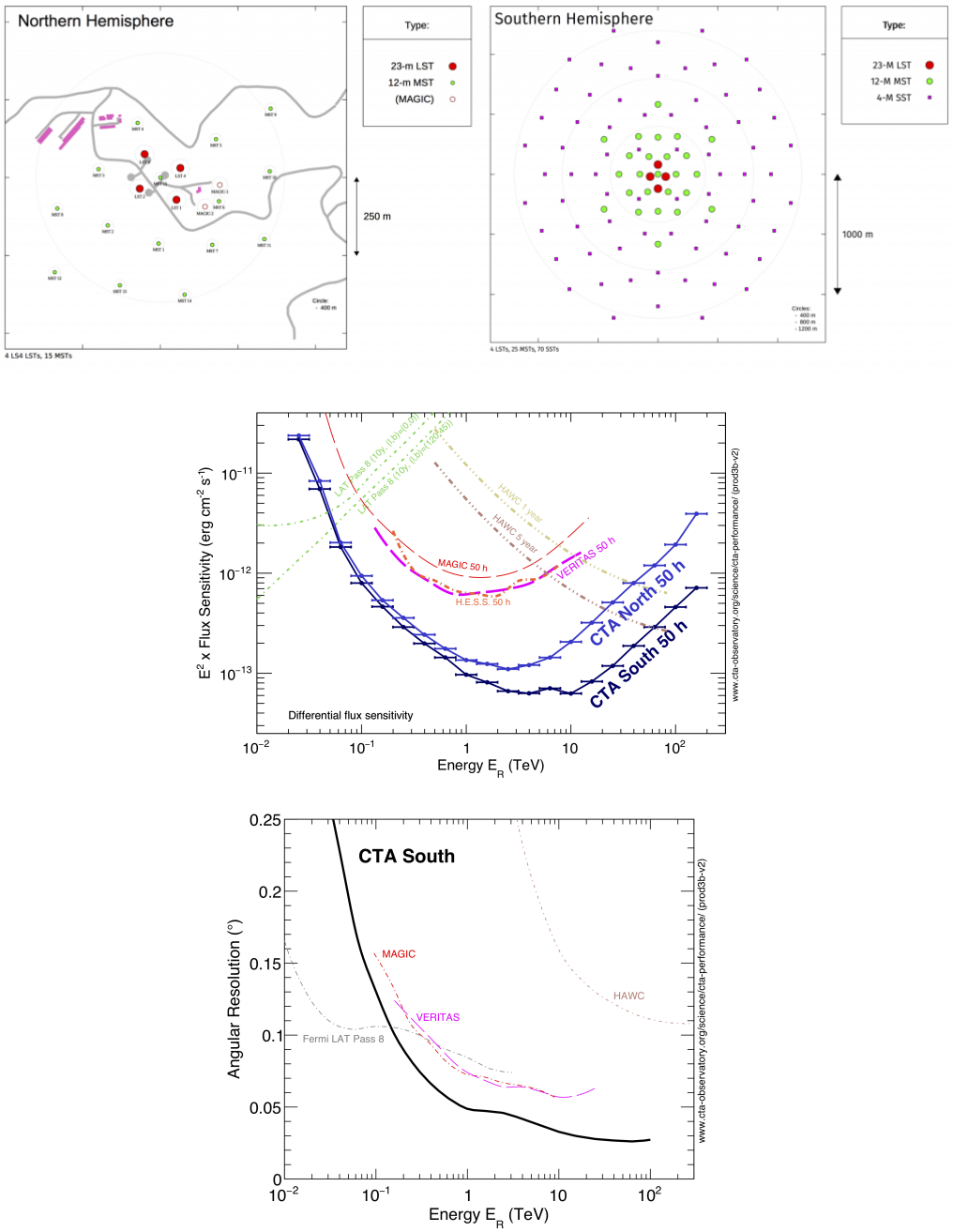

Figure 1.9: The layout of the two arrays (upper panels) and expected performances (mid and lower panels). The North site will consist of 4 LSTs and 15 SSTs while the South site will consist of 4 LSTs, 25 MSTs, and 70 SSTs (Acharyya et al. 2019). The sensitivity limits for both arrays and the angular resolution of CTA-South are compared to the performances of the current generation of γ-ray observatories (Fermi-LAT collaboration 2019b; Ahnen et al. 2015; Aleksi et al. 2016; Holler et al. 2015; VERITAS collaboration 2019; Abeysekara et al. 2017). Credit: The CTA Consortium.

The name ASTRI derives from the "Flagship Project" of the Italian Ministry of Education, University and Research (MIUR), tailored to the development of a replica technology for sensors and mirrors for γ-ray observations (La Palombara et al. 2013). The project aims at realizing an end-to-end prototype for the CTA SSTs, the ASTRI SST-2M (Maccarone & Astri Project 2017). The key feature of the ASTRI SST-2M is the dual-mirror modified Schwarzschild-Couder optical design (Vassiliev et al. 2007). This configuration is characterized by a very wide field-of-view ($\sim 10°$) and a much more compact structure compared to the single-mirror telescopes. The focal plane is curved and hosts a SiPM camera controlled by a fast front-end electronics (Scuderi 2018). The segmented primary dish has a diameter of 4.3 m, while the monolithic secondary has a diameter of 1.8 m.

Figure 1.10: The ASTRI SST-2M prototype (Pareschi 2016).

The prototype is nowadays installed and operational at Serra La Nave (Catania, Italy), on Mount Etna, and has already achieved important results. The first result is the demonstration of a uniform PSF across the focal plane in agreement with the specifications ($\sim$ 10 arcmin; Giro et al. 2017). The second result is the detection of the Crab Nebula, the first detection at TeV energies made by a Cherenkov telescope in a dual-mirror configuration[2] (Lombardi & The ASTRI Collaboration in prep.).

[2] www.cta-observatory.org/astri-detects-crab-at-tev-energies/

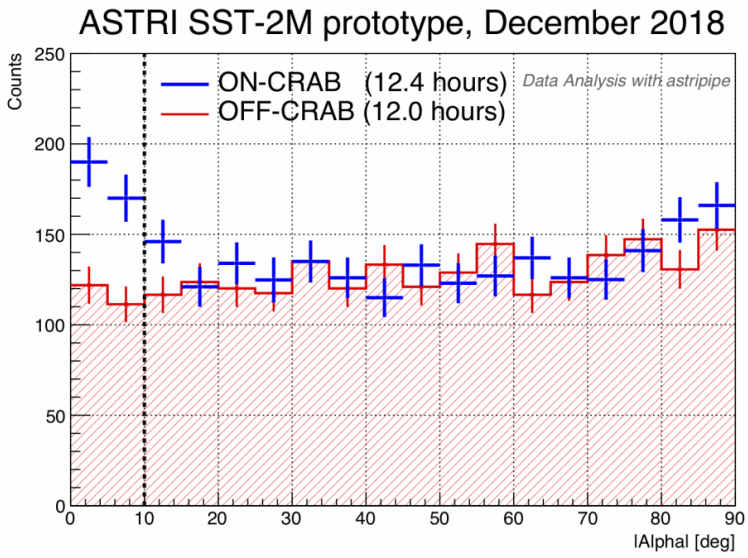

Figure 1.11: VHE counts as a function of declination for the ASTRI observation of the Crab Nebula. The comparison of the excess of counts in the direction of the Crab Nebula (blue points) versus the background (red points) shows that the source is detected. Credit: The ASTRI Collaboration.

The scope of the ASTRI prototype was to develop the hardware and the software for a fraction of the 70 SSTs for CTA-South. However, the CTAO council has decided that only one type of SST will be constructed to harmonize the array and reduce the number of sub-systems (CTA Consortium 2018). A recent resolution of the council informed that the project selected for all the 70 SSTs is the ASTRI telescope coupled with the CHEC camera (Brown et al. 2016), the camera developed for the GCT-SST project.

The next step for the ASTRI project is the implementation of a Mini-array of 9 telescopes (Scuderi 2019). The Mini-array will be of crucial importance to probe the technology and to test operational and maintenance procedure for the full CTA array. It will be useful also for comparing the performances of the array to the Monte Carlo simulations and to perform the first tests of stellar image reconstruction at sub-milliarcsec scale by means of intensity interferometry (for more information on stellar intensity interferometry with IACTs see for example Kieda & Matthews 2017; Kieda et al. 2019). Moreover, it will be possible to do early science while awaiting for the full CTA arrays.

While the ASTRI SSTs will be part of CTA South, it was recently dediced that the ASTRI Mini-array will be installed at the Observatorio del Teide (Canaries Islands,

Spain) in the Northern hemisphere[3].

The preliminary sensitivity curve of ASTRI Mini-array is shown in Figure 1.12. The sensitivity is computed from Monte Carlo simulations considering 9 telescopes with relative distances of ~ 250 m in a square layout and at the same altitude, but considering it located in the CTA South site (the sensitivity curve needs to be updated considering the new location of the Mini-array in the Northern hemisphere). Above 10 TeV the expected performances of the Mini-array are better than what is achievable nowadays with HESS. It will be possible to observe up to about 100 TeV with an energy resolution of $\sim 10-15\%$ (Lombardi et al. 2018).

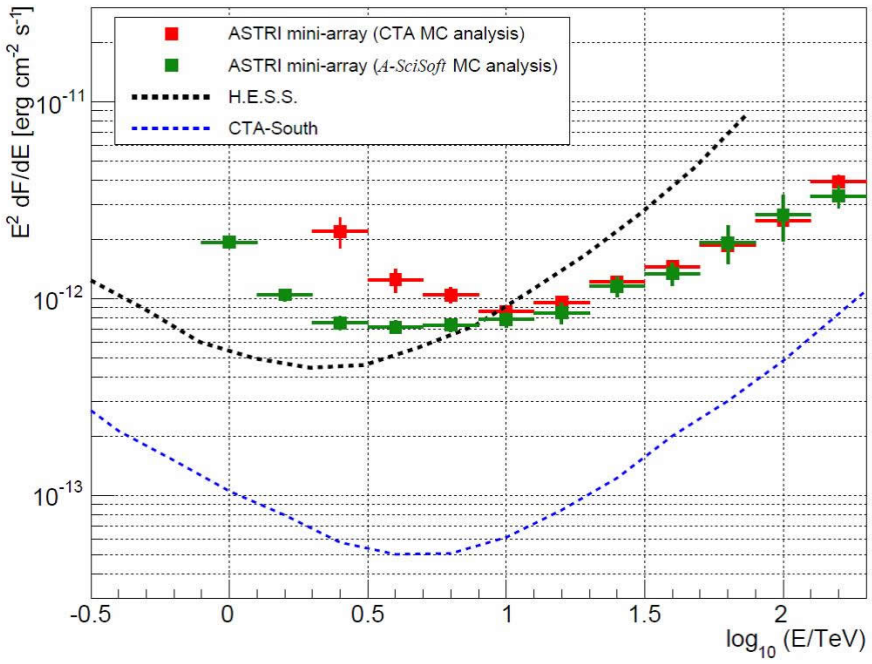

Figure 1.12: Preliminary sensitivity curve of the ASTRI Mini-array, compared to the sensitivity curve of HESS and CTA-South. The two curves for the ASTRI Mini-array were obtained by two groups that performed independent implementations of the MC analysis and adopted different low energy cuts (Scuderi 2018). However, the two curves are in good agreement above 10 TeV. Credit: The ASTRI Collaboration.

The science case for the ASTRI Mini-array is similar to the CTA science case. Bright TeV sources will be studied in great detail with an angular resolution of a few arcmins.

[3] www.inaf.it/en/inaf-news/astri-a-new-pathfinder-of-the-arrays-of-cherenkov-telescopes

Primary targets will be PWNe, SNRs, Galactic binaries, the Galactic Center, extreme blazars and well-known BL Lac objects. All these sources will be observed in a previously unexplored energy range (Vercellone et al. 2013).

1.5 This Thesis

The most numerous class of identified Galactic VHE γ-ray sources are PWNe. As discussed in the next Chapter, PWNe are important laboratories to test extreme physical processes, like the acceleration of charged particles to relativistic energies and the diffusion of such particles inside magnetic fields. Moreover, they are of crucial importance to understand how the rotational energy of a pulsar is transferred to its surrounding medium.

This Thesis is centered on the prospects for the study of PWNe with CTA and the ASTRI Mini-array, with the aim of improving our knowledge of the VHE emission of these sources and of optimizing the techniques for the reduction and analysis of extended sources with present and forthcoming VHE installations. To this end, I simulated some interesting sources that will be observed with CTA and the ASTRI Mini-array.

In Chapter 3 I simulated and analyzed the data of the PWN in SNR G0.9+0.1, testing the possibility to observe this source as extended and to disentangle among different spectral shapes. I have also carried out a study on how systematic uncertainties will affect the measured parameters of the source. Following similar work in the literature, in Chapter 4 I describe the implementation of a one-zone time-dependent model for the time evolution of the leptonic population inside PWNe. I applied it to the CTA simulated data to understand how these observations will improve our understanding of SNR G0.9+0.1. In Chapter 5 I applied the same one-zone time-dependent model to another peculiar source, MSH 15-52, and investigated the complex morphology of the source using the CTA simulated data. Finally, in Chapter 6, I describe a more technical work made for testing and analyzing the simulated data of the ASTRI Mini-array. This work was made to test the analysis chain of the ASTRI data and to asses the capabilities of the instrument. My concluding remarks are reported in Chapter 7.

Chapter 2

Pulsar Wind Nebulae

2.1 Introduction

The energetic emission coming from the inner part of many SNRs is believed to be produced by a wind of relativistic charged particles originating from the pulsar magnetosphere and moving inside a magnetic field. These emission regions are called Pulsar Wind Nebulae (Weiler & Panagia 1978) and the prototype of this class of objects is the Crab Nebula (Bühler & Blandford 2014). PWNe can be identified by a centrally filled emission morphology, a flat radio spectrum, a well-organized internal magnetic field, and a very broad-band non-thermal continuum spectrum (de Jager & Djannati-Ataï 2009).

PWNe are steadily fed during their evolution, at variance with the surrounding SNRs where the energy reservoir is the $\sim 10^{51}$ erg of kinetic energy released during the SN explosion (Gaensler & Slane 2006). The main engine of PWNe is the pulsar's rotational energy that is transported in part by relativistic electrons and positrons (the wind) leaving the magnetosphere along open magnetic field lines (Goldreich & Julian 1969). The nebula is produced when the wind interacts with the innermost part of the ejecta of the SNR at the so-called termination shock. The wind slows down and the bulk of its energy is thermalized (Amato 2014). The magnetized hot plasma can radiate, via non-thermal processes, from the radio band up to VHE γ-rays (Gelfand 2017). The radius of the termination shock (R_{TS}) is determined by the balance between the ram pressure of the unshocked wind (eventually originating from the conversion of the pulsar spin-down luminosity in particle kinetic luminosity; Mochol 2017) and the internal pressure of the nebula (Slane

2005):

$$R_{TS} = \sqrt{\frac{L}{4\pi c \omega p_{pwn}}} \tag{2.1}$$

where L is the pulsar spin-down luminosity, ω is the equivalent filling factor for an isotropic wind and p_{pwn} is the pressure inside the PWN.

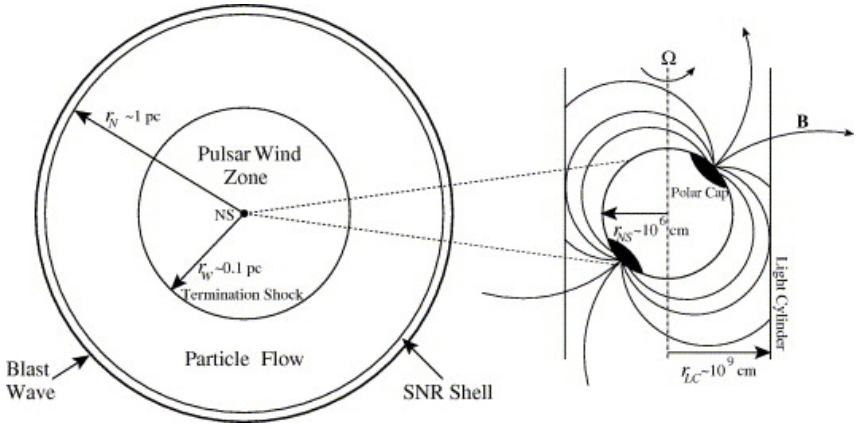

Figure 2.1: Schematic view of the pulsar magnetosphere and the associated PWN. The region indicated as "Particle Flow" is where the nebula radiates via non-thermal processes (Slane 2005).

2.2 The pulsar wind

The wind of relativistic particles is generated inside the pulsar's magnetosphere. The pulsar accelerates the particles and powers a low frequency electromagnetic wave steadily losing part of its rotational energy ($L \equiv \dot{E} = -dE_{rot}/dt$):

$$L = 4\pi^2 I \frac{\dot{P}}{P^3} \tag{2.2}$$

where I is the moment of inertia of the NS, P the rotational period and $\dot{P}$ the period derivative. It is largely believed that only pulsars with a spin-down luminosity $L \gtrsim 4 \times 10^{36}$erg s^{-1} can produce PWNe bright enough to be detected (Gotthelf 2004).

The magnetosphere[1] of the pulsar is filled by charged particles that can be accelerated

[1]The magnetosphere is the region around the pulsar where the magnetic field lines rigidly co-rotate with the pulsar.

in limited charge-separated regions called vacuum gaps (Mochol 2017; Slane 2017; Pétri 2016; Venter 2016). The location of these regions is dependent on the models: they could be in the polar caps (near the stellar surface and close to the magnetic axis of the pulsar; Sturrock 1971; Ruderman & Sutherland 1975; Harding et al. 1978; Daugherty & Harding 1982), in the outer magnetosphere (Cheng et al. 1986; Romani & Yadigaroglu 1995), in a region along the last open field line (Arons & Scharlemann 1979; Muslimov & Harding 2004; Dyks & Rudak 2003), or in current sheets just outside the light-cylinder (Lyubarskii 1996)[2]. In the case of an aligned rotator (spin axis parallel to the magnetic axis) the maximum electric potential generated by the rotating magnetic field of the NS is (Goldreich & Julian 1969):

$$\Phi = \frac{2\pi^2 B_p R_{NS}^3}{cP^2} \tag{2.3}$$

where B_p is the magnetic dipole strength at the pole and R_{NS} is the radius of the NS. The strong electric field rips the charges off from the stellar surface and accelerates them along the magnetic field lines (Mochol 2017). The particle current $\dot{N}_{GJ}$ induced by the potential Φ is:

$$\dot{N}_{GJ} = \frac{c\Phi}{e} \approx 4 \times 10^{33} \left(\frac{L}{10^{38} \text{ erg s}^{-1}} \right)^{1/2} \text{ s}^{-1} \tag{2.4}$$

The accelerated particles produce curvature radiation that initiates an electron-positron pair cascade. From the observations, the value of the particle current needed to explain the radio synchrotron emission of PWNe is on the order of $\dot{N} \sim 10^{40}$ s^{-1}. This in turn requires a multiplicity (the number of pairs created per primary particle inside the magnetosphere) of about $k \sim 10^5 - 10^7$ (Slane 2017). This number is difficult to explain when compared to simulations of electromagnetic cascades ($k \sim 10^3 - 10^5$; Tchekhovskoy et al. 2013), and probably needs the contribution of some other mechanism besides pair production (Timokhin & Harding 2015; Atoyan & Aharonian 1996).

Assuming an inertia-free plasma (transport of energy and momentum purely electromagnetic) it is possible to describe the magnetosphere using a magnetohydrodynamic (MHD) model, the so-called Force-Free Electrodynamics (FFE) approximation (see e.g. Michel 1973; Scharlemann & Wagoner 1973; Komissarov 2002; Blandford 2002). Beyond the magnetosphere, the plasma cannot corotate with the pulsar and, as a consequence, the magnetic field lines are bent backwards moving outside. In the case of an oblique

[2]For a review on the different models for the acceleration regions see, for example, Hirotani (2006) and Harding (2013).

rotator (magnetic field axis not aligned with the spin axis of the pulsar) the torque on the magnetic field lines is even higher. This creates a split-monopole configuration for the magnetic field, where in the equatorial plane two monopoles are joined together. A current sheet is then generated between the two regions where the magnetic field has opposite directions. This current sheet oscillates following the rotation of the pulsar (see Figure 2.2) and forms a structure called the striped wind (Coroniti 1990; Michel 1994; Bogovalov 1999; Kirk & Lyubarsky 2001; Pétri 2013). For a detailed review on the striped wind we refer to Mochol (2017).

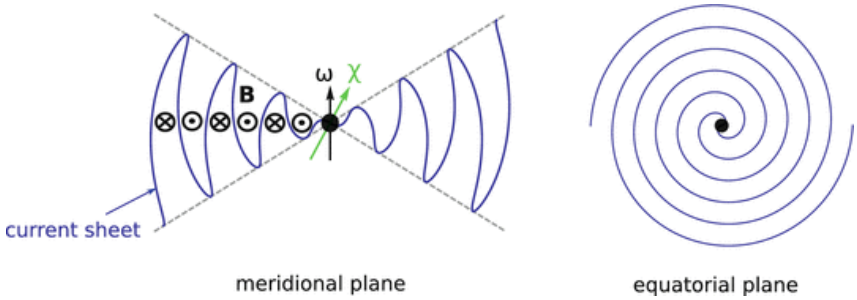

Figure 2.2: Schematic view of the pulsar striped wind for an oblique rotator. The current sheet is corrugated and separates the stripes of opposite magnetic polarity (Mochol 2017).

In PWNe a physically important parameter is the so-called magnetization parameter σ, that is the ratio of the Poynting flux to the particle energy flux:

$$\sigma = \frac{F_{Poynting}}{F_{particle}} = \frac{B^2}{4\pi\rho\gamma c^2} \tag{2.5}$$

where B is the magnetic field, ρ the mass density of particles and γ is the Lorentz factor of the wind. The pulsar wind at the magnetosphere is expected to be dominated by the Pointing flux, with typical values of $\sigma > 10^4$. However, from the observations of various sources, such as the Crab Nebula (Kennel & Coroniti 1984b), the value of σ at the termination shock is inferred to be much smaller ($\sigma \ll 1$). In some way the wind changes from being dominated by the electromagnetic field to being dominated by the kinetic energy of the particles. This is usually referred to as the "σ-problem". The main mechanism that is believed to cause this conversion is the magnetic reconnection (Lyubarsky 2003; Sironi & Spitkovsky 2011).

2.3 Temporal evolution

This section is based on the review made by Gaensler & Slane (2006) and other works (Reynolds & Chevalier 1984; Chevalier 1998; Blondin et al. 2001; Bucciantini et al. 2003; van der Swaluw et al. 2004; Chevalier 2005). Without entering in too many details on how the wind of charged particles is generated, it is possible to model the various phases of the evolution of a PWN simply assuming that the pulsar continuously injects energy and pairs inside it.

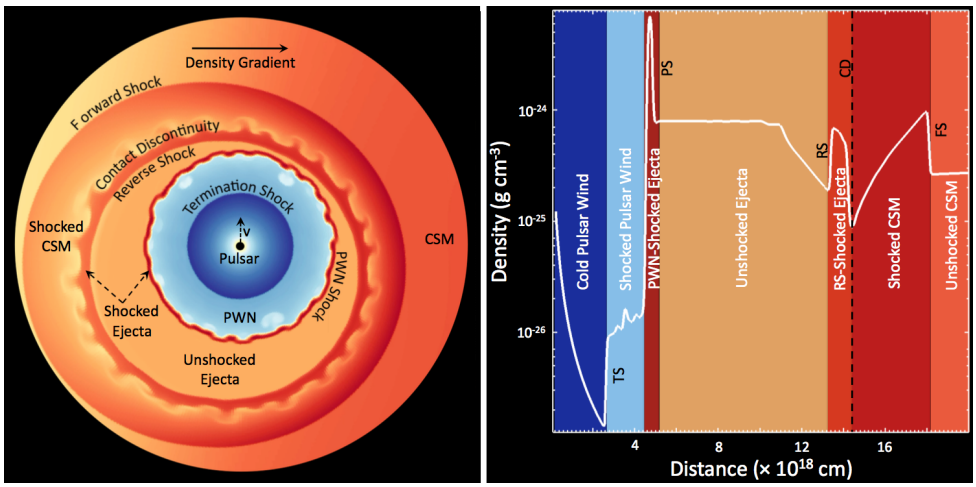

Figure 2.3: Sketch of a young PWN expanding in a SNR from a hydrodynamical simulation before the interaction of the PWN with the reverse shock of the SNR. The right panel shows the density profile (Slane 2017).

The evolution is then tightly dependent on the energy input from the pulsar and on the interaction of the PWN with the surrounding medium. In the early phases, the surrounding medium is the SNR ejecta, while at a much later time this can be the Inter-Stellar Medium (ISM). At the beginning, when the SNR is in the freely expanding phase, the PWN expands rapidly since the pressure inside the nebula is much higher then that of the surroundings[3]. The radius evolves as $R_{PWN} \propto t^{6/5}$ (Chevalier 1977). The position of the pulsar is close to the center, even in the case of a high kick velocity for the neutron star, since the sound speed of the fluid inside the PWN is $c_s = c/\sqrt{3}$ and the PWN responds to any pressure variations possibly induced by the pulsar displacement.

[3]More details are given in Chapter 4, where we present a 1-zone time-dependent evolutionary model for the electrons inside a young PWN.

When the swept-up material from the ISM becomes comparable to the mass ejected in the SN explosion, the SNR enters into the "Sedov-Taylor" stage (Sedov 1959; Taylor 1950). A forward shock heats and compresses the cold ISM and moves outward, while an inside reverse shock starts to decelerate the ejecta material. This reverse shock will start moving inward and eventually reaches the center of the SNR (Reynolds & Chevalier 1984). At a certain time, the SNR reverse shock and the outer shell of the expanding PWN start to interact (Blondin et al. 2001; van der Swaluw et al. 2001). This interaction compresses the nebula, that responds to it increasing the internal pressure and causing a new subsequent fast expansion. The system reverberates several times (Gelfand et al. 2009; Torres et al. 2019). In this phase, Rayleigh-Taylor instabilities produce a chaotic filamentary structure (Chevalier 1998; Blondin et al. 2001) and the interactions between the PWN, the SNR and the ISM results in a highly complex morphology, with the pulsar position significantly displaced from the center (Chevalier 1998; van der Swaluw et al. 2004).

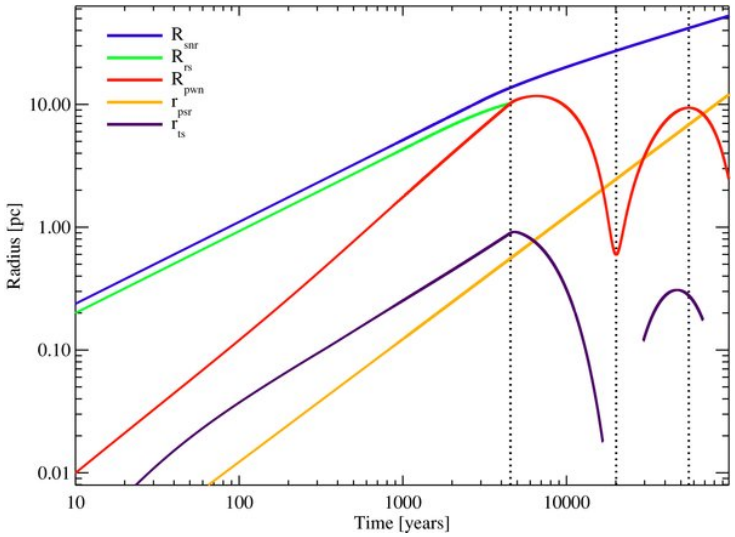

Figure 2.4: Radius evolution of the forward shock (blue) of the SNR, the reverse shock (green) of the SNR, the PWN (red), the termination shock (purple), and the pulsar position (yellow). The vertical dashed lines separate four different phases of the PWN evolution: initial expansion, reverse shock collision and first compression, re-expansion, and second compression (Gelfand et al. 2009).

After the reverberation phase, the distance traveled by the pulsar can be significant and thus it can escape from the original nebula. The pulsar generates a new and smaller PWN, and the old one is often referred to as a "relic PWN" (van der Swaluw et al. 2004). In this phase, the magnetic field in the nebula drops to small values ($\sim 5\ \mu$G; see e.g. de

Jager et al. 2008) and so ratio of the IC to the synchrotron luminosity increases (Slane 2017). This means that in the late phases of the evolution of PWNe the γ-ray emission can dominate over the radio and the X-ray bands. This may explain why PWNe dominate the population of TeV sources in the Galactic Plane (Carrigan et al. 2013).

The final step in the evolution of PWNe occurs when the pulsar exits its host SNR. In the cold ISM the sound speed is much lower then the pulsar speed, that becomes supersonic and drives a bow-shock through the medium (Wilkin 1996; Van Der Swaluw et al. 1998; Bucciantini & Bandiera 2001). The balance of the ram pressure of the wind with the ISM creates a "cometary-like shape" in these bow-shock PWNe (Olmi & Bucciantini 2019).

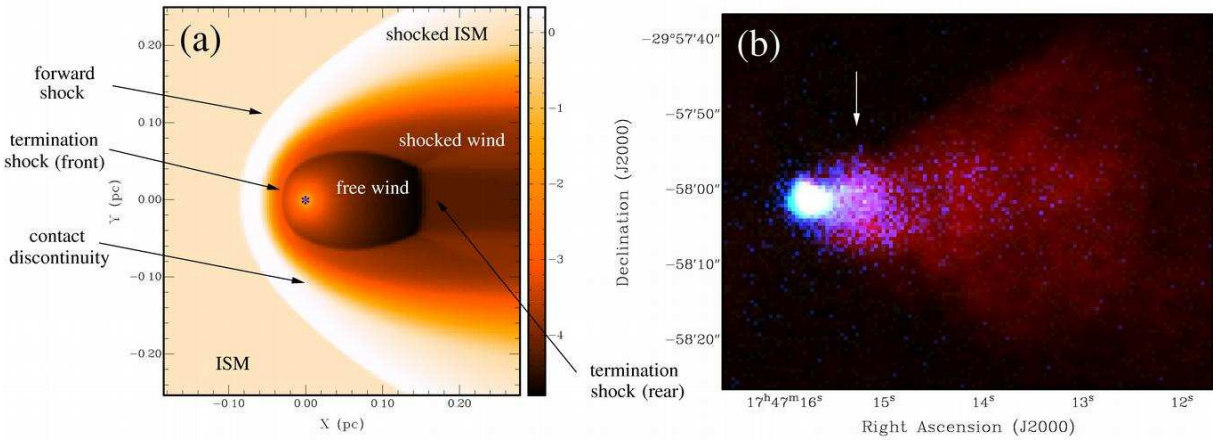

Figure 2.5: Left: hydrodynamic simulation of a bow-shock PWN. Right: X-ray (*Chandra*; in blue) and radio (VLA; in red) images of the bow-shock formed from the PWN G359.23-0.82 (Gaensler et al. 2004).

2.4 Observational properties

The wind generated from the pulsar is highly axisymmetric (Lyubarsky 2002) because of the structure of the magnetic field in a striped wind, as discussed above. Observations show "torus-like" regions of enhanced luminosity along the equatorial plane, together with collimated jets along the rotation axis of the pulsar (Begelman & Li 1992; van der Swaluw 2003). The inner torus may correspond to the termination shock (Bucciantini et al. 2006).

High-resolution X-ray and optical images show also wisps and filamentary structures that are variable on timescales of days (Figure 2.6; Slane 2008). These structures can be produced by synchrotron instabilities, by Rayleigh-Taylor instabilities, or by the compression of the plasma in particular regions of the nebula (Hester et al. 1996, 2002; Gallant & Arons 1994; Spitkovsky & Arons 2004).

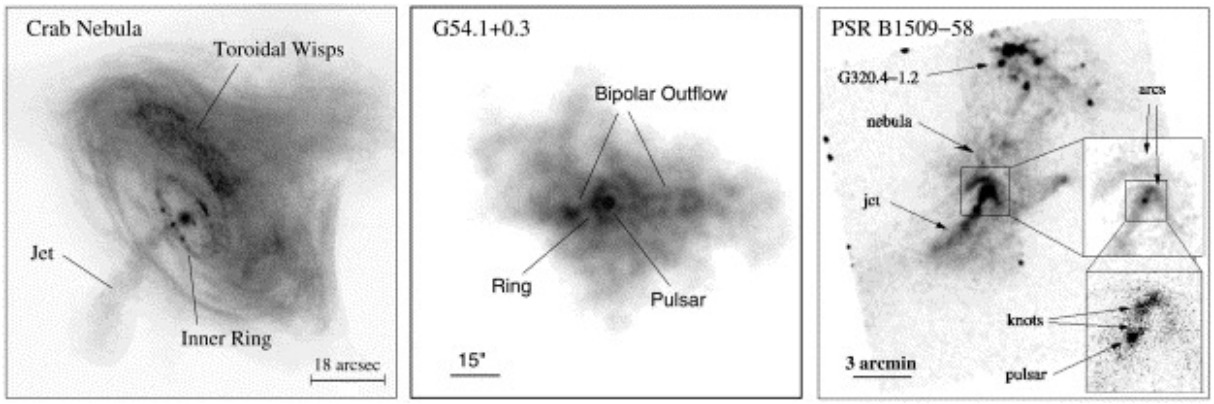

Figure 2.6: X-ray images (*Chandra*) of three PWNe showing jets, torus-like structures and wisps (Slane 2008).

One of the most studied sources at high energies (and at VHE) is the Crab Nebula (for a review on the emission properties of the pulsar and the nebula see Zanin 2017). For a long time, it was considered a standard candle and used for calibration (Meyer et al. 2010). However, flares and variability on short timescales have been discovered (see e.g. Bednarek & Idec 2011; Tavani et al. 2011; Buehler et al. 2012; Lyutikov et al. 2012). Nonetheless, the Crab Nebula remains one of the best-studied PWNe and most of the models of these sources were developed from observations of this nebula.

The typical multiwavelength (MWL) spectral energy distribution (SED) of a PWN shows two different peaks, one produced by synchrotron emission, and one by IC emission. An intrinsic break in the synchrotron spectra is often found close to the optical band, where the slope changes. This is caused by the underlying SED of the leptonic population accelerated at the termination shock, that typically has a broken power law shape (see the discussion in Gelfand 2017).

In the higher energy part of the MWL SED, the IC mechanism dominates. The very high energy electrons in the nebula scatter against the low energy photons of the Inter-Stellar Radiation Field (ISRF) increasing their energies up to the VHE γ-rays. The main background radiation fields are the Cosmic Microwave Background (CMB), the Far

Infra-Red (FIR) emission from the interstellar medium, and the Near Infra-Red (NIR) emission from stars in the field. In some cases also the Synchrotron-Self-Compton (SSC, the synchrotron radiation is scattered at higher energies by the same emitting electrons) can be a dominant mechanism at VHE, as in the case of the Crab Nebula (Torres et al. 2013b).

Studying the MWL SED enables us to extract important physical information, such as the strength of the average magnetic field and the particle number density in the nebula (de Jager et al. 1996). The magnetic field of the nebula can be estimated following Aharonian et al. (1997). Assuming a δ-functional approximation for the energy dependence of the synchrotron and IC cross-section (see Ginzburg 1979) and assuming that IC scattering takes place in the Thomson regime, it is possible to relate the energy of synchrotron (E_{syn}) and IC photons (E_{IC}) with the energy of the electrons (E_e) that emit the radiation:

$$E_{syn} = \frac{heBE_e^2}{4\pi m_e^3 c^5} \tag{2.6}$$

$$E_{IC} = \frac{4\bar{E}_{CMB,ph}E_e^2}{3m_e^2 c^4} \tag{2.7}$$

where h is the Planck constant, e and m_e the charge and the mass of the electron, c the velocity of light, B the magnetic field and $\bar{E}_{CMB,ph}$ the mean energy of the target photons (assuming only CMB photons) for IC scattering. The two equations can be combined together to obtain the relation:

$$E_{syn} = 70 \left(\frac{E_{IC}}{1\ \text{TeV}}\right) \left(\frac{B}{10^{-5}\ \text{G}}\right)\ \text{eV} \tag{2.8}$$

Therefore, for a mean magnetic field around $10 - 100\ \mu$G, there is a direct correlation between the fluxes in the soft X-rays and VHE γ-rays (Aharonian et al. 1997; de Jager et al. 1996).

Figure 2.7 shows the modelled SED of a PWN. In the first panel, it is possible to see how this SED is expected to evolve with time. In the second panel, it is shown the contribution to the present SED of leptons injected in the nebula at different times (Mayer et al. 2012; H. E. S. S. Collaboration et al. 2018b). The two peaks of the SED are clearly visible in the plots, as well as the evolution of the relative contributions. The synchrotron spectrum decreases much faster with time than the IC spectrum, due to the rapidly decaying magnetic field in the nebula.

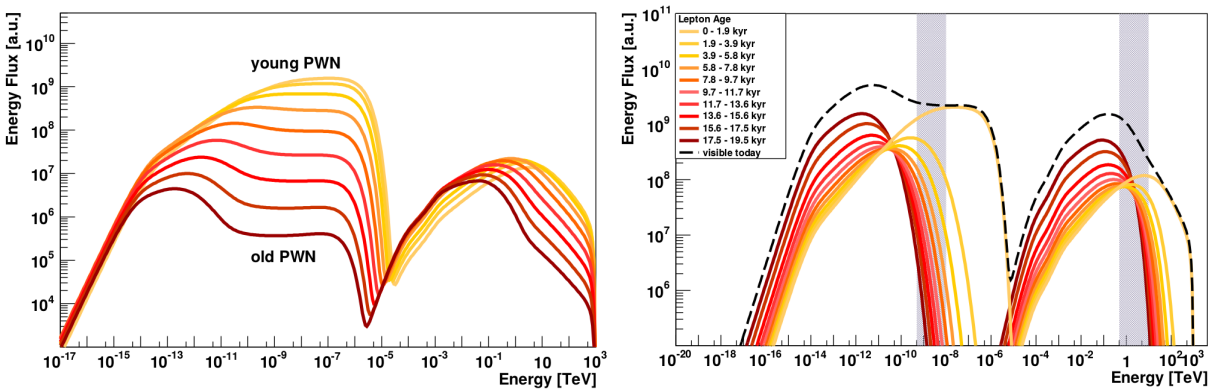

Figure 2.7: Modelled MWL SED of a PWN. Left: time evolution of the spectrum. Right: contribution to the total SED (at a fixed time) of leptons injected in the nebula at different times (Mayer et al. 2012).

Finally, it is worth mentioning that a scenario where a population of hadrons coexists with a population of leptons in the PWN could be possible (for example for the PWN in G54.1+0.3; Li et al. 2010). Hadrons could give a non-negligible contribution to the TeV flux of PWNe. For a discussion on the hadronic emission mechanism see Cheng et al. (1990), Bednarek & Protheroe (1997), and Amato et al. (2003). In many cases the hadrons in the nebula could be a small fraction of the total number of the emitting particles and only some of the observed VHE photons could originate from them. Disentangling this possible hadronic emission component from the IC contribution is difficult. A way to test this possibility is by trying to detect the neutrinos fluxes expected for the production of the γ-rays via nuclear interactions (Di Palma et al. 2017; Liu & Kheirandish 2019).

Chapter 3

Simulation and analysis of a young PWN with CTA - The case of SNR G0.9+0.1

3.1 Introduction

The purpose of this work is to test the capabilities of CTA to observe specific sources and assess its impact on our understanding of the physical processes inside these nebulae. The source selected is SNR G0.9+0.1, a well known composite supernova remnant (Helfand & Becker 1987). We selected this source because is at the limit of the sensitivity of the current γ-ray facilities to demonstrate the improvements in the quality of the data that CTA will generate. Moreover, the PWN is in the direction of the Galactic Center, an area that will be observed extensively with CTA. The bright central core has been unambiguously identified as a PWN through X-ray observations (Gaensler et al. 2001). SNR G0.9+0.1 is composed by a PWN in the core (with a diameter of $\sim 2'$) surrounded by a SNR (with a diameter of $\sim 8'$, Dubner et al. 2008). This source has been observed at Very High Energy (VHE) by HESS (Aharonian et al. 2005b), VERITAS (Smith & the VERITAS Collaboration 2015) and MAGIC (Ahnen et al. 2017). It has been detected up to $\sim$ 20 TeV. For all these facilities the source appears point-like because of the limited angular resolution.

The source position, its faintness (only about 2% of the Crab flux) and the small

angular size make this object a really interesting target for testing the capabilities of the CTA. Since the source extension is comparable to the best angular resolution achievable with CTA, it will be possible to measure its size at VHEs. In addition, the sensitivity of CTA will be much better up to and above 100 TeV (CTA Consortium 2019).

3.2 Simulations

To simulate, reduce and analyze the γ-ray data we made use of the software *ctools*, a software package developed for the scientific analysis of CTA data (Knödlseder et al. 2016).

We specified in input: a spatial and a spectral model describing the emission region of SNR G0.9+0.1 and a model for the spatial distribution of the cosmic-ray background. For the spectral models we adopted both a power law and a power law with an exponential cut-off (PLEC):

$$\frac{dN}{dE} = N_0 \left(\frac{E}{E_0} \right)^{-\Gamma}, \tag{3.1}$$

$$\frac{dN}{dE} = N_0 \left(\frac{E}{E_0} \right)^{-\Gamma} \exp\left(\frac{E}{E_{cut}} \right), \tag{3.2}$$

where N_0 is a normalization factor, Γ the spectral index and E_{cut} the cut-off energy. For the spatial model, we use different distributions as described in the following.

SNR G0.9+0.1 is projected in the direction of the crowded region of the Galactic Center. To understand which sources can significantly affect the measurement of the flux of SNR G0.9+0.1 and to test the capability of *ctools* to simulate the extended emission of the Galactic Center we simulate the γ-ray emission in a field of $3^\circ \times 1^\circ$ around the position of Sgr A*.

3.2.1 Galactic center extended region

In a box of 3 square degrees around the center of the Galaxy there are many sources at TeV energies as observed by the HESS, MAGIC and VERITAS collaborations (Aharonian et al. 2006a; Archer et al. 2016; H. E. S. S. Collaboration et al. 2017; Ahnen et al. 2017).

We consistently selected all the sources from the HESS catalogue[1], except for SNR G0.9+0.1 for which we take data also from VERITAS [2]. The sources considered in our simulation are listed below and their spatial and spectral parameters are reported in Table 3.1.

- HESS J1745-290 (Aharonian et al. 2004): This source represents the TeV emission coming from the center of our Galaxy (Acero et al. 2010). It is associated with the supermassive black hole Sgr A* or to the candidate PWN G359.95-0.04 (Kistler 2015). It is modeled as a point source with a power law spectrum with an exponential cut-off. The spectral parameters are taken from Aharonian et al. (2009)

- HESS J1741-302 (Tibolla et al. 2008): It is an unidentified source detected with HESS at $\sim 1\%$ of the Crab flux above 1 TeV. We modeled it as a point source with a power law spectrum.

- HESS J1745-303 (Aharonian et al. 2006b): This is an extended and unidentified VHE γ-ray source at l=-0.4°. The morphology of the source is quite complex owing to the presence of 3 major emitting regions. The spatial extension of this source has been modeled using the HESS excess map[3], shown in Figure 3.1. The spectral model is a power law (Aharonian et al. 2008).

- Diffuse emission along the Galactic plane (Aharonian et al. 2006a): It is a region of diffuse emission (of approximately $\pm 1^{\circ}$ in galactic longitude) probably associated with the interaction of cosmic-ray particles with molecular clouds. This diffuse emission is the only source that can affect our simulation of SNR G0.9+0.1 because the spatial emission regions of these sources overlap. For the spatial model we used a section (between $359.1^{\circ} < l < 1.5^{\circ}$ and $|b| < 0.4^{\circ}$) of an image taken from HESS[4] (Figure 3.2) in which the emission coming from HESS J1745-290 and SNR G0.9+0.1 has been previously subtracted. The spectral model is a power law.

[1] www.mpi-hd.mpg.de/hfm/HESS/pages/home/sources/

[2] veritas.sao.arizona.edu/

[3] www.mpi-hd.mpg.de/hfm/HESS/pages/publications/auxiliary/hessj1745-303-aux.html

[4] www.mpi-hd.mpg.de/hfm/HESS/pages/publications/auxiliary/gcdiffuse_auxinfo.html

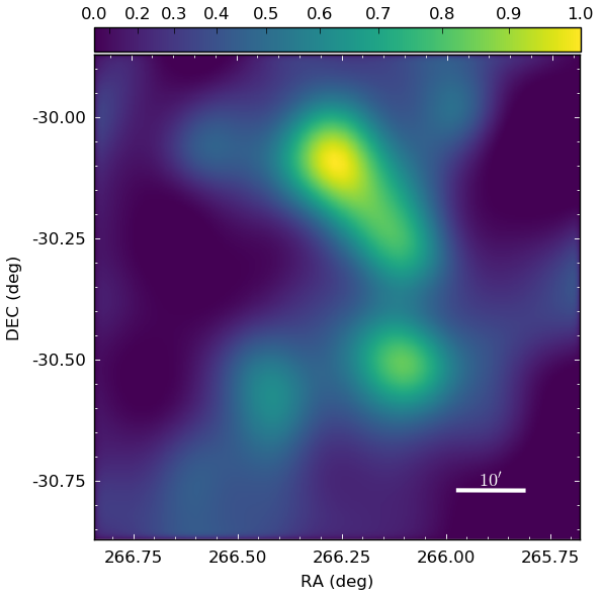

Figure 3.1: Excess map of HESS J1745-303 (Aharonian et al. 2008), used as spatial model for our simulations.

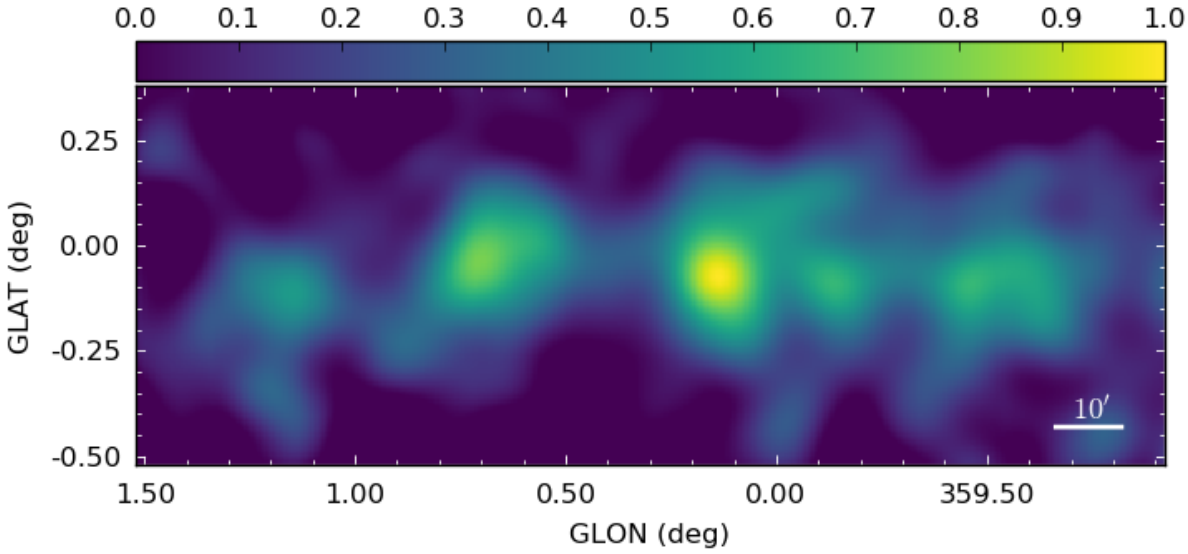

Figure 3.2: HESS excess map of the diffuse emission around the Galactic center (the emission from SNR G0.9+0.1 and HESS J1745-209 has been previously subtracted) (Aharonian et al. 2006a), used as input spatial model for our simulations.

- SNR G0.9+0.1 (Aharonian et al. 2005b): The spatial model is taken from a radio map at 843 MHz from the Sydney University Molonglo Sky Survey [5] (radiomap template hereafter). The map has been prepared for the simulation with a technique developed for the analysis of extended sources in *Fermi*-LAT[6]. For the spectral model we used a power law, as defined from the HESS and VERITAS data (Smith & the VERITAS Collaboration 2015).

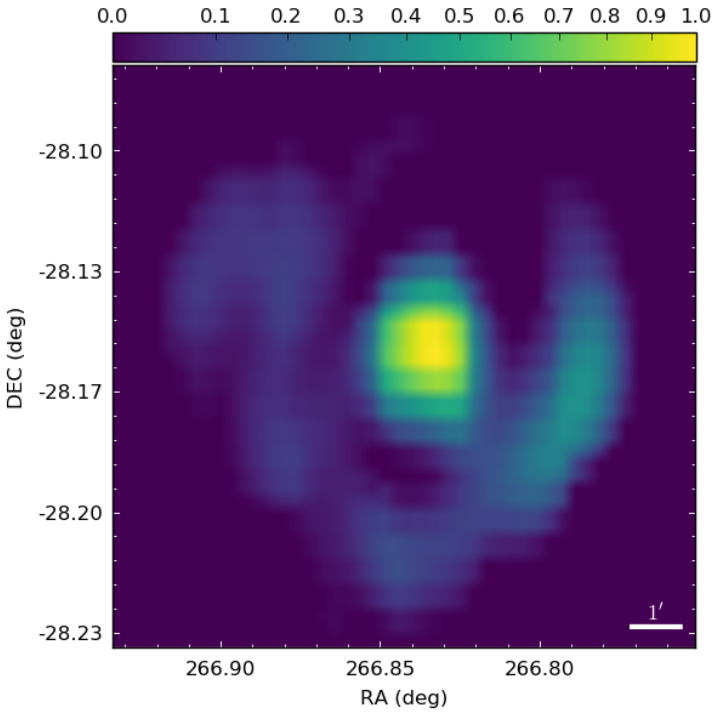

Figure 3.3: Radio image (843 MHz) of SNR G0.9+0.1 taken from the Sydney University Molonglo Sky Survey (SUMSS) and used as template for some of our simulations. Most of the power in the radio band is coming from the PWN that is surrounded by the less energetic shell of the supernova remnant.

To simulate observations of the field with the southern CTA facility (CTA-South) we made use of the Instrument Response Functions (IRFs) made available by the CTA Consortium (MC-prod3b-v2, Hassan et al. 2015). We provided as input all the information on the sources listed above, plus a model for the spatial distribution of the cosmic-ray

[5] skyview.gsfc.nasa.gov/surveys/sumss/mosaics/Galactic/J1752M28.FITS

[6] fermi.gsfc.nasa.gov/ssc/data/analysis/scitools/extended/extended.html

Table 3.1: Input data used with *ctobssim* to simulate the VHE emission from a region of $\approx 3^\circ \times 1^\circ$ around the Galactic center. The reported positions are taken from the SIMBAD astronomical database (Wenger et al. 2000), except for the position of the Galactic diffuse emission for which we adopt the position of the center of the template map. E_0 is always equal to 1 TeV.

Source	Spatial Model	Position	Spectral Model	Input Parameters
HESS J1745-290	point source	RA=266.°4150 Dec=−29.°0061	PLEC[d]	$N_0 = 2.55 \times 10^{-12}$ TeV^{-1}cm^{-2}s^{-1} $\Gamma = 2.10$ $E_{cut} = 15.7$ TeV
HESS J1741-302	point source	RA=265.°2500 Dec=−30.°2000	power law[e]	$N_0 = 2.34 \times 10^{-13}$ TeV^{-1}cm^{-2}s^{-1} $\Gamma = 2.30$
HESS J1745-303	Extended Source HESS excess map[a]	RA=266.°2970 Dec=−30.°1990	power law[f]	$N_0 = 2.84 \times 10^{-12}$ TeV^{-1}cm^{-2}s^{-1} $\Gamma = 2.71$
Galactic Diffuse	Extended Source HESS excess map[b]	RA=266.°6518 Dec=−28.°7166	power law[g]	$N_0 = 1.73 \times 10^{-8}$ TeV^{-1}cm^{-2}s^{-1}sr^{-1} $\Gamma = 2.29$
SNR G0.9+0.1	Extended Source SUMSS radio map (843 MHz)[c]	RA=266.°8250 Dec=−28.°1500	power law[h]	$N_0 = 8.80 \times 10^{-13}$ TeV^{-1}cm^{-2}s^{-1} $\Gamma = 2.29$

[a]Figure 3.1, [b]Figure 3.2, [c]Figure 3.3

[d]Aharonian et al. (2009), [e]Tibolla et al. (2008), [f]Aharonian et al. (2008), [g]Aharonian et al. (2006a), [h]Smith & the VERITAS Collaboration (2015)

background ("CTAIrfBackground"). We simulated four observations with different observing times centered on the position of Sgr A*, in the energy range 0.2-180 TeV: one 30 minute observation, one 5 hour observation, one 50 hours observation, and one 200 hours observation We then made an unbinned analysis[7] and fitted all the simulated data with the same models given in input. Applying the maximum likelihood method, we finally compute the Test Statistics (TS) value for each source[8].

3.2.2 SNR G0.9+0.1

As far as SNR G0.9+0.1 is concerned, we divided the analysis in two parts: first, we fixed all the spectral parameters of the source and varied only the spatial model, then we kept fixed the spatial model (one of the previously selected models) and varied the spectral parameters. At this stage, we include in the simulations only the information on SNR G0.9+0.1, the diffuse emission from the Galactic plane and the cosmic-ray background. The simulated field has a radius of 0.25° centered on the source.

To understand the capabilities of CTA in resolving the spatial extension of the VHE emission of SNR G0.9+0.1, we perform the simulations using different spatial models in the energy range 0.2-180 TeV. All the simulated observations last 200 hours and have fixed spectral parameters (a power law with the parameters reported in Table 3.1). We choose 200 hours because we want to test the results achievable with CTA under the best assumptions regarding the observing time. In fact, this number is justified by the fact that the Galactic Center will be extensively observed during the first years of CTA operations (CTA Consortium 2019). The spatial models used here are: point source (assuming that the VHE emission comes only from the inner part of the remnant), a radio map template (assuming that the VHE emission comes from the same region as the radio emission) and various spatially uniform radial disk models with different radii, from 0.01° to 0.16°. We then fit all the simulated data with four different spatial models: a point source model, a radial Gaussian model, a radial disk model, and the radiomap template model. Model fitting has been performed with a binned maximum likelihood analysis.[9] As before, we

[7] http://cta.irap.omp.eu/ctools/users/tutorials/quickstart/unbinned.html

[8] The square root of the TS value is roughly the Gaussian σ and describe the goodness of the fit.

[9] http://cta.irap.omp.eu/ctools/users/tutorials/quickstart/fitting.html

determine the goodness of fit measuring the TS value.

After the analysis of the spatial properties of the source, we perform the analysis of the spectral properties fixing all the spatial parameters. Our goal is to asses the detectability of the source in the higher energy range (from 30 TeV up to 180 TeV) and the capability of CTA-South to distinguish between different spectral models. We simulate different observations, all lasting 200 hours, with the source spatially modeled with the radiomap template and spectrally modeled with a power law and various PLEC with different cut-off energies (20 TeV, 30 TeV, 50 TeV, and 100 TeV). Data are simulated in the energy range between 0.2 TeV and 180 TeV. Model fitting has been performed with the binned likelihood analysis. The spectral energy distribution (SED) of the source is extracted using *csspec*, a specific tool of *ctools*.

3.3 Simulations results

3.3.1 Galactic center extended region

In Table 3.2 we show the results of the unbinned analysis performed on the four different simulations of the Galactic center region mentioned in section 3.2.1. We report all the TS values and the spectral parameters measured for all the sources in the simulations.

We then compared the simulation obtained for an exposure of 50 hours with that obtained with HESS in 55 hours[10] (Aharonian et al. 2006a). The simulated CTA spectra were extracted from two energy ranges, one similar to that of the HESS observation (0.2-10 TeV) and the other in an higher energy range (10-180 TeV, see Figure 3.4).

The images are in good agreement, with the CTA simulated one having a lower background contamination. With the same observing time, CTA will allow us to obtain a wider spectral coverage range with a higher signal-to-noise.

[10] www.mpi-hd.mpg.de/hfm/HESS/pages/publications/auxiliary/gcdiffuse_auxinfo.html

Table 3.2: Results of the unbinned maximum likelihood analysis on the simulated observations of the Galactic center region. After 30 minutes of observation all the sources are clearly detected.

Source	0.5 hour observation		5 hour observation	
	Spectral parameters[a,b]	TS	Spectral parameters[a,b]	TS
HESS J1745-290	$N_0 = (3.29 \pm 0.47) \times 10^{-12}$ $\Gamma = 1.95 \pm 0.12$ $E_{cut} = 5.73 \pm 2.06$	371	$N_0 = (2.51 \pm 0.11) \times 10^{-12}$ $\Gamma = 2.07 \pm 0.04$ $E_{cut} = 14.54 \pm 3.53$	3444
HESS J1741-302	$N_0 = (2.36 \pm 0.74) \times 10^{-13}$ $\Gamma = 2.32 \pm 0.29$	27	$N_0 = (2.55 \pm 0.26) \times 10^{-13}$ $\Gamma = 2.21 \pm 0.07$	301
HESS J1745-303	$N_0 = (2.49 \pm 0.28) \times 10^{-12}$ $\Gamma = 2.83 \pm 0.08$	318	$N_0 = (2.73 \pm 0.09) \times 10^{-12}$ $\Gamma = 2.71 \pm 0.02$	3081
Galactic Diffuse	$N_0 = (1.86 \pm 0.06) \times 10^{-8}\mathrm{sr}^{-1}$ $\Gamma = 2.31 \pm 0.03$	869	$N_0 = (1.71 \pm 0.01) \times 10^{-8}\mathrm{sr}^{-1}$ $\Gamma = 2.30 \pm 0.01$	7787
SNR G0.9+0.1	$N_0 = (7.66 \pm 1.32) \times 10^{-13}$ $\Gamma = 2.13 \pm 0.11$	103	$N_0 = (8.12 \pm 0.41) \times 10^{-13}$ $\Gamma = 2.31 \pm 0.04$	995
	50 hour observation		200 hour observation	
	Spectral parameters[a,b]	TS	Spectral parameters[a,b]	TS
HESS J1745-290	$N_0 = (2.61 \pm 0.03) \times 10^{-12}$ $\Gamma = 2.07 \pm 0.01$ $E_{cut} = 13.75 \pm 0.86$	36493	$N_0 = (2.53 \pm 0.01) \times 10^{-12}$ $\Gamma = 2.10 \pm 0.01$ $E_{cut} = 15.83 \pm 0.53$	142506
HESS J1741-302	$N_0 = (2.36 \pm 0.08) \times 10^{-13}$ $\Gamma = 2.27 \pm 0.03$	2526	$N_0 = (2.38 \pm 0.04) \times 10^{-13}$ $\Gamma = 2.30 \pm 0.01$	9987
HESS J1745-303	$N_0 = (2.79 \pm 0.03) \times 10^{-12}$ $\Gamma = 2.72 \pm 0.07$	32853	$N_0 = (2.83 \pm 0.01) \times 10^{-12}$ $\Gamma = 2.71 \pm 0.01$	132875
Galactic Diffuse	$N_0 = (1.73 \pm 0.01) \times 10^{-8}\mathrm{sr}^{-1}$ $\Gamma = 2.28 \pm 0.03$	80674	$N_0 = (1.73 \pm 0.01) \times 10^{-8}\mathrm{sr}^{-1}$ $\Gamma = 2.29 \pm 0.01$	322679
SNR G0.9+0.1	$N_0 = (8.87 \pm 0.13) \times 10^{-13}$ $\Gamma = 2.30 \pm 0.01$	11274	$N_0 = (8.83 \pm 0.06) \times 10^{-13}$ $\Gamma = 2.30 \pm 0.01$	44901

[a] N_0 in unit of $\mathrm{TeV}^{-1}\mathrm{cm}^{-2}\mathrm{s}^{-1}$ and E_{cut} in unit of TeV. $E_0 = 1\mathrm{TeV}$

[b] Statistical error only

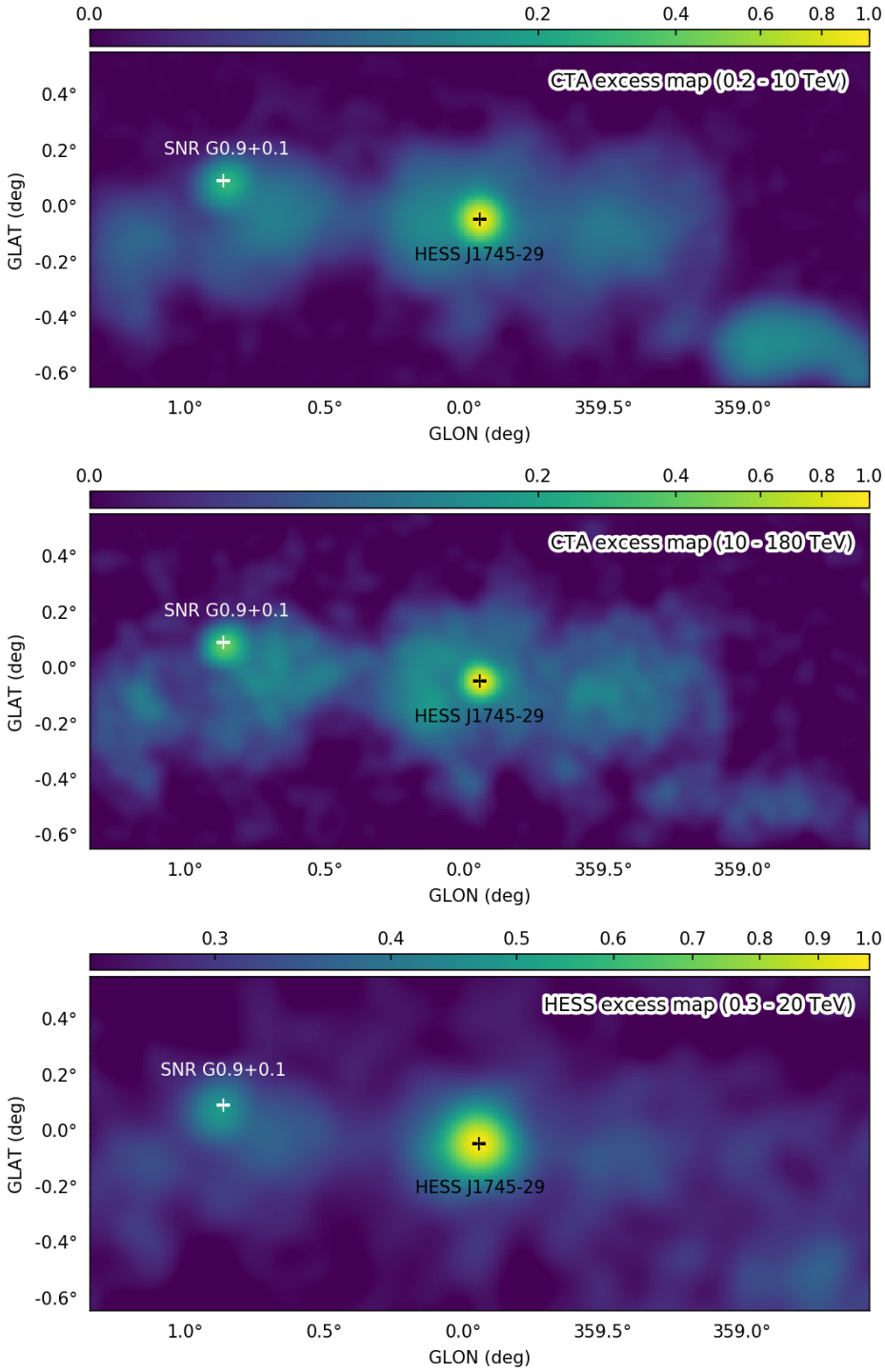

Figure 3.4: Simulation of the Galactic center extended emission as seen with CTA in an observation of 50 hours in two different energy ranges (0.2-10 TeV top panel, 10-180 TeV middle panel) and a residual map of the same region from a HESS observation in the energy range ∼0.3-20 TeV (lower panel; Aharonian et al. 2006a).

3.3.2 SNR G0.9+0.1

We performed two different analyses to investigate the resolving capabilities of CTA. In the first analysis, we carry out different fits of the image simulated using the radiomap template. The fits were performed with four different spatial models: point source model, spatially uniform radial disk model (with the radius left free during the fit), radial Gaussian model (with width left free during the fit) and the radiomap model. The results are shown in Figure 3.5. If the VHE emission follows the radio emission CTA could be able to detect it as an extended object because the TS value for the point source fit is significantly lower.

In the second analysis, we test the limiting resolving capabilities of CTA against the background of the Galactic Center VHE emission region in the following way. We simulated different images assuming a spatially uniform radial disc with different radii. We then fit all the images with a point source model (Figure 3.6). The TS value increases from large to small radii and below $\sim 1.5 - 2.0$ arcmin it becomes nearly constant. This means that if the VHE emission region of SNR G0.9+0.1 is bigger than ~ 1.5 arcmin, CTA would be able to detect it as an extended source. However, it would difficult to study substructures inside the source because the angular size of this substructures would be too small.

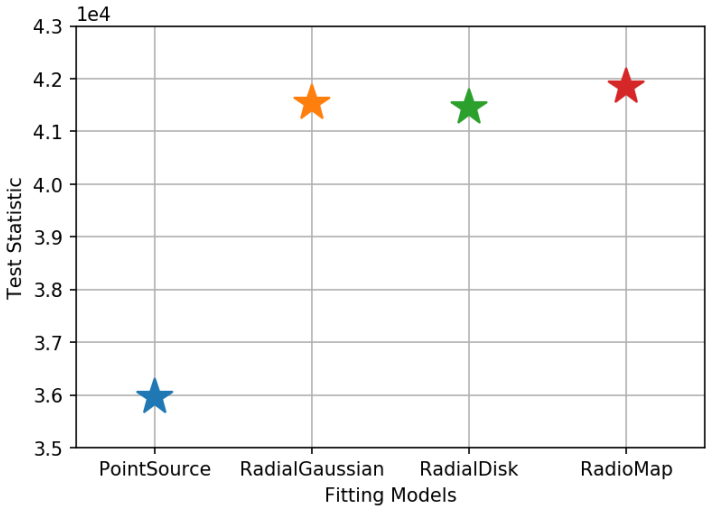

Figure 3.5: Test Statistics values for different fitting models applied to the simulation in which the VHE emitting region of SNR G0.9+0.1 is modeled with the radio map template. The TS for the point source fitting model has a lower significance compared to the other fitting models.

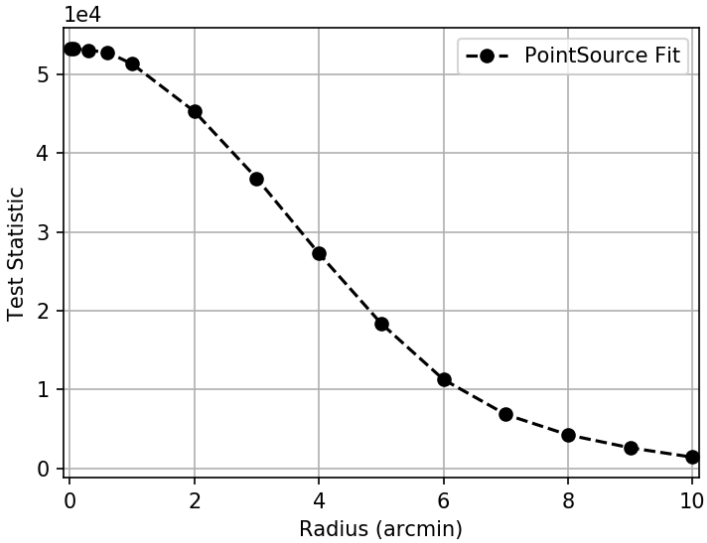

Figure 3.6: Test Statistic values for images simulated using a spatially uniform radial disc with different radii and fitted with a point source model.

As far as the CTA spectrum of SNR G0.9+0.1 is concerned, it is shown in Figure 3.7. The spectrum has a good statistics and therefore the spectral resolution is very good. The fit of each simulated spectrum with a cut-off power-law returned different values for the cut-off energy.

This represents a significant improvement in comparison with currently available data that do not allows to distinguish if the spectral shape of the VHE emission is a power law or a power law with a cut-off at energies higher than 20 TeV (Figure 3.8).

For the spectrum with the lowest cut-off energy the source is detectable only up to ~ 50 TeV, while for a pure power law spectrum the source is detectable up to maximum of the simulated energy range (180 TeV).

3.4 Assessing systematic errors

The spectral analysis of the simulated data returns only the statistical errors. But systematic errors need to be carefully accounted for in order to assess the accuracy of the results.

We considered both the instrumental sources of uncertainties and the background

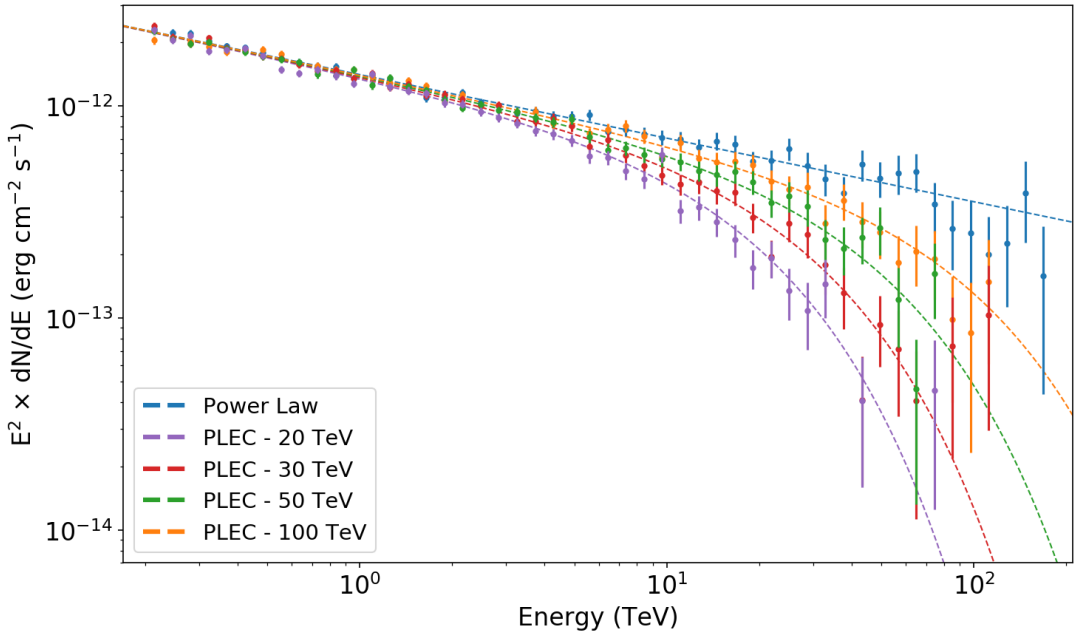

Figure 3.7: CTA spectral energy distribution of SNR G0.9+0.1, simulated using different cut-off energies. The fit of each simulated spectrum with a cut-off power-law returned different values for the cut-off energy.

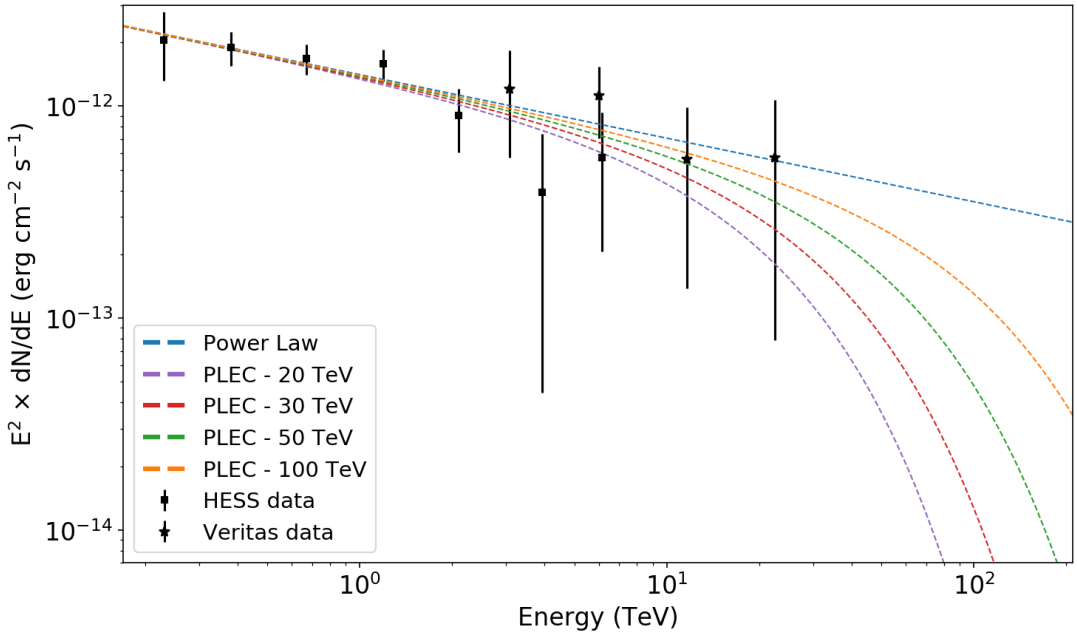

Figure 3.8: Comparison of the spectra simulated in this work with the data from HESS (black square) and VERITAS (black stars). With the current available data it is not possible to rule out models with cut-off energies higher than 20 TeV.

related uncertainties. The instrumental sources of uncertainties are due to the imperfect knowledge of the effective area and to the accuracy of the reconstructed energy scale, while the background sources of uncertainties are due to the cosmic-rays and the Galactic diffuse emission. In order to translate uncertainties into systematic errors on fluxes and spectral indices, we will make some assumptions on how these uncertainties propagate.

In the case of the instrumental uncertainties, we start from CTA technical requirements and we apply the following procedure to measure the associated errors.

- **Knowledge of the effective area**.
  Uncertainty on the effective area of the system must be $< 5\%$ (from the CTA technical requirements). To estimate the effect of such uncertainty we followed the method used by the Fermi-LAT team (Ackermann et al. 2012, Sec. 5.7). We generate perturbed IRFs that represent the worst scenario, extract the spectral parameters and compare them to those obtained with the unperturbed IRF. The perturbed effective area A'_{eff} is written as:

$$A'_{eff}(E,\theta) = A_{eff}(E,\theta) \cdot (1 + \epsilon(E)B(E)), \tag{3.3}$$

  where A_{eff} is the unperturbed effective area, $\epsilon(E) = 0.05$ is the uncertainty and $B(E)$ a function of the energy (bracketing function). Different form for $B(E)$ are adopted depending on the spectral parameter considered. For a simple power law, to maximize the effect on the normalization, the function $B(E)$ is written as:

$$B(E) = \pm 1, \tag{3.4}$$

  while, to maximize the effects on the spectral index, the following expression is used:

$$B(E) = \pm \tanh\left(\frac{1}{0.13}\log\left(\frac{E}{E_0}\right)\right), \tag{3.5}$$

  where E_0 is the pivot energy. With these two modified IRFs, we have reanalyzed the data and estimated the errors on the spectral parameters from the values obtained in the two cases.

- **Accuracy of the Energy Scale.**
  The uncertainty on the energy of a photon event candidate must be $< 6\%$ (from the CTA technical requirements). In order to estimate the errors on the spectral

parameters induced by this uncertainty, we took the simulated data and perturbed all the photon energies as:

$$E' = E \cdot (1 \pm \epsilon(E)), \tag{3.6}$$

where $\epsilon(E) = 0.06$. We have then analyzed these data and estimated the errors on the spectral parameters, repeating the simulation for one hundred times and taking the error from the mean value.

In the case of the uncertainties related to the knowledge of the background, we applied a different approach, as described below.

- **Cosmic-ray Background.**
  In order to determinate the impact of the uncertainty on the cosmic-ray background, we varied its flux of ±50% from the nominal value. We thus changed the normalization of the background according to:

$$N_0' = N_0 \cdot (1 + \epsilon), \tag{3.7}$$

  where $\epsilon = 0.5$ We then analyzed these data and estimated the errors on the spectral parameters, repeating the simulation for one hundred times and taking the error from the mean value.

- **Galactic Diffuse Emission.**
  As mentioned above we modeled the emission from the Galactic plane central region using a HESS observation (Aharonian et al. 2006a). The best fit spectral model for this observation is a power law whith $N_0 = 1.73 \times 10^{-8}$ TeV^{-1}cm^{-2}s^{-1}sr^{-1} and $\Gamma = 2.29$ with the associated errors $\sigma_{N_0} = (\pm 0.13_{stat} \pm 0.35_{syst}) \times 10^{-8}$ TeV^{-1}cm^{-2}s^{-1}sr^{-1} and $\sigma_\Gamma = \pm 0.07_{stat} \pm 0.20_{syst}$. Using these errors we calculate an optimistic/pessimistic spectrum from the Galactic center from:

$$F_{pess,opt} = F(E) \pm \sqrt{\left(\frac{\partial F}{\partial N_0}\right)^2 \sigma_{N_0}^2 + \left(\frac{\partial F}{\partial \Gamma}\right)^2 \sigma_\Gamma^2}, \tag{3.8}$$

  where $F(E)$ is the best fit value of the flux, the pessimistic case F_{pess} corresponds to the sign + and the optimistic case F_{opt} to the sign -. This is an approximation of the error propagation formula (we lack all the information on the full covariance matrix from the likelihood analysis). The spectrum is shown in Figure 3.9. We

have then analyzed these perturbed data and measured the associated errors. We repeated the analysis using the pessimistic and optimistic estimate of the spectrum and used the spectral parameters of the source inferred in the two cases to estimate the errors induced by this systematic uncertainty on it.

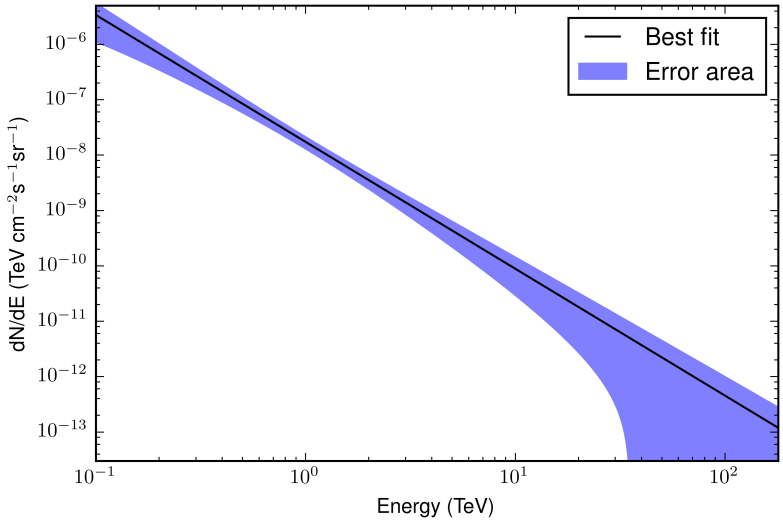

Figure 3.9: Average spectrum (per steradian) of the Galactic plane near the center region (between $359.2° < l < 0.8°$ and $|b| < 0.3°$) as measured by the HESS collaboration (Aharonian et al. 2006a). The shaded area correspond to the error boundary of the HESS measurements, in which both statistical and systematic errors are taken in account.

3.5 Systematic error estimation results

In Table 3.3 we report the values of the systematic errors, computed from the difference between the "Nominal value" (values computed without perturbing the data) and the values obtained as explained in the previous section.

The instrumental systematic uncertainties dominate over the background related sources of error. This is shown in Figure 3.10 where we plot the errors as function of energy, assuming a power law spectrum. While the systematics act differently at different energies, the background related uncertainties are always small. In the low energy range (where the source has the highest flux) the instrumental uncertainties dominate and are at the same level as the statistical errors, while in the higher energy range, the decrease of the sensitivity of CTA-South leads to an increase of the statistical errors. The behavior of

the statistical error yields a good representation of the sensitivity limit of the CTA-South array.

Although the errors reported here are probably overestimated (especially the instrumental ones), this analysis provides a good clue on the order of magnitude of the expected systematic uncertainties. According to the results of our analysis, the background related uncertainties are negligible in comparison with the other sources of uncertainty.

Table 3.3: Systematic errors measured using the deviation of the perturbed values from the nominal ones, as explained in the text. We report for comparison also the statistical errors computed from the likelihood analysis made with *ctools*.

Statistical errors	N_0[a]	δN_0[a]	$\delta N_0/N_0$	Γ	$\delta\Gamma$	$\delta\Gamma/\Gamma$
Nominal value	8.820×10^{-13}	7.322×10^{-15}	0.830%	2.306	0.006	0.251%
Systematic errors	N_0'[a]	δN_0[a]	$\delta N_0/N_0$	Γ'	$\delta\Gamma$	$\delta\Gamma/\Gamma$
A'_{eff}(Constant − 5%)	9.351×10^{-13}	5.309×10^{-14}	6.019%	2.309	0.003	0.123%
A'_{eff}(Constant + 5%)	8.334×10^{-13}	-4.865×10^{-14}	−5.516%	2.310	0.004	0.177%
A'_{eff}(Eq. 5 +5%)	8.846×10^{-13}	2.632×10^{-15}	0.298%	2.333	0.027	1.179%
En. scale (−6%)	8.555×10^{-13}	-2.656×10^{-14}	−3.012%	2.320	0.014	0.613%
En. scale (+6%)	9.055×10^{-13}	2.351×10^{-14}	2.666%	2.303	−0.003	−0.128%
Cosmic-ray (−50%)	8.837×10^{-13}	1.668×10^{-15}	0.189%	2.302	−0.042	−0.079%
Cosmic-ray (+50%)	8.882×10^{-13}	6.184×10^{-15}	0.701%	2.309	0.003	0.117%
Gal. Diffuse (Opt.)	8.807×10^{-13}	-1.277×10^{-15}	−0.145%	2.302	−0.004	−0.166%
Gal. Diffuse (Pess.)	8.807×10^{-13}	-1.315×10^{-15}	−0.149%	2.308	0.002	0.082%

[a] N_0 and δN_0 in unit of $\mathrm{TeV}^{-1}\mathrm{cm}^{-2}\mathrm{s}^{-1}$

3.6 Conclusions

In this work, we have studied a young PWN inside SNR G0.9+0.1 that is projected near the Galactic Center. Despite the high background rate, the crowded field and the faintness of the source we have shown that the CTA-South array allows us to study this region, and in particular the PWN, in great detail.

In our analysis of SNR G0.9+0.1 we choose as observing time for the simulations 200 hours in order to obtain very accurate data. This observing time can be obtained because of the projected position of this source, close to the Galactic Center. As reported in the book "Science with the Cherenkov Telescope Array" (CTA Consortium 2019), the Galactic Center is one of the Key Science Project (KSP) for the CTA collaboration. This

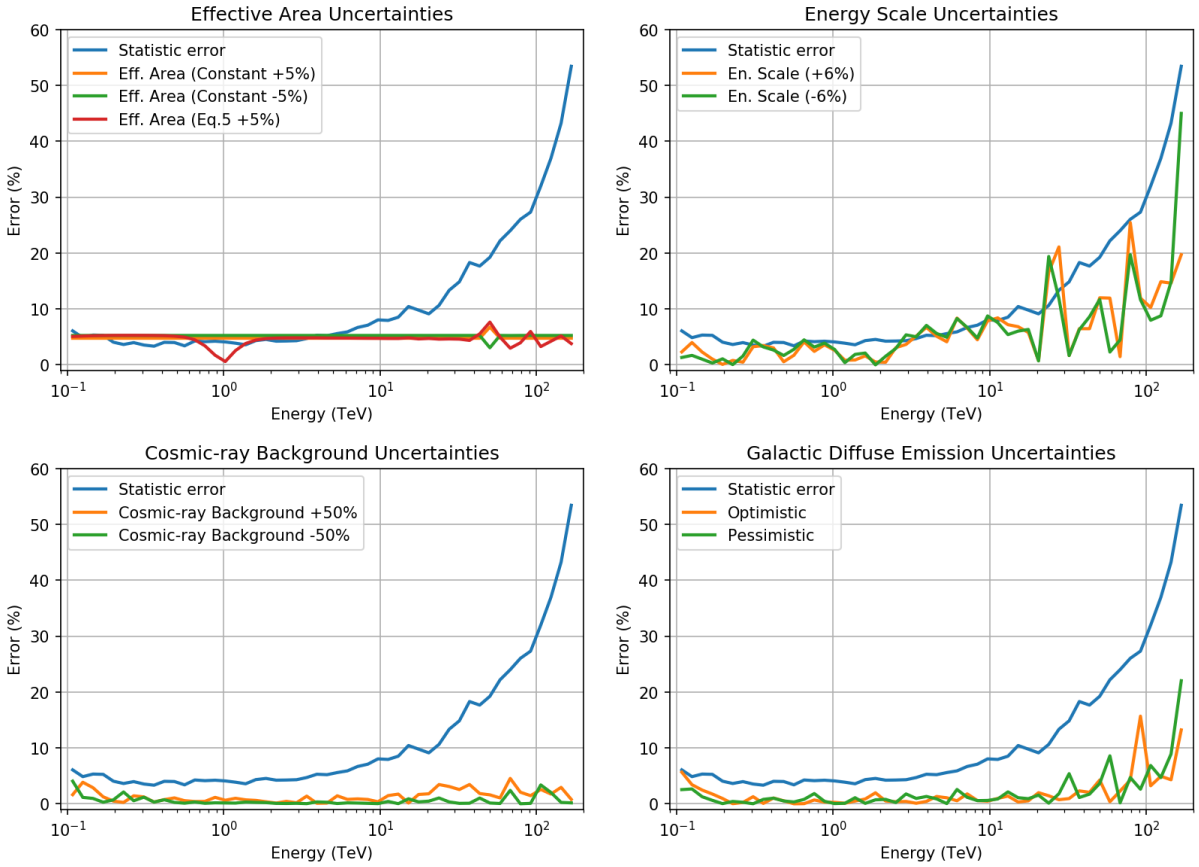

Figure 3.10: Fractional error on the CTA spectrum as function of photon energy, measured assuming a power law model for SNR G0.9+0.1. In the low energy range (where CTA-South will have the best sensitivity) the instrumental uncertainties are dominant, while in the higher energy range the decrease of the sensitivity of the array leads to an increase of the statistical errors. The background related uncertainties are very low at all energies.

core program will run for the first 3 years of observations with CTA and will produce 525 hours of data from the region of SNR G0.9+0.1. The 200 hours of time needed for our study will be reached after $\sim$ 1 year after the beginning of the observations with CTA-South.

Our spatial analysis of SNR G0.9+0.1 shows that if the VHE emission region is larger than $\sim$ 1.5 arcmin CTA will be able to resolve it, leading to a measurement of the size of the nebula in the VHE band. Furthermore, our spectral analysis shows that it would be possible to distinguish different spectral models and calculate the cut-off energy, if present. We could also detect the source at energies higher then 100 TeV if the spectrum is a pure power law.

We performed also a detailed analysis of the systematic errors and found that the systematics related to the instrumental uncertainties dominate, especially at low energies. Despite these errors maybe somewhat overestimated, they provide at least an order of magnitude estimate of the uncertainties that is crucial for our subsequent analysis.

Chapter 4

Modeling the emission of PWNe with CTA data - The case of SNR G0.9+0.1

4.1 Introduction

PWNe are important laboratories to test the processes responsible for the acceleration of charged particles. To this end it is crucial to compare real (or simulated data) with precise and physically motivated models.

In the previous Chapter, we adopted some phenomenological models to describe the morphological and spectral properties at TeV energies of SNR G0.9.01. To improve our understanding of this source, and to investigate how CTA data could increase our knowledge of the physical processes acting in young PWNe, in this Chapter we will present the implementation of a physical model that attempts to reproduce their dynamics and MWL emission. Indeed, reproducing the broad-band spectrum, from the radio band up to γ-rays, of these sources, requires a dynamical model that describes the evolution of the population of the emitting electrons inside the PWN.

A one-zone time-dependent leptonic model is often adopted. In this model the main emitting particles are a population of electrons that evolves with time and the nebula is approximated as a sphere where the electrons are uniformly distributed.

This approach has been developed by several authors (e.g. Venter & de Jager 2007; Qiao et al. 2009; Zhang et al. 2008; Fang & Zhang 2010; Tanaka & Takahara 2010, 2011; Bucciantini et al. 2011; Martín et al. 2012, 2016; Torres et al. 2014; van Rensburg et al. 2018). In this work, we follow the approach presented by Gelfand et al. (2009). We also test the result of our implementation for the PWN in SNR G0.9+0.1 against those obtained by Zhu et al. (2018) and Torres et al. (2014).

4.2 The model

The distribution and the evolution of the electronic population inside the nebula is described by an energy-diffusion equation. The general form of this equation (see equation B.1) and the meaning of all the terms of the equation are described in Appendix B. The simplified form used in this work is as follow:

$$\frac{\partial N(E,t)}{\partial t} = Q(E,t) - \frac{\partial}{\partial E}[b(E)N(E,t)] - \frac{N(E,t)}{\tau(E,t)}. \tag{4.1}$$

The typical shape adopted for the injection spectrum of the particles is a broken power law. Other types of injection spectra have been proposed but all somehow fail to reproduce the observed spectrum or are difficult to motivate (see the discussion in Gelfand 2017). The broken power law spectrum can reproduce well the different slopes of the synchrotron spectrum observed in many PWNe, as the Crab Nebula (Atoyan & Aharonian 1996), in the radio and X-ray bands. We then assume (Tanaka & Takahara 2010; Bucciantini et al. 2011; Martín et al. 2012; Torres et al. 2013a; Zhu et al. 2015):

$$Q(E,t) = Q_0(t) \begin{cases} (E/E_b)^{-\alpha_1} & \text{for } E \leq E_b \\ (E/E_b)^{-\alpha_2} & \text{for } E > E_b \end{cases}, \tag{4.2}$$

where $Q_0(t)$ is a normalization factor determined from the fraction of the spin-down luminosity $L(t)$ of the pulsar that goes in particles energy. If we write the spin-down luminosity of the pulsar in the form

$$L(t) = L_0 \left(1 + \frac{t}{\tau_0}\right)^{-\frac{(n+1)}{(n-1)}}, \tag{4.3}$$

where L_0 is the initial spin-down luminosity, τ_0 the initial spin-down timescale and n the braking index (Gaensler & Slane 2006), we can find the normalization factor $Q_0(t)$ from:

$$(1-\eta_B)L(t) = \int_{E_{min}}^{E_{max}} EQ(E,t)dE. \tag{4.4}$$

Here the constant η_B, the magnetic fraction of the nebula (Martín et al. 2016), is the fraction of the spin-down luminosity that goes into the electromagnetic field (Poynting flux)[1]. While $1-\eta_B$ is the part that goes in the kinetic energy of the electrons.

The escape timescale $\tau(E,t)$ is computed from the assumption that particles can escape from the nebula because of diffusion. This diffusion inside a PWN arises from the interaction of particles with irregularities in the magnetic field (Vorster et al. 2013). Assuming that the diffusion of plasma across the negative field in the PWN follows Bohm law, $\tau(E,t)$ is given by:

$$\tau_{esc} = \frac{eB(t)R_{pwn}^2(t)}{2Ec^2}, \tag{4.5}$$

where R_{pwn} is the radius of the PWN.

The second term in equation 4.1 includes the energy variation because of synchrotron radiation, IC scattering, Self-Synchrotron Compton (SSC) and adiabatic losses (Ginzburg & Syrovatskii 1964).

The minimum energy E_{min} of the injected electrons is a free parameter in this model and we choose to select a value equal to the electrons rest mass energy (0.51 MeV). On the other hand, the maximum electron energy E_{max} has to be determined because it is strictly related to the accelerations processes at the termination shock. There are different ways to calculate E_{max}. For high magnetic field strengths (for very young PWNe) one can estimate it by balancing synchrotron losses acceleration gains (de Jager et al. 1996). For lower magnetic field strengths, one needs to consider that the highest energy particle must have a gyro-radius comparable to the shock radius to participate in the acceleration process (de Jager & Djannati-Ataï 2009). Another possibility for estimating E_{max} is to consider the electric potential of the neutron star magnetosphere (Bucciantini et al. 2011; Granot et al. 2017) and determine the maximum energy that electrons can gain while moving through the polar cap potential. We computed E_{max} considering all three different

[1]This is not to be confused with the so called magnetization parameter $\sigma(t) = \eta_B/(1-\eta_B)$.

approaches and adopted the second one because the other two yield unreasonably high values. The second condition is equivalent to impose that the Larmor radius R_L must be a fraction $\epsilon < 1$ (ϵ containment factor) of the termination shock radius R_S. The Larmor radius can be written as

$$R_L = \frac{E_{max}}{eB_S}, \tag{4.6}$$

and so the maximum energy becomes:

$$E_{max} = \epsilon e B_S R_S. \tag{4.7}$$

Finally we need an expression for the magnetic field at the termination shock B_S. From Kennel & Coroniti (1984a) the post-shock field is expressed as:

$$B_S = \kappa \sqrt{\eta_B \frac{L(t)}{c}} \frac{1}{R_S}, \tag{4.8}$$

where κ is the magnetic field compression ratio taken equal to 3 (strong shock condition). The final expression for the maximum electron energy is then:

$$E_{max} = 3e\epsilon \sqrt{\eta_B \frac{L(t)}{c}}. \tag{4.9}$$

To compute the evolution of the magnetic field we consider the adiabatic losses due to expansion work done by the nebula on the surroundings and the energy input from the pulsar wind (Pacini & Salvati 1973; Torres et al. 2013a; Gelfand et al. 2009):

$$\frac{dW_B(t)}{dt} = \eta_B L(t) - \frac{W_B(t)}{R_{pwn}(t)} \frac{dR_{pwn}}{dt}, \tag{4.10}$$

where $W_B = (4\pi/3) R_{pwn}^3(t) B^2(t)/(8\pi)$ is the total magnetic energy. The integration over time of this equation leads to

$$B(t) = \frac{1}{R_{pwn}^2(t)} \sqrt{6\eta_B \int_0^t L(t') R_{pwn}(t') dt'}. \tag{4.11}$$

The last ingredient of the model is the dynamical evolution (radius and the expansion velocity) of the PWN. We compute it with an iterative approach that is explained in

appendix C[2].

The diffusion-loss equation (equation 4.1) is solved using a freely available code, called GAMERA[3] (Hahn 2015). Once the evolution of the particle spectrum is computed, it is possible to derive directly the photon spectrum with GAMERA. The synchrotron spectrum is computed considering an isotropic pitch angle distribution of the electrons as in Ghisellini et al. (1988). The IC emission is computed using the full Klein-Nishina cross-section (Blumenthal & Gould 1970) on a background radiation field (generally composed by the CMB photons and two Infra-Red components). Synchrotron Self-Compton (SSC) emission is also included (Atoyan & Aharonian 1996).

4.2.1 Model test and comparison

The model has several parameters that constrain various physical properties of the system. Since some of them are significantly degenerate, as the distance and the age of the system, we decide to fix them by choosing reliable value as reported in the literature (age, distance, energy of the SN explosion, density of the interstellar medium and photon background, see Table 4.1). In addition to these parameters, several parameters of the pulsar (spin-down luminosity, period derivative, characteristic age) are also known and are reported in Table 4.1. The remaining parameters are those related to the spectrum of the injected electrons population (the break energy and the two indices of the broken power law), the magnetic fraction of the nebula and the containment factor.

When fitting the data we leave the injection parameters free to vary. The only exceptions are α_1 and E_b that can be constrained from the radio and X-ray data. The fitting procedure and error estimation of the fitted parameters are reported in Appendix D.

We tested our implementation against the results presented in Zhu et al. (2018) and Torres et al. (2014), selecting the same set of data for consistency. The radio data are taken from Dubner et al. (2008), the X-ray data from Porquet et al. (2003) and the current VHE data from Aharonian et al. (2005b). We note that, differently to our work, Torres

[2]The caveats of this iterative approach are described at the end of appendix C.

[3]libgamera.github.io/GAMERA/docs/main_page.html

et al. (2014) treated the dynamical evolution of the nebula in a simplified way assuming free expansion as in van der Swaluw et al. (2001) and not considering the effects of the electron pitch angle.

The values of the fitted parameters and their comparison with those found in Zhu et al. (2018) and Torres et al. (2014) are reported in Table 4.1. Results are consistent, however, the fixed value of the ejected masses M_{ej} need to be physically adjusted. The difference with the result of Torres et al. (2014) is understandable because they treat the dynamical evolution in a simplified way. The difference with Zhu et al. (2018) arises probably from some differences in the implementation adopted to solve Equation 4.1. However, this difference is only of $\sim 40\%$, not very significant if we consider the uncertainty on the knowledge of this parameter.

We emphasize that the parameter ϵ is loosely constrained because the data do not cover the part of the spectrum where the effects of this parameter are more evident (i.e. in the high energy tails of the synchrotron and IC peaks). Is possible to see this effect in Figure 4.1 where we vary only ϵ between 0.02 and 0.98 with a constant step of 0.04. This parameter is only constrained to be > 0.1. We then took $\epsilon = 0.25$ as reference value for all the models in the subsequent analysis.

Figure 4.2 shows the final best fit electron and photon spectra. The reduced chi-square of the fit is $\chi^2_\nu = 1.1$.

4.3 Fit of simulated CTA data

We applied this model of the PWN evolution to the various simulated spectra of SNR G0.9+0.1 reported in Section 3.3.2, assuming that most of the simulated VHE emission comes from the central PWN. The spectral range is limited at 200 GeV to be consistent with the lower limit of the HESS data and we rebin the spectrum with 10 bins. However, depending on the spectral shape, the spectrum can have less than 10 bins since at high energies there may be no photons.

The results of the model fit are shown in Table 4.2 and in Figures 4.3-4.4-4.5. The errors on the γ-ray data-points includes also the systematic errors computed in the previous section.

Table 4.1: Fixed and fitted parameters of the model in comparison with those of Zhu et al. (2018) and (Torres et al. 2014, Model 2). Dots mean that the same value is adopted.

	This work	Zhu et al. (2018)	Torres et al. (2014)	Notes
Pulsar and SN parameters (fixed)				
P (ms)	52.2	...	...	Camilo et al. (2009)
$\dot{P}$ (s s^{-1})	1.56×10^{-13}	...	...	Camilo et al. (2009)
τ_c (yr)	5305	...	...	$P/(n-1)\dot{P}$
n	3	...	...	fixed at the standard braking index
$L(t)$ (erg/s)	4.32×10^{37}	...	...	Camilo et al. (2009)
t_{age} (yr)	3000	...	...	estimated[a]
τ_0 (yr)	2305	...	...	$[2\tau_c/(n-1)] - t_{age}$
L_0 (erg/s)	2.29×10^{38}	...	...	equation 4.3
M_{ej} ($M_\odot$)	9	14	17	estimated[a]
E_{sn} (erg)	10^{51}	...	...	estimated[a]
d (kpc)	13.3	...	13.	H. E. S. S. Collaboration et al. (2018b)
Environment parameters (fixed)				
n_h (cm^3)	0.01	...	1.	Zhu et al. (2018)
T_{CMB} (K)	2.7	...	...	Longair (2008)
U_{CMB} (ev/cm^3)	0.25	...	...	Longair (2008)
T_{FIR} (K)	30	...	...	Torres et al. (2014)
U_{FIR} (ev/cm^3)	3.8	...	...	Torres et al. (2014)
T_{NIR} (K)	3000	...	...	Torres et al. (2014)
U_{NIR} (ev/cm^3)	25	...	...	Torres et al. (2014)
Injection parameters				
E_b (TeV)	0.045	...	0.026	Zhu et al. (2018)
α_1	1.1	...	1.2	Zhu et al. (2018)
α_2	2.523 ± 0.022	2.52 ± 0.02	2.5	fitted
η_B	0.0313 ± 0.0055	0.029 ± 0.004	0.02	fitted
ϵ	> 0.10	0.25 ± 0.08	0.2	fitted
PWN parameters[b]				
R_{pwn} (pc)	3.46 ± 0.01	3.51	3.8	iterative procedure in Appendix C
B (μG)	$21.89^{+1.93}_{-2.08}$	$20.29^{+1.86}_{-1.93}$	15	equation 4.11
E_{max} (TeV)	> 600	1452^{+600}_{-535}	971	equation 4.9

[a] t_{age}, M_{ej} and E_{SN} taken in order to obtain a nebula of $\sim 2'$ located at 13.3 kpc.
[b] Computed from the PWN dynamics (see Appendix C)

Table 4.2: Results of the fitting procedure with the PWN model adopted in this work for various CTA simulated spectra of SNR G0.9+0.1.

	PLEC 20 TeV	PLEC 30 TeV	PLEC 50 TeV	PLEC 80 TeV	PLEC 100 TeV	PWL
Fitting result						
χ^2_ν	0.8	0.8	0.9	1.2	1.1	2.2
α_2	2.520 ± 0.017	2.509 ± 0.016	2.507 ± 0.016	2.503 ± 0.016	2.500 ± 0.016	2.496 ± 0.016
η_B	0.0310 ± 0.0048	0.0286 ± 0.0045	0.0272 ± 0.0044	0.0257 ± 0.0042	0.0251 ± 0.0041	0.0232 ± 0.0039
R_{pwn} (pc)	3.46 ± 0.01	3.45 ± 0.01	3.45 ± 0.01	3.45 ± 0.01	3.45 ± 0.01	3.45 ± 0.01
B (μG)	$21.81^{+1.53}_{-1.67}$	$20.97^{+1.55}_{-1.59}$	$20.44^{+1.49}_{-1.58}$	$19.87^{+1.41}_{-1.55}$	$19.65^{+1.40}_{-1.52}$	$18.89^{+1.39}_{-1.50}$

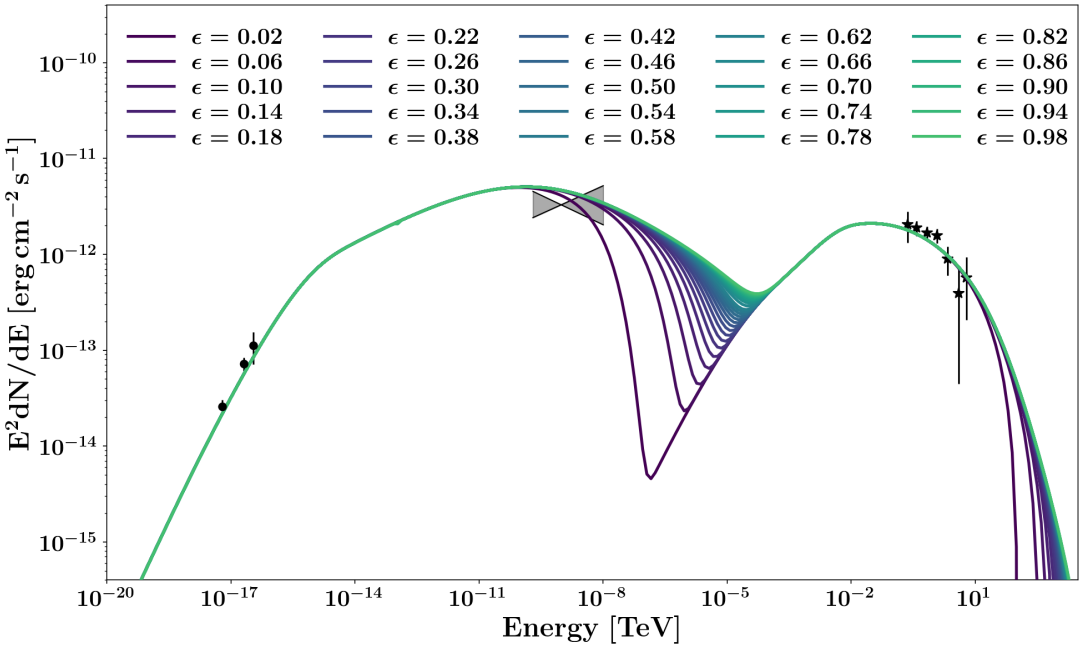

Figure 4.1: SED models for SNR G0.9+0.1 computed for $\alpha = 2.51$ and $\eta_B = 0.031$ fixed while ϵ is varying from 0.02 to 0.98 with step 0.04. We can clearly see that is possible to rule out only really small values of the containment factor ($\epsilon \lesssim 0.1$).

From Figures 4.3-4.4-4.5 we see that the model is always consistent with the data in the lower energy part of the spectrum (the synchrotron emission peak). At high energies the model cannot adjust to a power-law spectral model for any leptonic scenario.

The most interesting result is that the value of the magnetization parameters η_B is fairly well determined and tend to decrease with increasing cut-off energy. In general, the multiwavelength (MWL) spectrum, can constrain it.

Finally, we want to emphasize that the model spectra are not consistent with a pure power law simulated spectrum for every value of the parameters (reduced $\chi^2_\nu \simeq 1.5$). With this model, we are not able to reproduce a power law with no measured cut-off. Even changing the age and distance of the source, it is not possible to find a model that has a power law tail up to 180 TeV. The only possibility would probably be including a hadronic component, but this is beyond the purpose of this work.

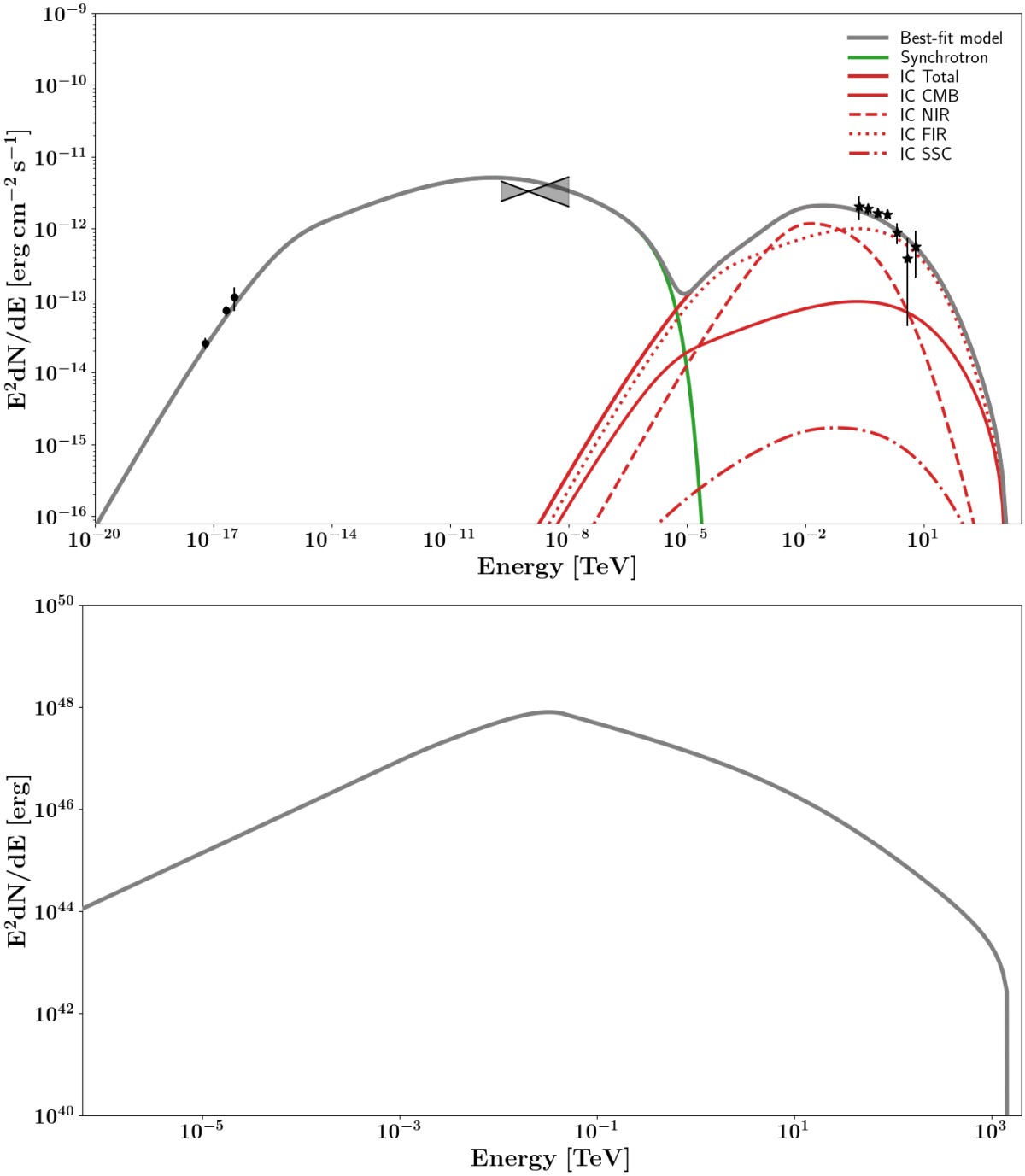

Figure 4.2: Photon (upper panel) and electron (lower panel) SED model for SNR G0.9+0.1 computed with the best fit values reported in Table 4.1. The dataset is the same as in the work of Zhu et al. (2018) (more detail in the text).

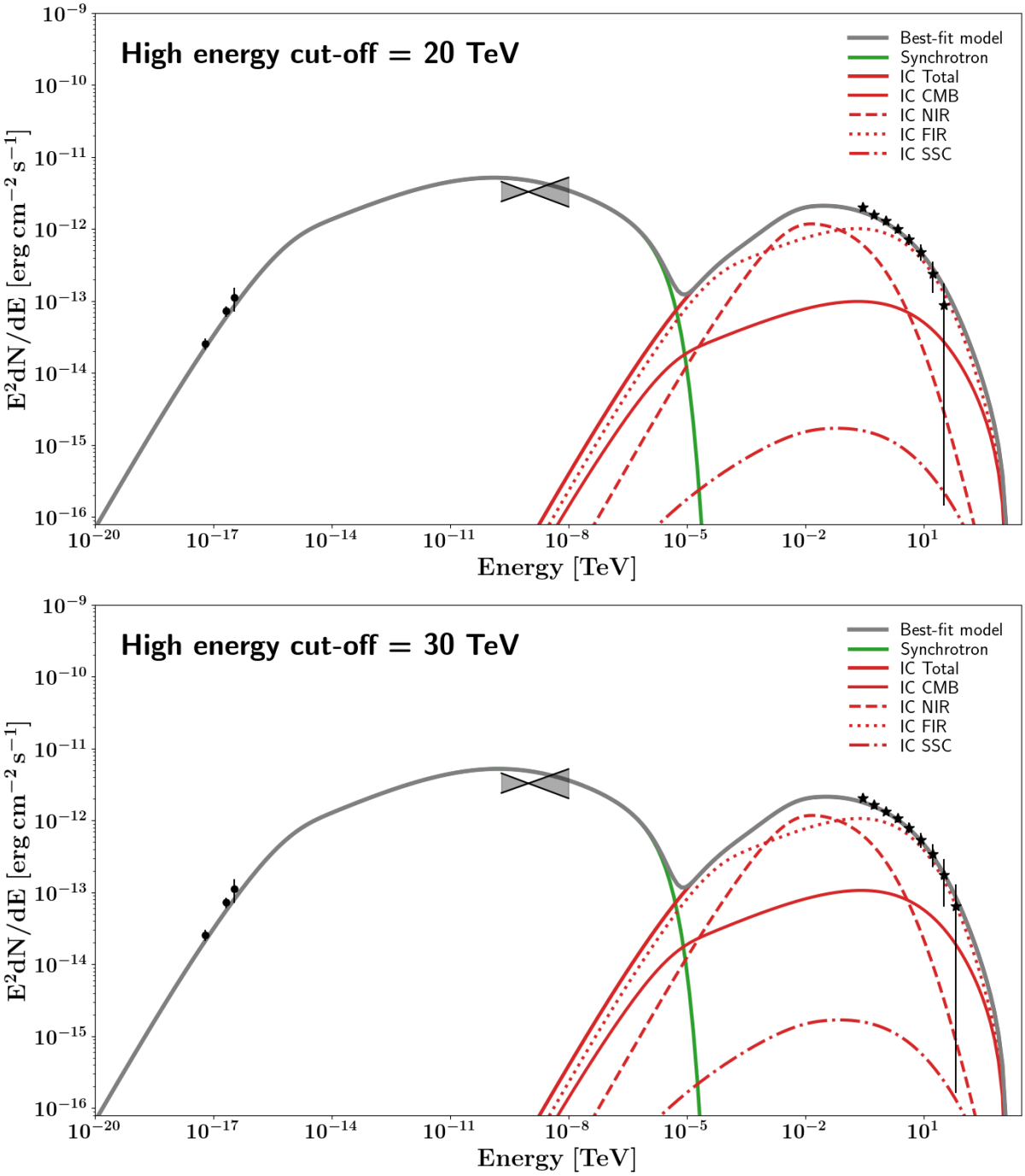

Figure 4.3: Photon SED computed with the best-fitting values reported in Table 4.2 for CTA simulated spectra of SNR G0.9+0.1 with cut-off energy at 20 TeV and 30 TeV.

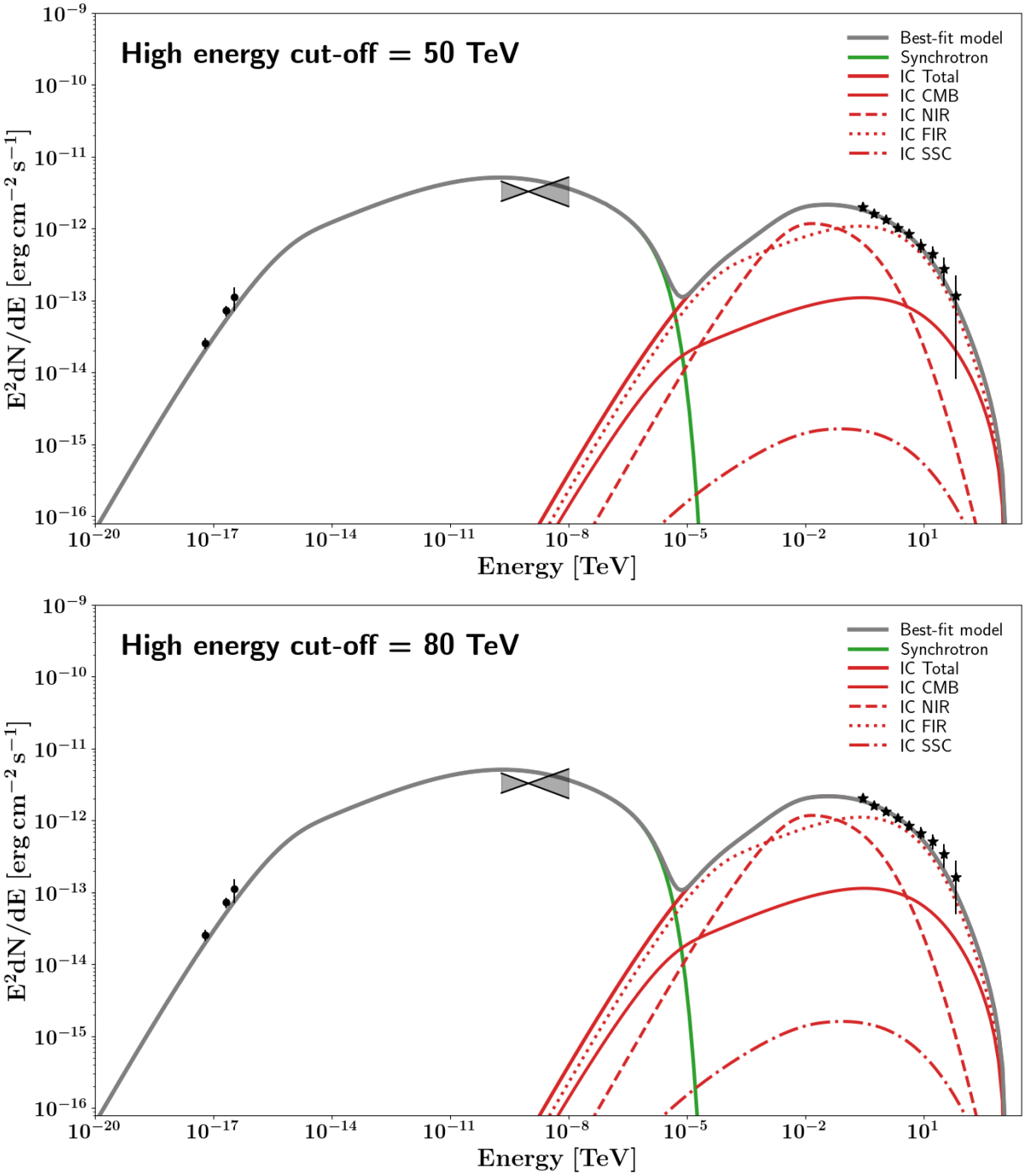

Figure 4.4: Photon SED computed with the best-fitting values reported in Table 4.2 for various CTA simulated spectra of SNR G0.9+0.1 with cut-off energy at 50 TeV and 80 TeV.

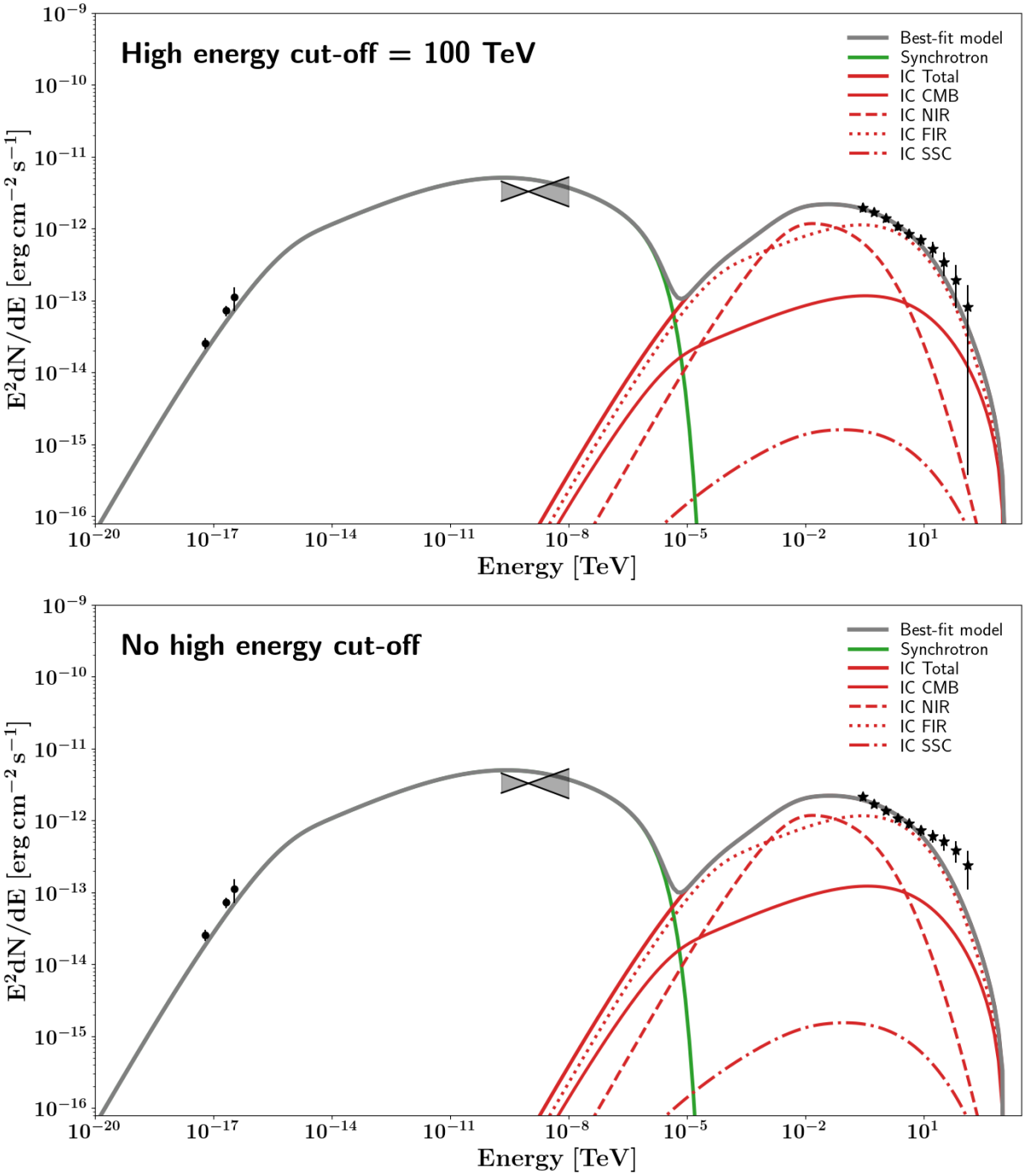

Figure 4.5: Photon SED computed with the best-fitting values reported in Table 4.2 for various CTA simulated spectra of SNR G0.9+0.1 with cut-off energy at 100 TeV and without cut-off.

4.3.1 Impact of the ISRF

We now try to estimate the impact on our results caused by the uncertainties on the Inter-Stellar Radiation Field (ISRF) at the (unknown) position of SNR G0.9+0.1. In principle, a different ISRF can affect our measurement of the parameter of the nebula since the shape of the IC component is dependent on the background radiation. In the previous analysis, we fixed the parameters of the ISRF. It would have been computationally too expensive to let them free.

The density and temperature of the Near-Infrared (NIR) and Far-Infrared (FIR) photon field can vary significantly with the position in the galaxy. Moreover, the spectral shape of this emission can be very different from the simple sum of diluted blackbodies (as assumed in the previous sections).

In order to estimate the effects of different ISRFs, we perform two different approaches. In the first, we check how much the fit differ comparing the case with fixed and free ISRF parameters. To do it we cannot use the full model since the computational time would be too large. We then treated the dynamical evolution in a simplified way, assuming a PWN in a freely expanding SNR (see equation C.4). We then considered the CTA simulated data with a cut-off at 30 TeV and fitted them leaving α_2 and η_B free. We used a Monte Carlo Markov Chain (MCMC) code (*emcee*, Foreman-Mackey et al. 2013) and made 2500 realizations of the spectrum. We obtain results similar to those previously found ($\alpha_2 = 2.516^{+0.019}_{-0.018}$, $\eta_B = 0.0307^{+0.0052}_{-0.0050}$). After this, we repeated the fit but adding as free parameters the energy density and temperature for the IR radiation fields ($T_{FIR}\,, U_{FIR}\,, T_{NIR}\,, U_{NIR}$). We found, in this case, a different ISFR, with a higher energy density of the Far IR component (see Figure 4.6). However, the relevant parameters of the PWN did not change significantly, although their errors increased ($\alpha_2 = 2.593^{+0.049}_{-0.041}$, $\eta_B = 0.0378^{+0.0075}_{-0.0068}$).

In the second approach we considered a more realistic radiation field, like the axisymmetric solution for the ISFR of the Milky Way provided by Popescu et al. (2017), and use it to produce a model with fixed nebula parameters ($\alpha_2 = 2.515$, $\eta_B = 0.0315$). We selected the model reported in the first panel in Figure 9 of Popescu et al. (2017) and rescaled it by a factor ~ 3 to obtain a similar γ-ray flux as the one of SNR G0.9+0.1. We then used this model to simulate an observation made with CTA, extracted the new spectrum and used it in the MCMC fitting procedure as before. We fit the usual two

parameters α_2 and η_B fixing again the values for the ISRF as in the previous analysis and using two diluted blackbodies to model it. We obtained values that are in very good agreement with the ones used for the preparation of this model ($\alpha_2 = 2.524^{+0.020}_{-0.019}$, $\eta_B = 0.0321^{+0.0054}_{-0.0052}$). The results are shown in Figure 4.7. We also tried to fit this model leaving all the parameters for the IR radiation field free to vary and found similar values. While the energy density of the ISRF is crucial to reproduce the IC component in the VHE spectrum, its actual spectral distribution is not, because Comptonized IR photons tend to loose rapidly memory of their initial energy.

4.4 Conclusions

In this Chapter, we have implemented a one-zone time-dependent leptonic model that computes the evolution of a young PWN inside a SNR. Our goal was to simulate on physical grounds the VHE spectra of SNR G0.9+0.1 expected to be observed with CTA, to check what physical information can be obtained from the simulated observations, and to understand what impact CTA will have on our understanding of this PWN.

We first compared our result with those obtained by Zhu et al. (2018) and Torres et al. (2014) using the same data-set. We find good agreement, although it is difficult to constraint the confinement factor ϵ (hence the maximum electron energy in the nebula). Measurements of the flux of SNR G0.9+0.1 at MeV energies would be needed to obtain a precise value for this parameter. However, in the absence of MeV data, an increase of the VHE observing time would help to put constraints on the maximum electron energy because the tail of the IC peak is also sensitive to it at high energies. From the best fit model of the currently available data (Table 4.1) we expect a high energy cut-off between 20 and 30 TeV. This is a measurement that CTA could easily do as shown in Figure 3.7.

It is worth noting that the possibility to put a constraint on the size of the VHE emission region with CTA would be crucial to check the goodness of the model, because we could compare it with the model computed radius and to the size observed at other wavelengths.

We have shown that MWL data will lead to a precise measurement of the magnetization parameter η_B of the nebula. We note also that, with this model, it is not possible to reproduce a pure power law spectrum. If detected with CTA, this would require a drastic

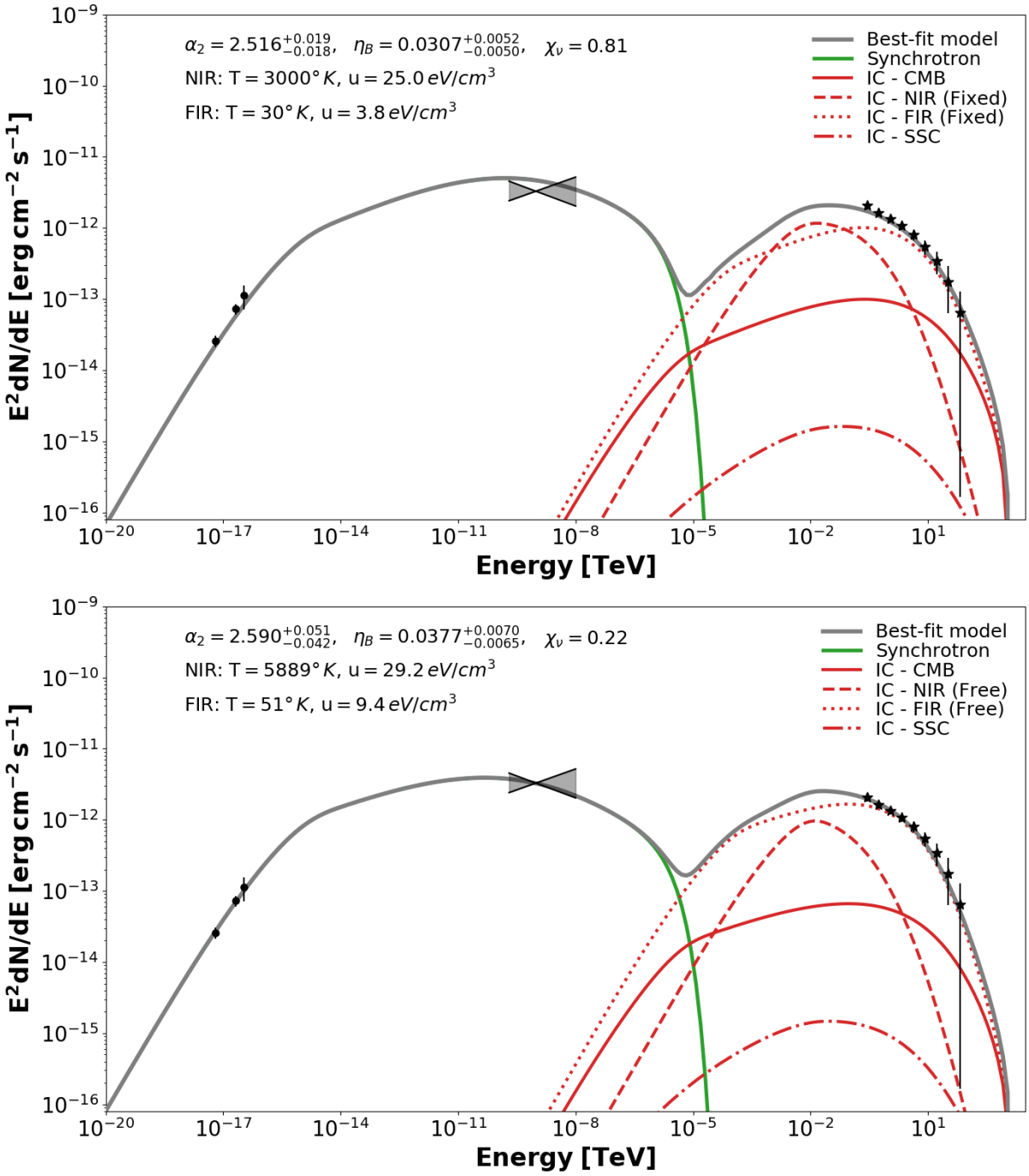

Figure 4.6: Photon SED computed with the fixed ISRF background (left panel) and with the free ISRF background (right panel). The best fit value are computed with an MCMC procedure.

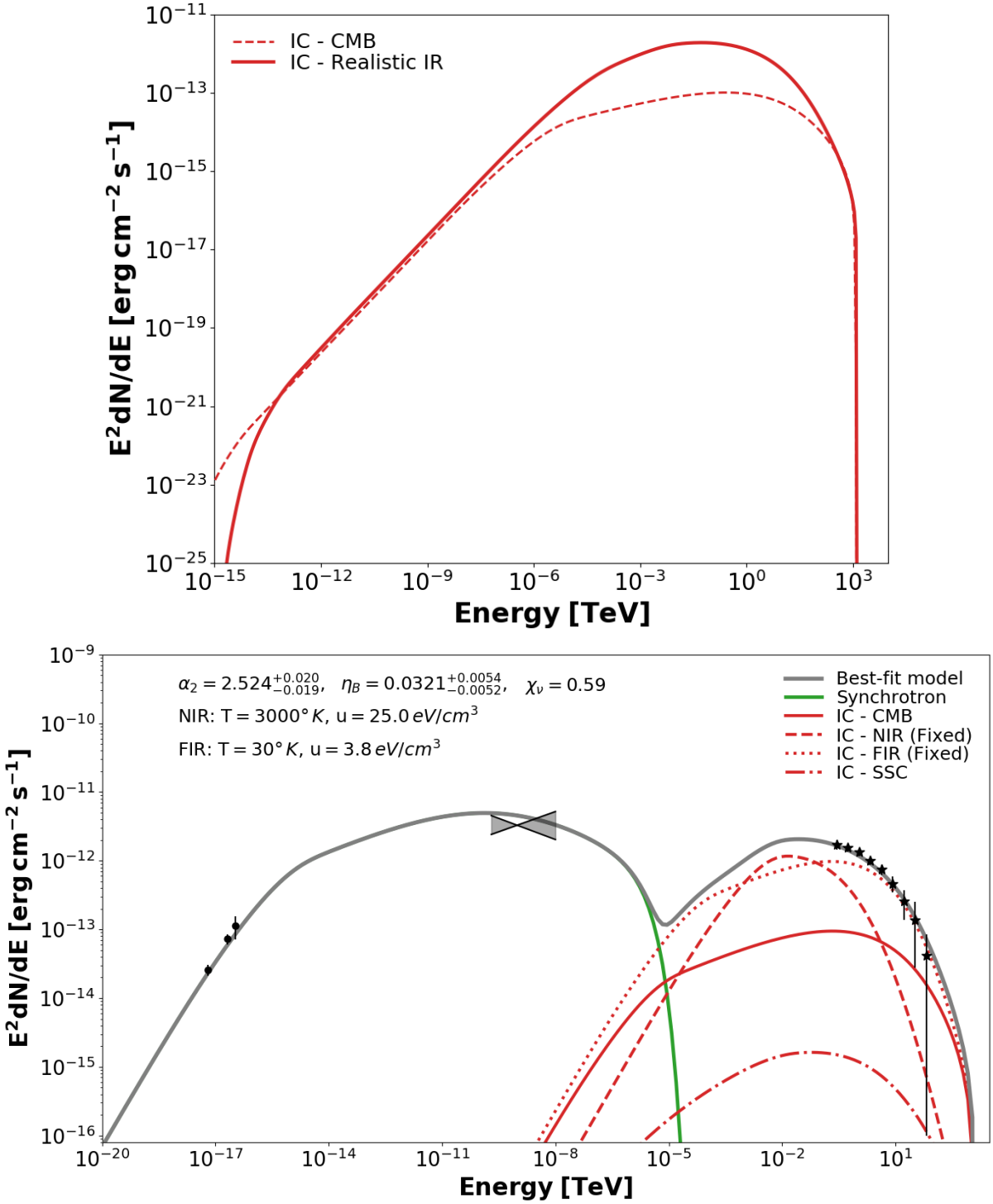

Figure 4.7: In the upper panel we show the realistic (Popescu et al. 2017) IR background reprocessed via IC used as input for the simulation. In the lower panel the photon SED fitted with just two diluted blackblody.

change in the model, such as the introduction of a hadronic component.

We checked also the effects caused by uncertainties on the ISRF field. A fit leaving the ISRF parameters free leads only to small differences in the values of α_2 and η_B. Even approximating a realistic ISRF with only two diluted blackbodies, the values of α_2 and η_B are not significantly affected.

Chapter 5

A complex morphology in a young PWN - The case of MSH 15-52

5.1 Introduction

The PWN in the composite SNR system MSH 15-52 is a quite unique object. It has been extensively observed and studied, through all the electromagnetic spectrum, but its morphology and emission properties are still not fully understood.

The system is powered by one of the most powerful known pulsars (PSR B1509-58), with a spin-down luminosity of 1.8×10^{37}erg s^{-1}, a period derivative of 1.5×10^{-12}s s^{-1} and a characteristic age of about 1600 years (Livingstone & Kaspi 2011). In addiction PSR B1509-58 is one of the few pulsars for which the braking index has been precisely measured ($n = 2.839$; Livingstone et al. 2005).

MSH 15-52 (also called SNR G320.4-01.2) was discovered in the radio band in the early 80's (Caswell et al. 1981). Its pulsar has been detected in the X-rays with the *Einstein* satellite and later on also in the radio band (Seward & Harnden 1982; Manchester et al. 1982). The composite nature of the system has been found later with the observations made with the ROSAT (Trussoni et al. 1996; Brazier & Becker 1997) and ASCA (Tamura et al. 1996) satellites. An elongated structure has been detected around the pulsar and has been interpreted as a PWN (Trussoni et al. 1996). TeV emission associated with the PWN in MSH 15-52 was discovered with HESS (Aharonian et al. 2005a), while

GeV emission and pulsations were discovered with *Fermi*-LAT (Abdo et al. 2010). In the X-rays the source was studied with many other facilities, such as *Beppo*SAX (Mineo et al. 2001), *Chandra* (Gaensler et al. 2002), XMM-*Newton* (Schöck et al. 2010), RXTE (Marsden et al. 1997), *NuSTAR* (An et al. 2014) and INTEGRAL (Forot et al. 2006). In the VHE band the source was observed also with COMPTEL (Kuiper et al. 1999), EGRET (Kuiper et al. 1999) and CANGAROO-III (Nakamori et al. 2008).

The estimated distance of MSH 15-52 computed with HI absorption measurements (Gaensler et al. 1999) is 5.2 ± 1.4 kpc. The distance derived from the dispersion measure of the pulsar, taking the most recent Galactic free electron density model, is $4.4^{+1.3}_{-0.8}$ kpc (Yao et al. 2017), fully consistent with the former.

The age of the system has been debated during the years. As already mentioned, the age of the pulsar derived from the spin-down measurements suggests that the source is $\lesssim 1600$ years old. However, considering standard parameters for the supernova and the ISM, Seward et al. (1983) proposed that the system could be much older ($6 - 21 \times 10^3$ years). To reconcile these two very different estimates there are two possibilities: either the pulsar had an unusual spin-down history (Gvaramadze 2001; Blandford & Romani 1988) or the ISM parameters are not standard. The first case seems to be very unlikely since, from long-term timing observations (Kaspi et al. 1994; Livingstone et al. 2005; Livingstone & Kaspi 2011), there is no evidence that the pulsar is behaving in an unusual way. The second explanation is more likely if the SNR could expand rapidly into a low-density cavity (Seward et al. 1983; Gaensler et al. 2002).

5.1.1 MWL Morphology of the system

The scenario in which the SNR expands in a low-density cavity can explain also the complex morphology of the system, clearly visible in Figure 5.1. In the radio band (red contours in Figure 5.1) two separate sources are detected South-East and North-West from the central pulsar (SE and NW components hereafter). Very faint emission is also observed in the region of the PWN. The SE component is located at a projected distance of 20 ± 2 pc from the pulsar (considering a distance of $d \sim 4.4$ kpc) while the NW component (also known as RCW 89; Rodgers et al. 1960) is much closer to the center, at about 9 ± 2 pc. Gaensler et al. (1999) have interpreted this asymmetry as the result of the interaction of the SNR shell with a medium having different densities in the two directions. Such a

cavity is also expected because of the presence of other massive stars in the region (Lortet et al. 1987). Gaensler et al. (1999) proposed that the SN that generated the system had a typical explosion energy ($E_{sn} \sim 1 - 2 \times 10^{51}$erg) but low-mass ejecta ($M_{ej} \sim 1.5 M_{\odot}$), such as in the case of a helium star. The low density of the cavity can also account for the faintness of the PWN in the radio band (Bhattacharya 1990). Using the radio data of Gaensler et al. (1999) and Whiteoak & Green (1996) Gaensler et al. (2002) provide an approximate estimate of the flux of the PWN in the radio band of about 2 ± 1 Jy at 0.8 and 1.4 GHz.

The bright emission in the X-ray band is more concentrated in the central region of MSH 15-52 (white contours in Figure 5.1). However, faint diffuse emission can be seen over the entire area. This diffuse emission can be interpreted as thermal emission from the SNR (Trussoni et al. 1996). The central non-thermal emission region (inside the orange circle in Figure 5.1) corresponds to the PWN. It is synchrotron radiation with knots, bright arc, and jet-like structures (Gaensler et al. 2002; Yatsu et al. 2009), similar to those observed in the Crab nebula (Dubner et al. 2017). A ring-like feature is clearly visible around the pulsar in high-spatial-resolution images taken with XMM-*Newton* and *Chandra*, that can be the termination shock of the PWN (Schöck et al. 2010; Yatsu et al. 2009). The Northern part of the bright emission is coincident with the location of RCW 89. It is mostly thermal emission with a very small flux above 3-4 keV (Gaensler et al. 2002; An et al. 2014).

The morphology in the VHE band appears to show some dependence on energy. Observations of the GeV unpulsed emission of MSH 15-52 with *Fermi*-LAT reveal a structure that can be best-fitted with a uniform disk centred south from the pulsar position (yellow circle in Figure 5.1; Abdo et al. 2010). The morphology in the TeV range reported in Aharonian et al. (2005a, color map in Figure 5.1) is best-fitted with an elliptical source, with the centroid SE from the pulsar position. A more recent analysis of the HESS data has shown that this emission can be modeled using the $4 - 7$ keV *Chandra* map multiplied by a function that depends on the radial distance R from the pulsar ($F_{TeV} = F_{Chandra} \times R^{1.31}$) plus an additional Gaussian component (Tsirou et al. 2018). The extra Gaussian component is shown as a black circle in Figure 5.1, in SE direction from the pulsar. It is in good agreement with the *Fermi*-LAT data and contains about 65% of the total flux between 280 GeV and 40 TeV (Tsirou et al. 2018). However, observations with CANGAROO-III, that has a higher lower energy limit than HESS, show that the centroid of the γ-ray emission is consistent with the position of the pulsar (Nakamori

et al. 2008).

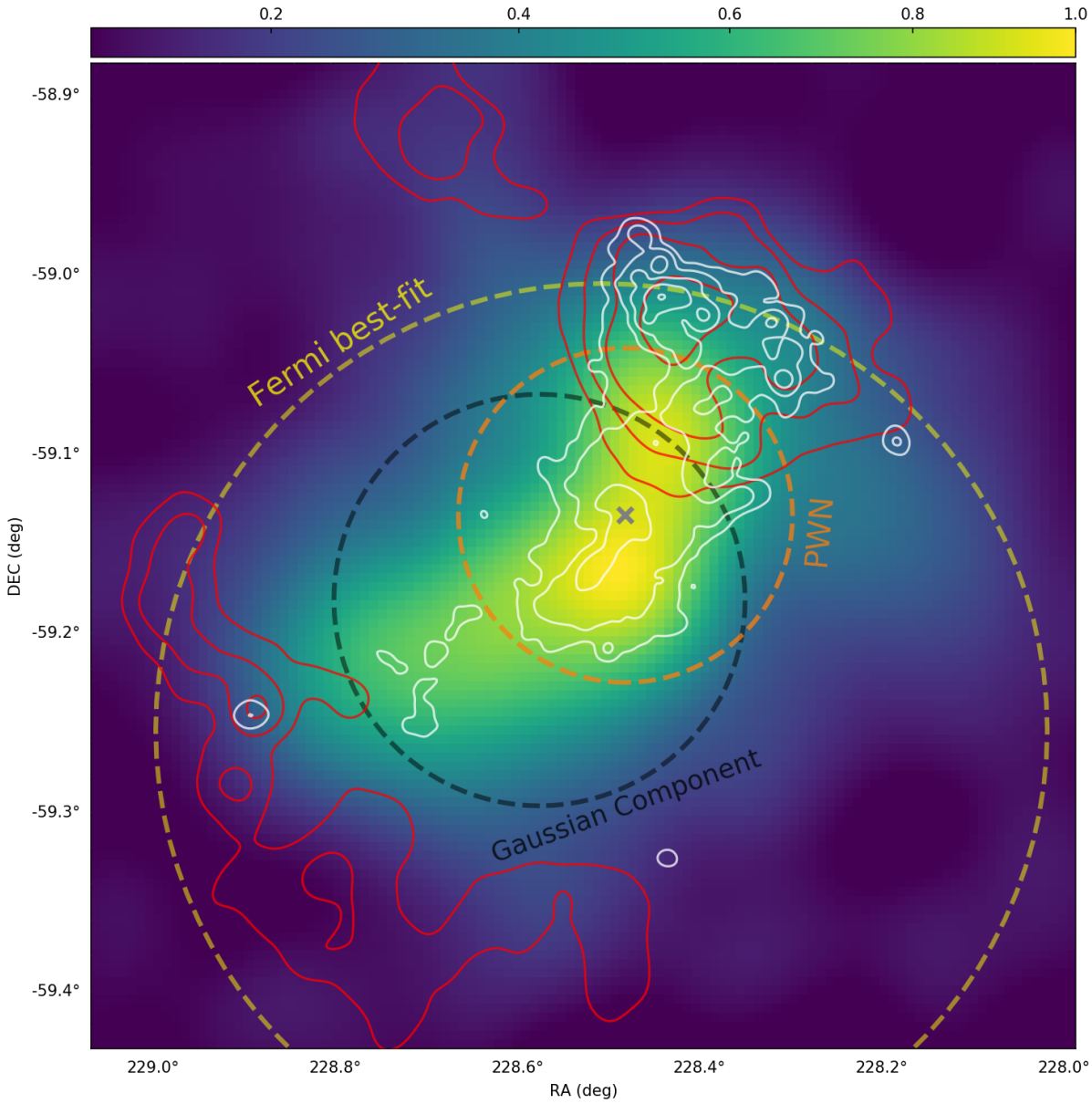

Figure 5.1: MWL morphology of MSH 15-52. The color map is an HESS excess map (Aharonian et al. 2005a) with over imposed the *Chandra* contours (in white; Mineo et al. 2001) and the MOST contours (in red; 843 MHz). The circles in the map indicate: the best-fit of the morphology in the GeV band from a *Fermi*-LAT analysis using a uniform disk (yellow; Abdo et al. 2010), the size of the PWN assumed in our analysis (orange) and the additional Gaussian component needed to model the TeV data (black; Tsirou et al. 2018). The gray cross in the middle of the PWN marks the position of the pulsar PSR B1509-58 (Livingstone & Kaspi 2011).

Many authors have tried to model the multiwavelength data of MSH 15-52 with time-dependent leptonic models. A major limitation of these models is that they needed a fairly accurate estimate of the age of the system because it is possible to find good solutions for different ages. The majority of the models can reproduce well the MWL data assuming an age consistent with that estimated from the pulsar spin-down ($\sim 1400-1700$ years; Zhang et al. 2008; Fang & Zhang 2010; Bucciantini et al. 2011; Torres et al. 2014; Lu et al. 2017). However, other authors (e.g. Zhu et al. 2018) assume that the source is older. In this case, consistent results are found under the hypothesis that the spin-down history of the pulsar is not typical, which is at variance with the findings obtained from the long term observations of the pulsar rotational history (Livingstone & Kaspi 2011). Another significant limitation of these models is the assumption of spherical symmetry, that is clearly not adequate to describe faithfully the morphology of this source. These approximate models can produce reasonable estimates, although some discrepancies may arise. For example, in some models, the radius of the PWN is not completely consistent with observations (Zhang et al. 2008; Fang & Zhang 2010; Torres et al. 2014). If the emission of the PWN is modeled using the *Chandra* map above 3-4 keV, the nebula has an extension of at least 5-6 pc (considering a distance of 4.4 kpc), as found by Bucciantini et al. (2011) and Lu et al. (2017). Finally, these models do not take into account the existence of an extended component SE of the PWN as reported by Tsirou et al. (2018). Only Schöck et al. (2010) modeled the MWL emission of the PWN considering the sole central region (the orange circle in Figure 5.1) and rescaling the TeV flux. However, they did not take into account for possible differences of the spectral shape between the various regions of the source.

The scope of this work is to perform perspective studies of MSH 15-52 with CTA-South, using the one-zone time-dependent leptonic model described in the previous chapter and the most recent findings for this source. In the following, we will first present some test cases for MSH 15-52, with the multiwavelength SED fitting on the presently available data, and then, using the GeV-TeV data extracted from the test cases, we will analyze simulated observations performed with CTA.

5.2 Description of the test cases

In the following we make use of the one-zone time-dependent model described in section 4 to compute the GeV-TeV spectrum of MSH 15-52. The best-fitting spectrum is then used as a template model for the CTA simulations carried out with *ctools* (Knödlseder et al. 2016). In order to save computational time, we used the simplified version of the dynamical evolution code (as done in section 4.3.1), assuming the PWN in a freely expanding SNR (see equation C.4).

The parameters are fixed from a fit of the presently available data:

- Radio data from Gaensler et al. (2002), even if the values are very uncertain.
- X-ray data from *Beppo*SAX (Mineo et al. 2001) and INTEGRAL (Forot et al. 2006). Forot et al. (2006) report also a possible spectral cut-off around 160 keV (at 2.9σ confidence level), although they could only measure an upper-limit to the flux in the energy range 130-200 keV.
- GeV data from *Fermi*-LAT (Abdo et al. 2010).
- TeV data from the HESS detection paper of MSH 15-52 (Aharonian et al. 2005a).

To find the best-fit values and confidence levels of the model parameters we applied an MCMC procedure (2500 realizations) using the package *emcee* (Foreman-Mackey et al. 2013).

5.2.1 Test case 1

The first test case (hereafter TC1) considered assumes that the VHE emission comes from the sole PWN. In order to obtain a radius of ~ 6 pc for the PWN we need a SN explosion energy $E_{sn} = 3 \times 10^{51}$ erg and an ejected mass $M_{ej} = 5 M_{\odot}$.

For MSH 15-52 we did not fix the values of the density of the ISRF at the values found in GALPROP (Porter et al. 2006), since the resulting VHE flux is not large enough to fit the observed data. We instead fixed the temperature and density of the FIR field and left free to vary the parameters of the NIR field. In fact in this region, there are massive stars whose reprocessed light can contribute to the IR background, such as the

O star Muzzio 10 (Muzzio & Celotti de Frecha 1979; Koo et al. 2011). In addition, as for SNR G0.9+0.1, we leave free to vary also the parameters η_B and α_2. In Table 5.1 we list all the fixed parameters and the best-fitting values of all the free parameters, with the related uncertainties.

The best-fit MWL spectrum of MSH 15-52 is shown in the upper panel of Figure 5.2. In this case, we need a rather high value of the magnetization parameter ($\eta_B = 0.194^{+0.022}_{-0.034}$) because, although the nebula is young, it has a large extension. Reproducing the observed flux in the synchrotron peak requires a value of the magnetic field around $15 - 20\,\mu$G[1] (in agreement with other estimates, e.g. Abdo et al. 2010; Aharonian et al. 2005a; Nakamori et al. 2008; Forot et al. 2006; Gaensler et al. 2002; Lu et al. 2017).

The values obtained for the density of the NIR background is very high ($U_{NIR} = 68^{+24}_{-19}$ eV/cm^3), about 30 times higher than the value inferred from GALPROP. As already pointed out in section 4.3.1, the values of the ISRFs needed to explain the TeV emission of PWNe can be significantly different from the average values estimated in other ways. However, the value obtained for MSH 15-52 seems difficult to explain even if we consider the actual contribution of the stars in the region. Other authors proposed a background component with a lower temperature and a lower density (T= 400 K, U= 20 eV/cm^3), that can originate from the reprocessing of stellar light in the SNR shell (Bucciantini et al. 2011; Torres et al. 2014). However, in those assumptions, the density is 10 times higher than the one provided by GALPROP. Furthermore, we found that we need a temperature higher than 400 K to better fit the GeV data.

We tried also to estimate the containment factor ϵ (related to the maximum electron energy E_{max}), as done for SNR G0.9+0.1. For MSH 15-52 there is evidence of a possible break in the spectrum around 160 keV (at 2.9σ; Forot et al. 2006). We then tried to change the value of ϵ to reproduce it. Notably, we are not able to reproduce such a fast drop in the spectrum. Values $\epsilon \ll 0.1$ are needed to account for the upper limit in the range 130-200 keV, but for such low values of ϵ, it would not possible to reproduce the INTEGRAL data at lower energies. We then decided to take as reference value $\epsilon = 0.1$, corresponding to a maximum electron energy of $E_{max} \sim 900$ TeV.

[1]This value is achievable in such an extended PWN only if the magnetization parameter is high.

5.2.2 Test case 2

In test case 2 (TC2 hereafter) we assume that an additional source contributes to the VHE emission. This source may in part explain the observed morphology and in part relieve the requirement of a very high IR background needed to reproduce the GeV-TeV spectrum.

There is a clear indication that the VHE emission of MSH 15-52 extends much farther out than the PWN, especially in the SE direction. Tsirou et al. (2018) analyzed the HESS data and modeled the extended emission with a Gaussian component centered SE of the PWN (RA= 228.575000°, DEC=−59.183056°) with a width $\sigma = 6.89'$. The centroid of this component is closer to the centroid of the *Fermi*-LAT data than to the center of the PWN. This Gaussian component accounts for $64.8\% \pm 5.3\%$ of the total flux in the energy band between 280 GeV and 40 TeV.

We thus modified the previous model including an extra electron population that we assume to belong to the Gaussian component and to have an ad-hoc log-parabola spectral distribution:

$$K(E) = k_0 \left(\frac{E}{E_0}\right)^{-\Gamma-\beta \log \frac{E}{E_0}} \tag{5.1}$$

where k_0 is a normalization and Γ and β are the parameters describing the power law curvature. We computed the IC emission from this Gaussian component using the same method adopted for the electron population in the PWN, with the full Klein-Nishina cross-section (Blumenthal & Gould 1970) and the same ISRF.

For the fit with TC2, we fixed all the parameters of the ISRFs at the values inferred from GALPROP. The free parameters are α_2, η_B and the three parameters of the spectrum of the Gaussian component: k_0, Γ and β. Furthermore, we added the constraint that the flux of the Gaussian component is $64.8\% \pm 5.3\%$ of the total flux in the energy range 0.28-40 TeV, as found in the HESS data.

The result of the fitting procedure and the values of all the parameters of the model are reported in Table 5.1. The corresponding MWL spectrum is shown in the lower panel of Figure 5.2. The percentage of the total flux in the Gaussian component from this fit is $\sim 60\%$, in agreement with the constraint that we imposed.

The best-fit value of η_B is very high ($\eta_B = 0.360^{+0.039}_{-0.028}$), even higher than in TC1, resulting in a higher magnetic field (consistent with the values found by other authors). This

is probably a consequence of the condition that we imposed on the flux of the Gaussian component. Conversely, smaller values of η_B would give a higher flux at TeV energies from the PWN, leading to a lower flux from the Gaussian component, not consistent with the constraint that we imposed. For the confinement factor ϵ similar arguments apply as for TC1, with the difference that for TC2 we can use a slightly lower value ($\epsilon = 0.07$). However, the maximum electron energy does not change ($E_{max} \sim 900$ TeV) since it depends also from η_B (equation 4.9).

We have computed the total energy content of the electron population of the Gaussian component in order to understand its possible origin. Integrating over energy the spectrum of this electron population we find a total energy $E_{G.C.} = 2.3 \times 10^{48}$ erg. If the medium is highly-diffusive a high number of particles can escape from the PWN during its lifetime. The value of the diffusion coefficient for Bohm diffusion (equation 4.5) at $t = 1500$ year is $\kappa \sim 10^{26}$ cm^2 s^{-1}. Integrating over time the energy of the particles that escape from the PWN, we found a total energy of $\sim 10^{46}$ erg, not enough to explain the emission from the Gaussian component. However, the escape of particles from the PWN can be different from a simple Bohm diffusion and for example, it can be enhanced at the edges of the nebula (Gelfand 2017) due to Rayleigh-Taylor instabilities (Bucciantini et al. 2004; Porth et al. 2014). If we assume $\kappa \sim 10^{28}$ cm^2 s^{-1} (at 10 TeV), the total energy of the escaped electrons is enough to power the Gaussian component.

Finally, we tested the possibility that the emission of the Gaussian component is produced by a hadronic population of particles. In this case, the total energy of the hadrons would be $E_{G.C.,hadrons} \gtrsim 10^{51}$ erg (assuming that the density of the medium inside the SNR is $n_H \lesssim 1$ cm^{-3}), three orders of magnitude larger than that of a leptonic population of particles, and comparable to the energy of the SN that originated the remnant. Thus, even for a rather high ambient density, the hadronic component would require an unreasonably high shock energy conversion efficiency and we then disfavor this hypothesis.

5.3 Simulations and analysis

With the models constructed in the previous section, we computed the spectra of MSH 15-52 in the energy range between 50 GeV and 180 TeV. They were adopted for simulating CTA data and test the perspectives of observations of MSH 15-52 with CTA-South.

Table 5.1: Fixed and fitted parameters of the two test cases described in the text. Dots mean that the same value is adopted.

	TC1	TC2	Notes
Pulsar and SN parameters (fixed)			
P (ms)	150	...	Livingstone & Kaspi (2011)
$\dot{P}$ (s s^{-1})	1.5×10^{-12}	...	Livingstone & Kaspi (2011)
τ_c (yr)	1585	...	$P/(n-1)\dot{P}$
n	2.839	...	Livingstone & Kaspi (2011)
$L(t)$ (erg/s)	1.8×10^{37}	...	Livingstone & Kaspi (2011)
t_{age} (yr)	1500	...	estimated[a]
τ_0 (yr)	224	...	$[2\tau_c/(n-1)] - t_{age}$
L_0 (erg/s)	1.3×10^{39}	...	equation 4.3
M_{ej} ($M_\odot$)	5	...	estimated[a]
E_{sn} (erg)	3×10^{51}	...	estimated[a]
d (kpc)	4.4	...	Yao et al. (2017)
Environment parameters			
T_{CMB} (K)	2.7	...	Longair (2008)
U_{CMB} (eV/cm^3)	0.25	...	Longair (2008)
T_{FIR} (K)	30	...	Porter et al. (2006)
U_{FIR} (eV/cm^3)	2.2	...	Porter et al. (2006)
T_{NIR} (K)	3650^{+1330}_{-900}	3000	fitted in TC1; fixed in TC2 (Porter et al. 2006)
U_{NIR} (eV/cm^3)	68^{+24}_{-19}	2.2	fitted in TC1; fixed in TC2 (Porter et al. 2006)
Injection parameters			
E_b (TeV)	1.5	...	fixed
α_1	1.7	...	fixed
α_2	$2.262^{+0.009}_{-0.010}$	$2.246^{+0.010}_{-0.010}$	fitted
η_B	$0.194^{+0.022}_{-0.034}$	$0.360^{+0.039}_{-0.028}$	fitted
ϵ	0.10	0.07	fixed
Added Gaussian component (log-parabola)[b]			
E_0 (TeV)	×	1.5	fixed
k_0 (1/TeV)	×	$0.471^{+0.077}_{-0.070} \times 10^{47}$	fitted
Γ	×	$2.692^{+0.266}_{-0.134}$	fixed
β	×	$0.119^{+0.054}_{-0.092}$	fitted
PWN parameters			
R_{pwn} (pc)	5.93 ± 0.01	5.93 ± 0.01	equation C.4
B (μG)	$14.79^{+0.82}_{-1.35}$	$20.16^{+1.06}_{-0.81}$	equation 4.11
E_{max} (TeV)	900	900	equation 4.9
$E_{G.C.}$ (erg)	×	2.3×10^{48}	Total energy in Gaussian component[b]

[a] t_{age}, M_{ej} and E_{SN} fixed in order to obtain a nebula with a radius of ~ 6 pc.

[b] Only for TC2. See text for more details.

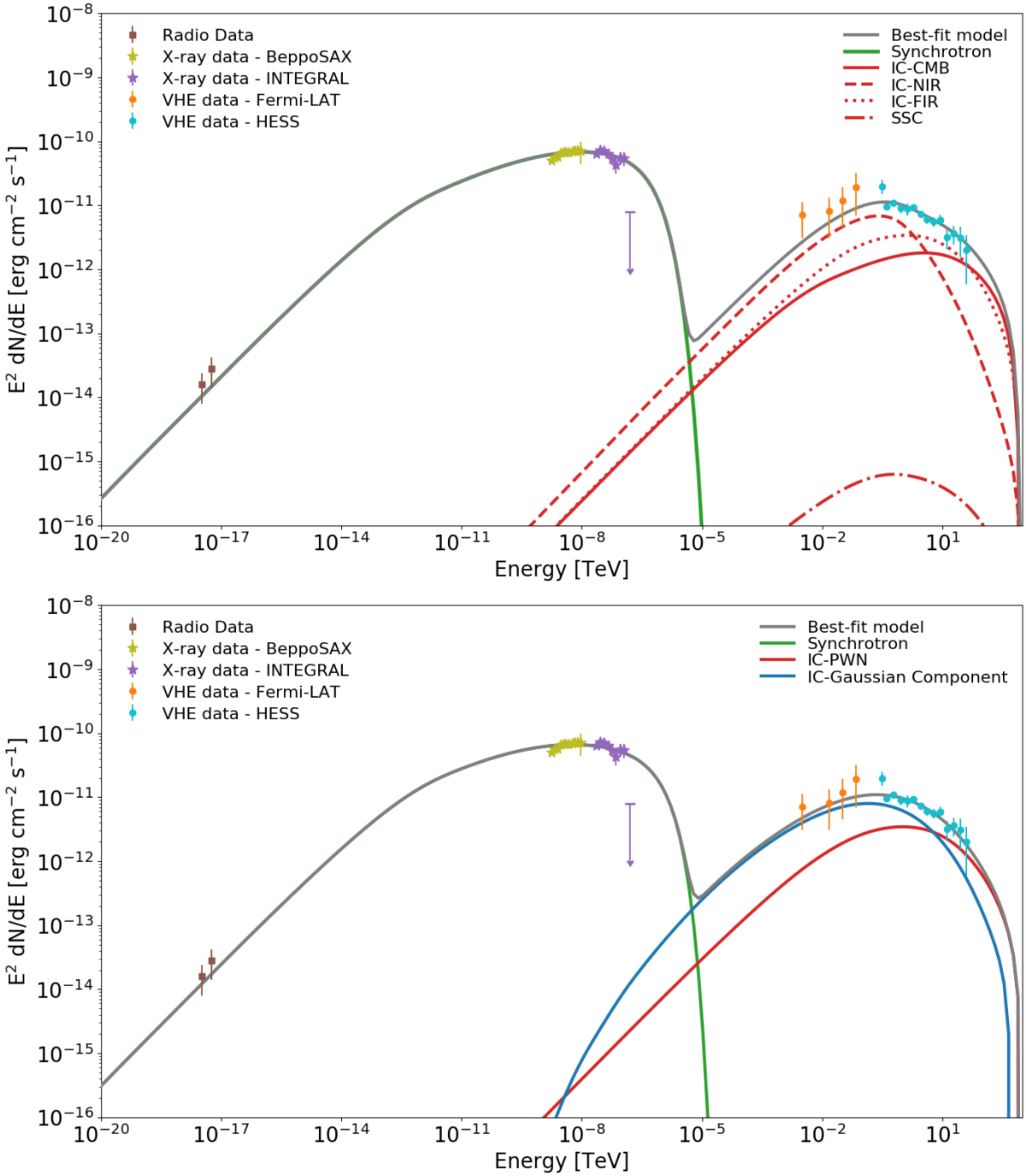

Figure 5.2: Photon SED of TC1 (upper panel) and of TC2 (lower panel) constructed with the parameters in Table 5.1. In the SED for TC2 we only show for clarity the total IC spectra of the PWN (in red) and the Gaussian component (in blue).

We simulated 50 hours of observation with the South array in the energy range 0.05-180 TeV, using the most recent CTA IRFs (*Prod3b-v2*[2]; Bernlöhr et al. 2013). Together with the spatial and the spectral information in the input model we include also the expected cosmic-ray background that will affect the observations. The simulated field has a radius of 0.33°.

All the simulations and analyses have been done using *ctools*-v1.6.1 (Knödlseder et al. 2016). We perform a standard binned likelihood analysis and extracted the TS value as a measurement of the goodness of the fit. At the end, we inspect the residual maps to check if systematic residuals are present.

5.3.1 Test case 1

For the simulations related to TC1, we use the spectral model extracted from the best-fit solution shown in Figure 5.2 (upper panel). For the spatial model, we consider only the emission coming from the PWN, using a *Chandra* X-ray image as a template (Gaensler et al. 2002). From this template, we remove the emission from the central pulsar and the background (estimated from four regions of the image far from the PWN). We then extract the emission region believed to represent the PWN (a region of ~ 5 arcmin around the pulsar position) and renormalize the entire image. In Figure 5.3 we show the final X-ray template image obtained in this way.

For the analysis, we fit the data with three different spatial models: The same X-ray template of the simulation, a radial Gaussian disk, and an elliptical disk. As spectral models we use: A power law, an exponentially cut-off power law (ECPL), a smoothly broken power law (SBPL) and a log-parabola.

The best-fit solution has been obtained with the X-ray template as spatial model and with the SBPL spectral model. However, also the elliptical disk (as spatial model) and the log-parabola (as spectral model) give analogous results. Figure 5.4 shows the spectrum extracted for the X-ray template with the SBPL spectral model and that for the elliptical disk with the log-parabola spectral model. The associated residual maps are also shown in the same Figure. As expected the quality of the data is very good. CTA will give a comprehensive view of the spectrum of MSH 15-52 from the *Fermi*-LAT energy range to

[2] www.cta-observatory.org/science/cta-performance/

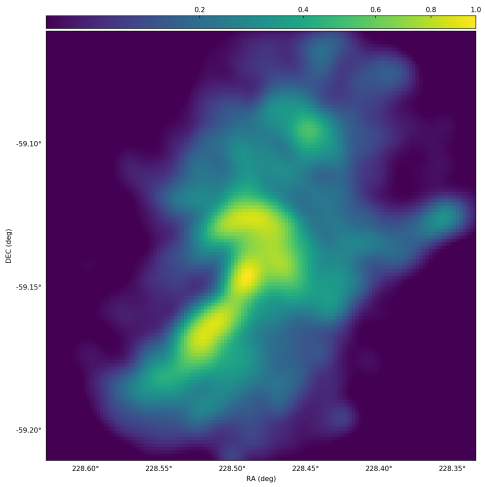

Figure 5.3: X-ray spatial template of the PWN in MSH 15-52 constructed from a *Chandra* image (Gaensler et al. 2002).

the HESS energy range and beyond.

5.3.2 Test case 2

For the simulations related to TC2, we extracted the data from the best fit solution shown in Figure 5.2 (lower panel). For the spatial template of the PWN, we use a *Chandra* X-ray image, as before, while the second region is modeled using a radial Gaussian with the parameters reported by Tsirou et al. (2018).

The spectral models adopted for the analysis are the same as for TC1. For the spatial models, we used two different approaches. We started fitting the data with two different spatial models for the two regions: the X-ray template and one radial Gaussian (the same models adopted for the simulation), 2 radial Gaussians, 2 point source models. We then tried to fit the data using only one, more extended, spatial model, to check if CTA can distinguish the complex morphology of MSH 15-52. In this case, the adopted spatial models are a radial Gaussian model or an elliptical disk model.

The overall best-fit solution is obtained considering the X-ray template (for the PWN) plus a radial Gaussian model (for the external component). For the PWN the best-fit spectral model is a SBPL, while for the Gaussian component it is a log-parabola. In Figure 5.5 we show the resulting VHE spectra for the two regions together with the total composite spectrum of MSH 15-52. The spectra of the two regions are well reconstructed

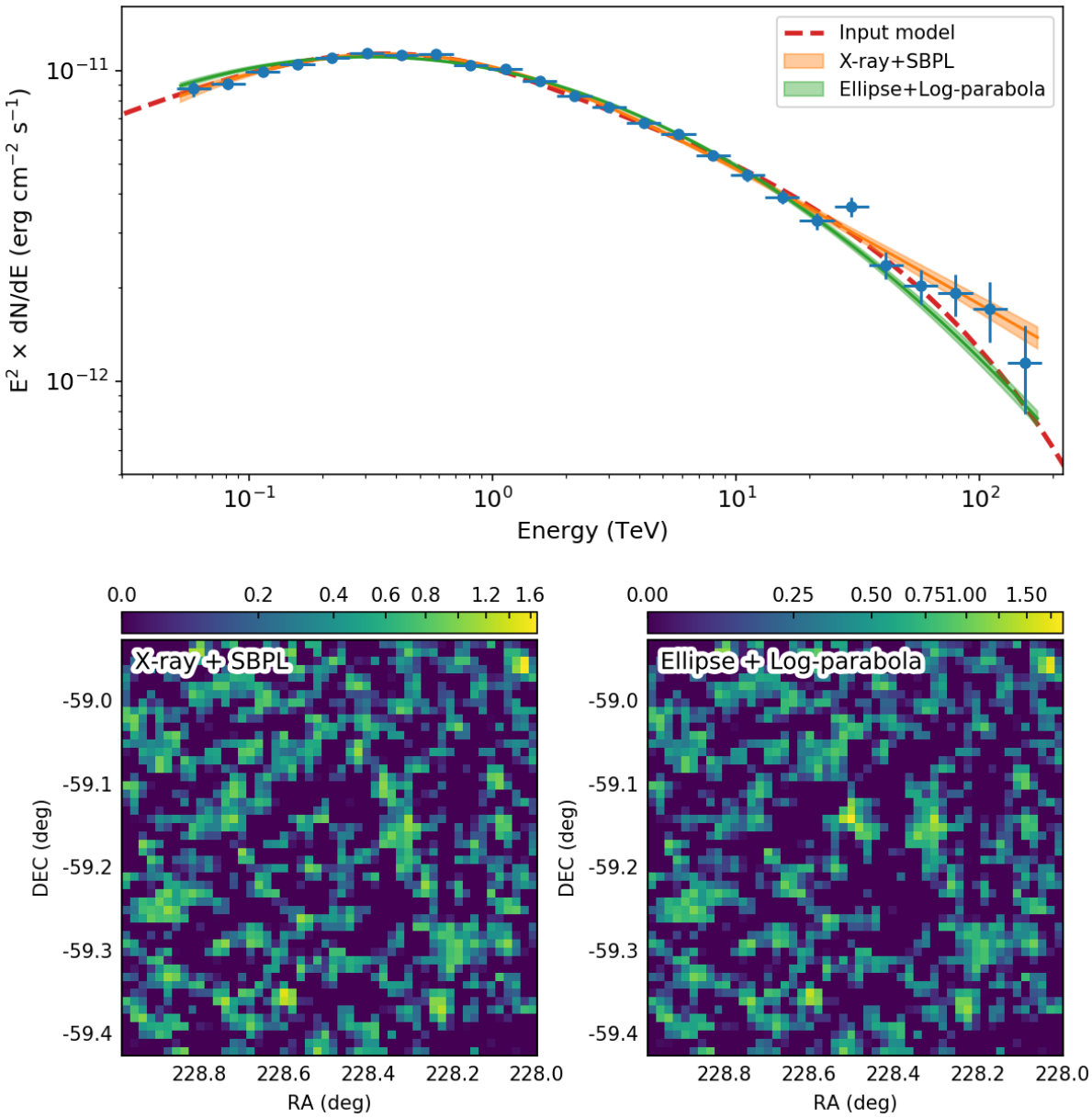

Figure 5.4: Results of the maximum likelihood analysis on the simulated CTA data of TC1 for MSH 15-52 obtained with the X-ray spatial template. In the upper panel, we show the extracted spectral data (blue points) together with the best-fit spectral models (in orange and in green) and the input model (red dashed curve). In the lower panel we show the associated residual maps.

from the analysis chain.

In Figure 5.6 we compare the results of the two different analysis. For the analysis

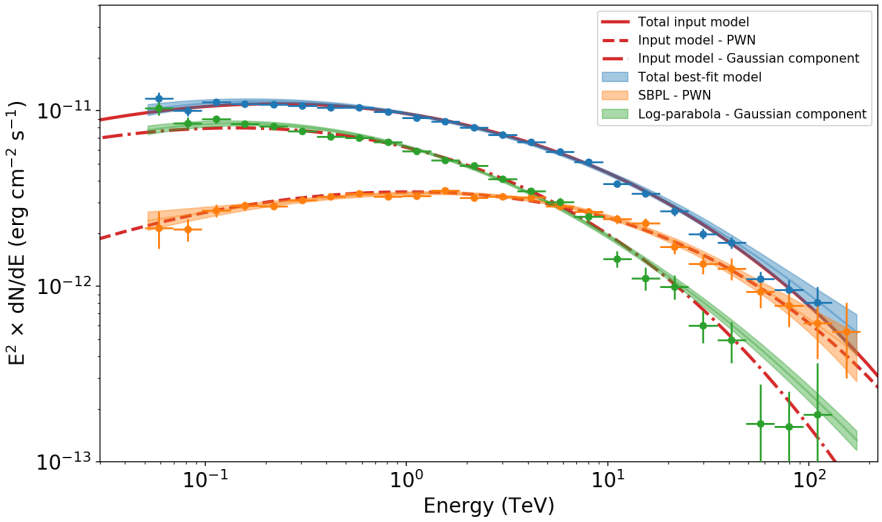

Figure 5.5: Results of the maximum likelihood analysis on the simulated CTA data of TC2 for MSH 15-52 obtained with the X-ray spatial template (for the PWN) plus a radial Gaussian model (for the external component). We show the spectrum (blue), the spectrum of the PWN (orange) and the spectrum of the Gaussian component (green). We also show the corresponding best-fit spectral models (shaded areas) and the input models (red lines).

with a single region, we find that the best-fit is obtained using an elliptical disk with a SBPL spectrum. The VHE spectrum is reproduced but, looking at the residual map, we clearly see that the spatial model is not satisfactory. We conclude that the model with a single spatial region cannot reproduce the data. On the other hand, the model with two spatial components (X-ray template plus Gaussian component) provides a satisfactory description of both the spatial and spectral data (Figure 5.6)

Using the two-components best-fit model of the TC2 simulation we have produced excess maps[3] in different energy bands, subtracting the cosmic-ray background from the data. In Figure 5.7 we show the excess maps in the range 50-200 GeV, 0.2-10 TeV and 10-180 TeV. These energy ranges are chosen to represent the *Fermi*-LAT observations (lower range), the HESS observations (mid range) and the much more extended window achievable with CTA (higher range). In each of these three maps, we fit the images with a two dimensional Gaussian to determine the centroids of the γ-ray emission. In

[3]The best way to visualize the images of sources after the analysis chain. Excess maps are obtained subtracting the estimated background from the best fit solution.
cta.irap.omp.eu/ctools/users/user_manual/iact_analysis/tips.html

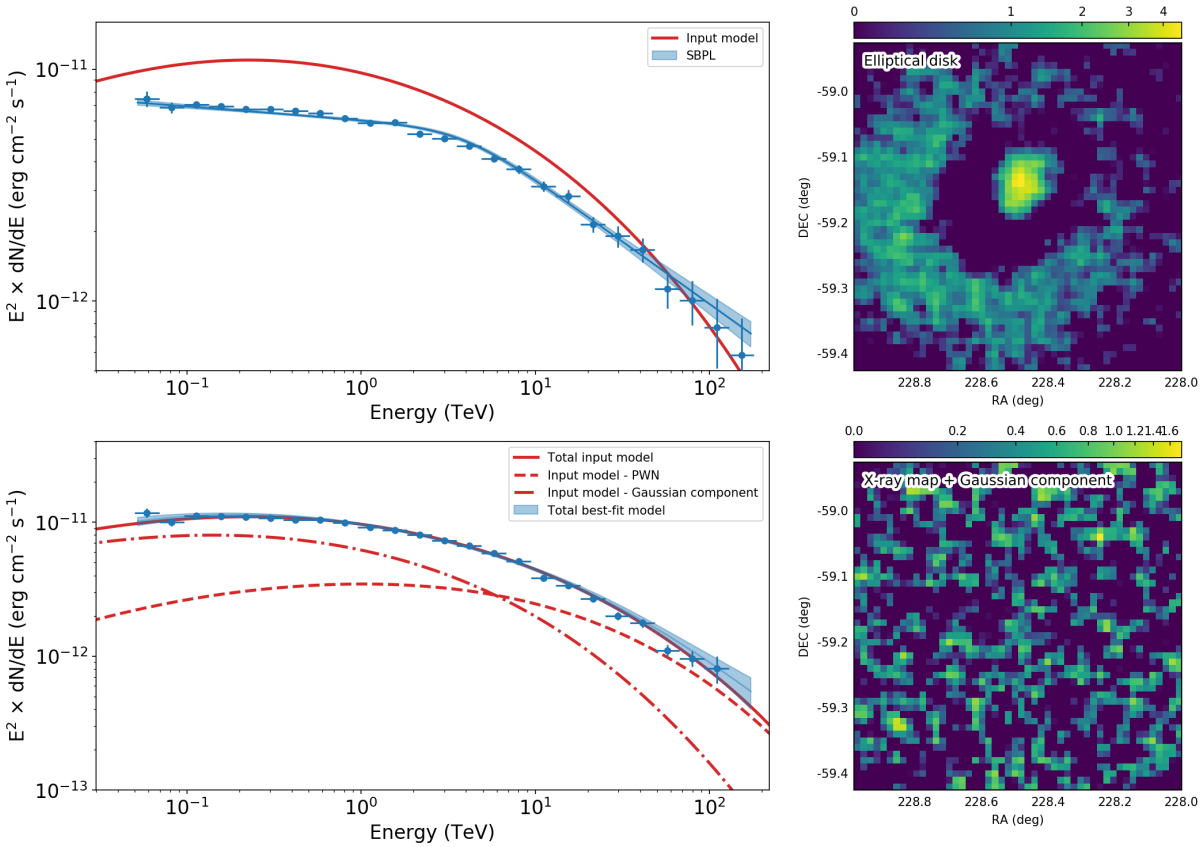

Figure 5.6: Results of the maximum likelihood analysis on the simulated CTA data of TC2 for MSH 15-52 obtained considering only one region (elliptical disk; upper panels) or two regions (X-ray template plus Gaussian component; lower panels). The spectra are shown together with the associated residual maps. The fit with a single spatial model cannot reproduce the data.

this final analysis, we made use of a least-square fitting algorithm applied directly to the excess maps[4] to determine the 'average' positions of the centroids, neglecting the actual morphological complexity of the system. In Figure 5.8 we show these Gaussians superimposed to the excess map in the full energy range. Although the width of this Gaussian profiles resemble the PSF in each energy range, the centroid seems to shift from South to the pulsar position as the energy increases. This analysis aims essentially at showing that it is difficult to interpret data obtained with different instruments and at a lower angular resolution. This is probably the reason why the best-fit position from the *Fermi*-LAT data (Figure 5.1) is shifted from the center of the PWN and of the Gaussian component. This means that in order to understand well the geometry of the system and to avoid systematic errors arising from the analysis of the data coming from different facilities, we need an instrument that can cover a very extended energy range, like CTA.

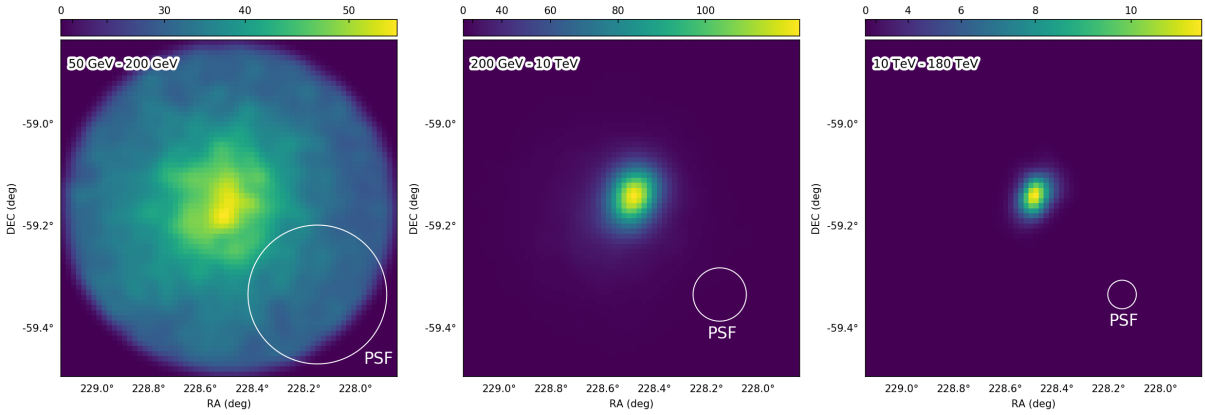

Figure 5.7: Excess maps of TC2 in different energy bands together with the corresponding average PSF.

5.4 Conclusions

In this chapter we have studied MSH 15-52, a young PWN with a complex morphology, assessing the capabilities of CTA in observing this source.

We first constructed a model (TC1) assuming that the γ-ray emission comes only from the central PWN. The analysis of this simulation shows that CTA can observe this

[4]This is a more approximate approach compared to the maximum likelihood analysis applied to the two regions, but it is adequate for what is discussed here.

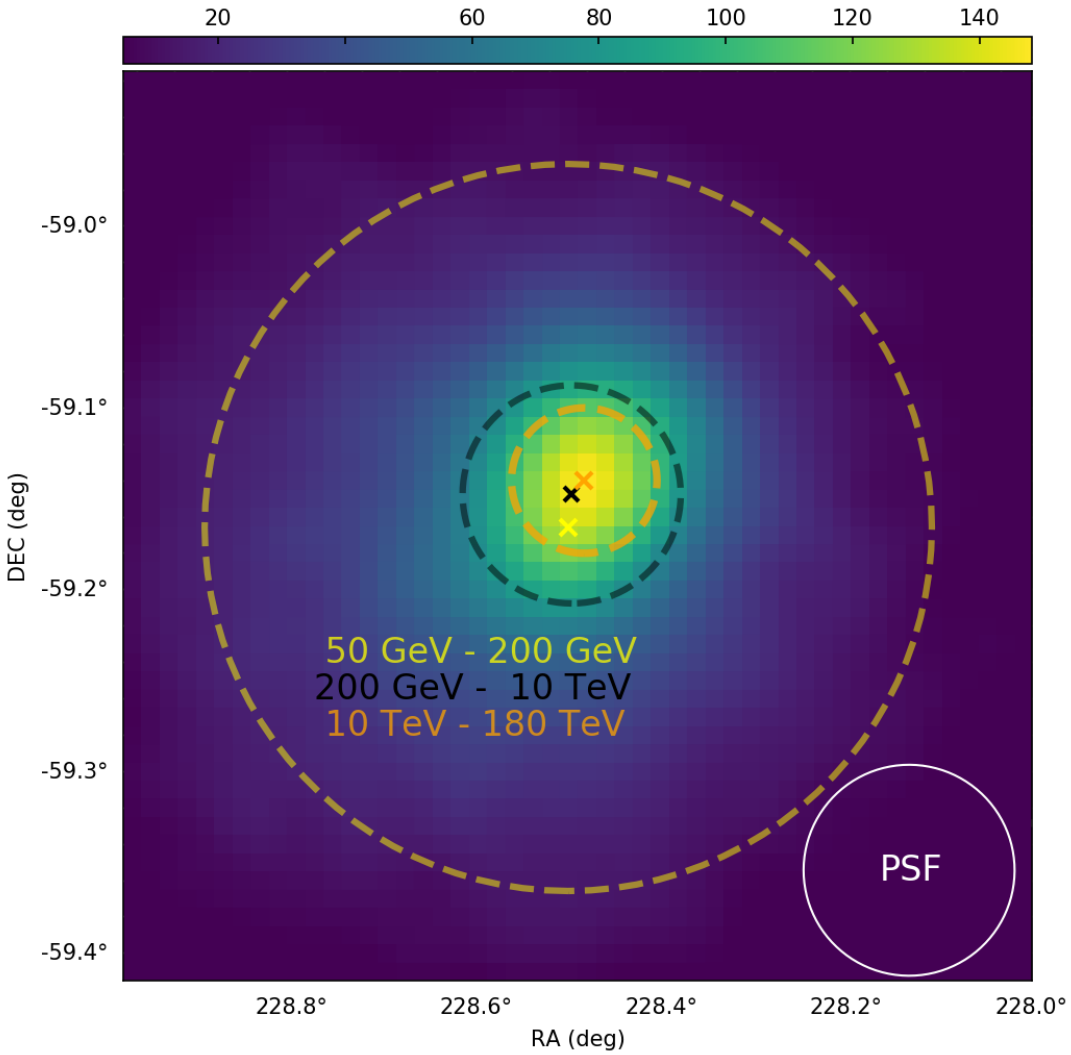

Figure 5.8: Excess map of TC2 in the full simulated energy range. The dashed circle indicates the widths of three Gaussian profiles obtained after performing a least-square fit to the images in different energy ranges: 50-200 GeV (yellow), 0.2-10 TeV (black), 10-180 TeV (orange). The centroid of each Gaussian seems to shift from South to North as the energy increases. See the text for more details.

source from the *Fermi*-LAT energy band to the HESS energy band and beyond. However, we found that, in order to explain the observed IC peak, we need a high NIR background.

We considered another model for the source (TC2) following the work by Tsirou et al. (2018). We assumed that the morphology of the source in the γ-rays is the superposition of two contributions, modeled using a *Chandra* X-ray map (above 4 keV) and a Gaussian component South-East from the position of the pulsar[5]. With the addition of this Gaussian component we found that a high NIR background is no longer needed to reproduce the simulated data. From the simulations we found that CTA could clearly disentangle the two regions, measuring the spectra emitted by them in great detail. This is crucial in order to understand the processes that power the external Gaussian component. The total energetics of the particles in the Gaussian component is comparable to the energy of the particles that escape from the PWN during its entire lifetime, if we take a diffusion coefficient of the order of $\kappa \sim 10^{28}$ cm^2 s^{-1} (at 10 TeV).

Finally, from the analysis of the simulated TC2 data, we find some evidence of an energy-dependent morphology, likely arising from the particles escaping from the PWN and injected inside the Gaussian component. Observations made with CTA could measure the extension of this component at different energies and give important information on the diffusion of particles inside and outside the PWN. However, to better understand the spatial properties of MSH 15-52, we need more advanced multidimensional models that can better reproduce the morphology of the system.

[5]We point out that, at variance with Tsirou et al. (2018), we did not consider the dependence of the X-ray map on the distance from the pulsar, since the one-zone time-dependent leptonic model works only with a constant magnetic field inside the nebula.

Chapter 6

The ASTRI/CTA Data Challange (ACDC)

6.1 Introduction

The ASTRI/CTA Data Challenge (ACDC) is a project aiming at the production of a set of simulated data for the ASTRI Mini-array. It was funded by INAF, to test the readiness of the scientific community to take advantage of the ASTRI Mini-array data and to enhance its future scientific return.

The importance of carrying out a data challenge well before the start of a large scale observational project was demonstrated by the *Fermi*-LAT collaboration. Thanks to the data challenges they were ready to produce scientific results already a few weeks after the beginning of the actual observations. Similarly, the CTA collaboration has already performed a first data challenge (CTA-1DC) to test all pipelines and reduction/analysis chain and to probe the real potential of CTA. The INAF scientific community decided to follow the example of the *Fermi*-LAT and the CTA collaborations with the ACDC project.

The purpose of this project is to:

- Provide a test of the instrument data chain robustness and test each step of the analysis chain. The simulations of the data start directly from the photons emitted from the astrophysical sources and proceeds step-by-step with the propagation and

the interaction of these photons with the atmosphere. The photons of a particular source are detected with the simulated array, and then enter in the analysis pipeline which reconstructs the γ-ray sky. The source properties measured from the simulations are compared with the injected ones. A variety of different sources are simulated to test both the instrument response functions and the reliability of the data analysis pipeline.

- Train the Italian astrophysical community in the analysis of the ASTRI Mini-array TeV data with regards to format, size, content, and details of analysis issues. This will help to grow the science analysis team and to provide a feedback for the software development teams on what works and what is instead missing from the data formats and tools. The simulated data will be delivered to the community of potential INAF users who will have the opportunity to learn the analysis techniques used in VHE γ-ray astronomy.

- Test the capabilities of the final array and give the opportunity to investigate scientifically relevant questions that will then be studied with the ASTRI Mini-array. This is crucial to understand how to fully take advantage of the array, selecting the most promising and scientifically relevant sources. The input sky models also contain sources with no obvious counterparts to allow for the preparation of the identification strategy. This, again, is very important since a series of serendipitous sources are expected to be discovered and a strategy for conducting coordinate MWL campaigns has to be devised.

Starting from the state-of-the-art knowledge of the VHE astrophysical sources and models predictions of the TeV sky, a realistic three-year observing program was simulated. The simulated data are comparable to the data expected to be collected with the ASTRI mini-array, so that a comparable effort for the analysis is required. This TeV sky model is extrapolated in the ASTRI energy range, starting from data collected with the current generation of γ-ray telescopes and considering also theoretical models proposed for the various sources.

The production of the TeV sky started by issuing an internal "Call for Proposal" to select the most interesting objects. From these proposals, a realistic pointing plan was developed taking into account all the aspects related to the organization of the observations, and obtaining reliable data products.

In this project, I was actively involved in the production of the sky model proposing to observe SNR G0.9+0.1 and MSH 15-52, and producing models to simulate these sources. I have been involved also in the scientific analysis of the simulated data, trying to extract the best possible results and to spot the issues arising in the analysis chain.

6.2 Project organization

The project is structured in workpackages (WPs). The structure is shown in Figure 6.1. In the following, I will briefly summarize the mean tasks of the various WPs (Pintore & The ASTRI Collaboration in prep.).

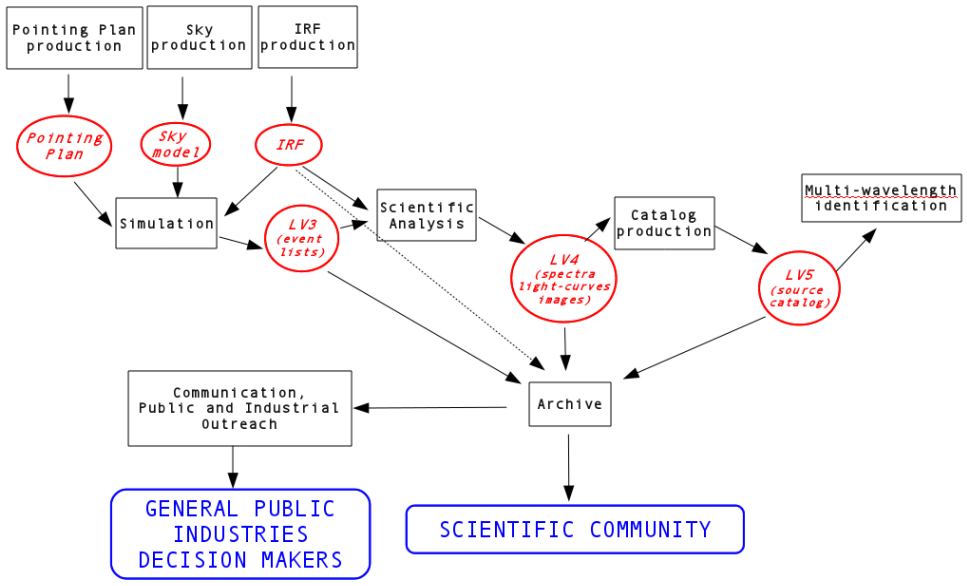

Figure 6.1: Structure of the ACDC project. The (black) boxes indicate the WPs, the (red) circles the data products and the (blue) boxes at the bottom the output for the community (Pintore & The ASTRI Collaboration in prep.).

Pointing Plan Production (PP) WP: Production of an optimized pointing plan for the ASTRI Mini-array observations, including their duration. The Pointing Plan will take into account all the requested targets accounting for their visibility constraints, based on the ASTRI Mini-array site, and the windows of useful observing time not disturbed by Moonlight.

Sky production (SKY) WP: Production of a realistic TeV sky model. Starting from the requested targets and the field covered by the observation, all the known sources at TeV energies are added. Moreover, some serendipitous sources are included. All the proposed targets, known and serendipitous sources, are described by their spatial information (spatial extension and morphology), their TeV spectral shape and their temporal variability. Finally, the sky model includes a model of the CR background and the diffuse emission from the Galactic plane.

Instrument Response Function production (IRF) WP: Creation of the instrument response files to be used in the data challenge. These files contain the information on the effective area of the array, the energy resolution, the Point Spread Function (PSF), and the expected CR background. These values depend on both the energy range and the off-axis angle. The IRFs are computed starting from the *sim_telarray* code (Bernlöhr 2008), which allows to do Monte Carlo simulations of γ-ray events, needed for the estimation of the response of the array.

Simulation (SIM) WP: Production of realistic data events files and auxiliary files in the specific format required (level 3 data). The simulated data are based on the pointing plan, TeV sky model and IRFs developed from the other WPs. The software adopted is the standard simulator developed for the CTA data, *ctobssim* (Knödlseder et al. 2016).

Scientific Analysis (SA) WP: Production of scientific data consisting of sky maps, spectra, and light curves (level 4 data). The starting point is the simulated event lists from the SIM WP. All the analysis is performed with *ctools* (Knödlseder et al. 2016) and *gammapy* (Donath et al. 2015; Deil et al. 2017). The results are eventually compared to the simulated source models to check the robustness of the data production and analysis chains.

Catalog Production (CAT) WP: Creation of a catalog of the simulated sources containing the measured properties of the sources detected above a certain threshold of significance (level 5 data). The catalog includes also the possible source association for the unidentified sources.

Multiwavelength identification (MWL) WP: Development of a multiwavelength association strategy to address the identification of unknown sources (or known sources with no viable associations).

Archive (ARC) WP: Implementation of a data archive that will contain the simulated

data, the analyzed data and the catalog data with all the corresponding response files.

Communication, Public and Industrial Outreach (CO) WP: Enhancing the visibility of the CTA and the ASTRI projects to the scientific community as well as to the general public. As part of this activity a website is being built[1] and meetings with the general public were organized.

6.3 Call for proposal

The three-year observing programs started from a "Call for proposal" extended to all the ASTRI collaboration. The final output of this call resulted in the request to observe 20 astrophysical sources. These targets were divided into 19 different fields, for a total of 4350 hours of observing time (Pintore & The ASTRI Collaboration in prep.). Table 6.1 reports all the simulated fields, with the related proposed sources.

The period selected for the three-year simulated observing campaign goes from January 1, 2020 to January 1, 2023 and takes into account the visibility constraints and moon conditions (ASTRI Mini-array located at Paranal, Chile). The overall available time corresponds to $\sim$ 5160 hours, of which 4350 are devoted to pointed on-source observations. The remaining $\sim$ 800 hours are devoted to simulated observations of sky fields without any TeV source (needed for the classical ON-OFF analysis). All the observation blocks last 20 minutes and are randomly distributed within 1° around the main target (even in the case of the sky fields without TeV sources). A traditional wobbling observing mode is not suitable in the case of our observations characterized by a large field of view containing several targets (Pintore & The ASTRI Collaboration in prep.).

The diffuse emission from the Galactic plane has been included in the simulations and has been modeled in the same way as in the 1DC of CTA, based on predictions from codes that solve the CR transport equations and calculate the related multiwavelength emission (Gaggero et al. 2015; Werner et al. 2015).

All the known sources expected at TeV energies that were found in the FoV of the different fields have been inserted in the sky models (considering that the array has a good

[1] www.acdc.inaf.it/home

Table 6.1: Simulated sky fields for the ACDC project, according to the proposal requests and the pointing plan restrictions (Pintore & The ASTRI Collaboration in prep.).

Field	RA (deg)	DEC (deg)	Exposure (hr)	Main sources	Type
01+02	276.6300	-13.0900	300	LS 5039	Binary
				HESS J1825-137	PWN
03	40.6700	-0.0133	200	NGC 1068	AGN
04	15.0392	-33.7089	100	Sculptor	Dwarf spheroidal galaxy
05	53.9254	-54.0492	100	Reticulum II	Dwarf spheroidal galaxy
06	342.9796	-58.5689	100	Tucana II	Dwarf spheroidal galaxy
07	237.2500	-30.7500	300	Te-REX 1549	AGN
08	266.9225	-26.4650	300	Terzan 5	Globular cluster
				SNR G0.9+0.1	PWN
09	195.7517	-63.1986	300	HESS J1303-631	PWN
10	84.0000	-67.5864	200	LMC P3	Binary
11	248.2500	-47.5500	150	HESS J1632-478	PWN
				HESS J1634-472	Unidentify
12	269.7150	-24.0519	300	SNR W28	SNR
				Terzan 5	Globular cluster
13	155.9921	-57.7636	200	Westerlund 2	Star cluster
14	128.7500	-45.6000	100	Vela X	PSR and PWN
15	266.8467	-28.1517	100	SNR G0.9+0.1	PWN
				Terzan 5	Globular cluster
16	228.5292	-59.1575	200	MSH 15-52	PWN
17	278.3900	-10.5689	300	HESS J1833-105	PSR and PWN
				HESS J1825-137	PWN
				LS 5039	Binary
18	83.6333	22.0144	100	Crab	PSR and PWN
19	329.7196	-30.2217	200	PKS 2155-304	AGN

sensitivity up to $\sim 4^{\circ}$). The sources have been taken from the HESS catalog[2] and the *Fermi*-LAT Third Source Catalog (3FGL; Acero et al. 2015). Moreover, 8 serendipitous sources were also inserted in the sky model. A total of 81 sources in ~ 1250 square degrees of the sky were finally simulated (Pintore & The ASTRI Collaboration in prep.).

My contribution to this project is related to the production of models for the two sources studied in this thesis: SNR G0.9+0.1 and MSH 15-52. As already mentioned, PWNe are a class of sources very bright at TeV energies and therefore are a natural target for the ASTRI Mini-array. 8 out of 20 targets requested in the ACDC proposals are PWNe.

SNR G0.9+0.1 is a difficult target for the ASTRI Mini-array (the flux at TeV energies is only $\sim 2\%$ of the Crab flux). However, it is an interesting target to check the sensitivity in the higher energy range and to see if it is possible to measure a cut-off at energies $\gtrsim 20$ TeV. In order to test it, we selected a point source spatial model (the extension of the PWNe is well below the resolving capabilities of the array) and a PLEC spectral model with the normalization N_0 and spectral slope Γ reported in Table 3.1, and a cut-off at 30 TeV. This energy cut-off is in agreement with the predictions from the modeling performed in section 4.3, where we found that a cut-off around 20/30 TeV is expected. The estimated observing time for this measurement is 400 hours since the source flux is only $\sim 2\%$ of the Crab flux. This observing time is achievable because the source is in the direction of the Galactic Center and there are many other interesting potential targets nearby. In fact, another proposed source is at about $\sim 3^{\circ}$, Terzan 5, enabling the simultaneous observation of both sources with a single pointing.

MSH 15-52 can be used as a test for checking the resolving capabilities of the ASTRI Mini-array. As shown in Figure 5.1 and in Chapter 5 the morphology of the system at VHE does not simply follow the X-ray morphology and does not have a regular shape (such as a radial disk, a radial Gaussian profile, etc...). To reproduce the shape observed with HESS it is possible to use three radial Gaussians with different sizes and different fluxes. This spatial model for MSH 15-52 is an approximate phenomenological representation of the system without a physical motivation (at variance with what has been done in the dedicated study of this source in Chapter 5) but it is useful for the purpose of this work. The three regions are shown in Figure 6.2, and the coordinates and corresponding fluxes

[2] www.mpi-hd.mpg.de/hfm/HESS/pages/home/sources/

are reported in Table 6.2. The overall spectrum of the source is taken from Aharonian et al. (2005a), a power law with normalization $N_0 = 5.7 \times 10^{-12}\text{TeV}^{-1}\text{cm}^{-2}\text{s}^{-1}$ and index $\Gamma = 2.27$. The three regions have the same spectral index and emit $\sim 44\%$, $\sim 23\%$ and $\sim 33\%$ of the total flux. The time needed to disentangle the three sources has been estimated in 200 hours.

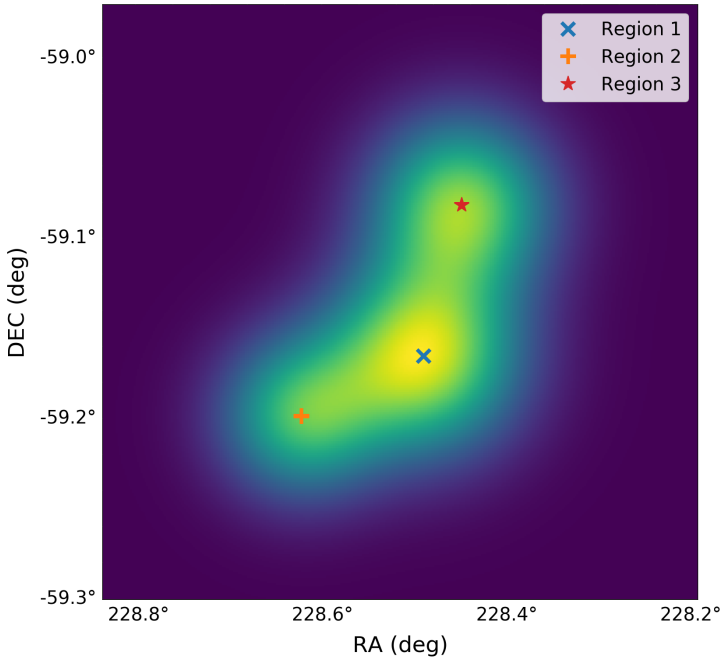

Figure 6.2: Phenomenological model for MSH 15-52 used in the ACDC simulations. The source is composed by three radial Gaussian profiles with the parameters reported in Table 6.2.

Table 6.2: Spatial and spectral parameters for the simulations of MSH 15-52, modeled with three radial Gaussian spatial profiles and pure power law spectra.

Region	RA (deg)	DEC (deg)	σ (arcmin)	N_0 ($\text{TeV}^{-1}\text{cm}^{-2}\text{s}^{-1}$)	Γ
01	228.4901125	-59.1660667	1.2	2.5×10^{-12}	2.27
02	228.6227188	-59.1991324	0.3	1.3×10^{-12}	2.27
03	228.4493583	-59.0823381	0.9	1.9×10^{-12}	2.27

The simulations of the data have been done using the task *ctobssim* of the software package *ctools* (Knödlseder et al. 2016), in the energy range 1-100 TeV and with the latest ASTRI Mini-array IRF (called *Astri_June_50h*).

6.4 Data analysis

The analysis of the simulated data was performed using a binned and an unbinned maximum likelihood procedure.

The final choice for the analysis chain has been done after performing a series of tests needed to optimize the results (comparing the input parameters from the simulations with the output parameters) and to minimize the computing time. Here we report the analysis chain for the two sources for the binned analysis:

- Restrict the energy range to 2.5-80 TeV. This was needed to avoid artifacts appearing in the lower and higher energy bins and that were affecting the fitting procedure. The interpretation of this effect is not straightforward but is believed to arise in the binned analysis when the fluxes are calculated in energy bins near the boundaries of validity of the IRF. This issue has been reported to the IRF WP and the developer of the analysis software.
- Bin the events files in energy with 20 logarithmic bins.
- Select all the events in a square region with a side length of 2° around the source and bin them with a pixel size of 0.01° (map with 200×200 pixels).
- Compute the PSF cubes, exposure cubes and the background cubes with the same parameters as the events files (except for the pixel size of the PSF cube that was fixed at 0.1°, since it varies slowly in the FoV). This step is recommended to pre-compute the instrument response needed for the likelihood analysis.
- Extract the source properties with the maximum likelihood analysis on the binned cubes. A series of parameters are needed to calculate the input models (for the spatial and spectral properties of the source and the background), that can be fixed or left free.
- Extract 10 spectral points and compute the butterfly plot from the best-fit solution of the likelihood analysis.
- Compute the so-called residual map of the best-fit solution. From the results of the likelihood analysis, the best-fit model is subtracted from the simulated events and

the difference is used to build a map of the residuals of the region. If the fitted model reproduces well the simulation, the residual map is uniform.

In the case of the unbinned analysis the procedure is reported below:

- Select the full energy range (1-100 TeV) since there is no problem with the energy binning.
- Extract a region with a radius of 1° around the source position.
- Extract the source properties with the unbinned maximum likelihood analysis applied directly to the events data file.
- Extract 10 spectral points and compute the butterfly plot from the best-fit solution of the likelihood analysis.
- Compute the residual map of the best-fit solution.

For the analysis of SNR G0.9+0.1, the simulated data have been fitted either with a pure power law or with a PLEC with a cut-off energy free to vary to check if the detection of the cut-off is statistically significant. For the spatial model we used either a point source, a radial disk, or a radial Gaussian profile.

For MSH 15-52, after several tests needed to understand the best way to model the three regions, we choose to perform the analysis with two different approaches. In the first case the source is modeled as it was simulated, fixing the positions and the sizes of the three radial Gaussian profiles. In the second case, the source is modeled using a radial Gaussian profile for the sum of regions 1 and 2, and a point source for region 3, with all the spatial parameters left free to vary to allow the program to adjust them. The spectral models are power laws for all components.

6.5 Results and conclusions

The results of the analysis of the simulated data of SNR G0.9+0.1 are shown in Figure 6.3, together with the differential sensitivity of the array for 500 hours. The results, in this case, are obtained with the unbinned analysis, since we need the full energy range to better

determine the spectrum. The best fit solution is obtained with a PLEC with spectral cut-off at the energy $E_{cut} = 35 \pm 18$ TeV (TS= 624). However, also the model with a pure power law has good significance, although lower than that obtained for the PLEC (TS= 617) and with parameters not compatible with the ones used for the simulation (N_0 and Γ are not consistent). The high background around this source, both the CR background and the Galactic diffuse emission (that is high near the Galactic center), decrease somewhat the accuracy of the measurement of the cut-off energy and the statistical significance of the PLEC model. The sensitivity and the resolving capabilities of the array do not permit to disentangle completely the source from its background at higher energies, even increasing the observing time. Nevertheless, this simulation shows that the ASTRI Mini-array can be used to detect very faint sources, with the performance expected to increase in regions where the Galactic diffuse emission is less intense.

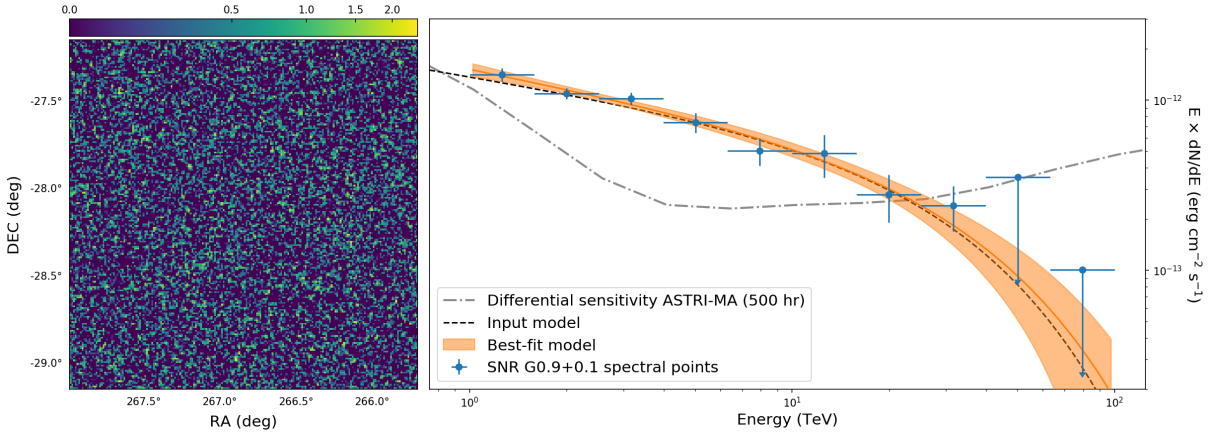

Figure 6.3: Best-fit solution for the analysis of the simulated data of SNR G0.9+0.1 with the ASTRI Mini-array. Left: residual map after the subtraction of the best-fit model. Right: Spectrum compared to the input model (dashed black line) and the differential sensitivity of the array for 500 hours (dashed-dotted gray line).

For MSH 15-52, the two analyses performed return reasonable results using the binned analysis in the energy range 2.5-80 TeV[3]. When fitting the simulated data with the three radial Gaussian profiles, it is possible to recover the input spectra within the errors. The same results can be obtained with three point sources (i.e. three radial Gaussian with very small values of σ) at the center of the three regions. This means that the ASTRI Mini-array will see the three regions as point-like, as expected, but also that it can disentangle

[3]The use of the full energy range was not needed in this case, and therefore the binned analysis was eventually chosen to save computational time.

the emission coming from sources that are very close to each other. Modelling with a single component the composite emission from regions 1 and 2, we found that it is possible to recover the input spectra without fixing the spatial parameters. Therefore, when studying a situation like this, some assumption on the morphology is required to resolve the various components (as often done in the studies of TeV sources), e.g. comparing the TeV morphology with that in the X-ray or radio band. In Figures 6.4 and 6.5 we show the spectra obtained in the two different analyses.

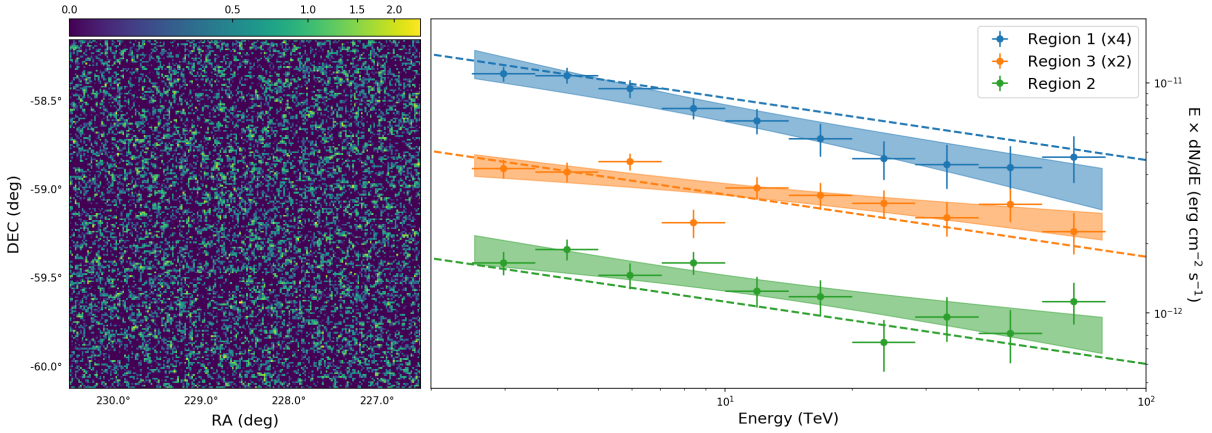

Figure 6.4: Best-fit solution for the analysis of the simulated data of MSH 15-52 with the ASTRI Mini-array in the case of three Gaussian profiles with fixed parameters. Left: residual map after the subtraction of the best-fit model. Right: Spectra compared to the input models (dashed lines).

6.6 PWNe in the Northern hemisphere

In the work presented in this Chapter, the simulated sources were chosen considering the original location for the ASTRI Mini-array at Paranal (Chile), that is in the Southern hemisphere. We now know that the instrument will be installed at Observatorio del Teide (Canary Islands, Spain), in the Northern hemisphere. This does not make the preparatory simulations performed so far useless since the scope of the ACDC project was mainly to test the array and understanding how it works. However, it is interesting at this point to shortly discuss what are the prospects for the study of PWNe from the new Northern site.

In Table 6.3 we show all the known and candidate PWNe at TeV energies that can be

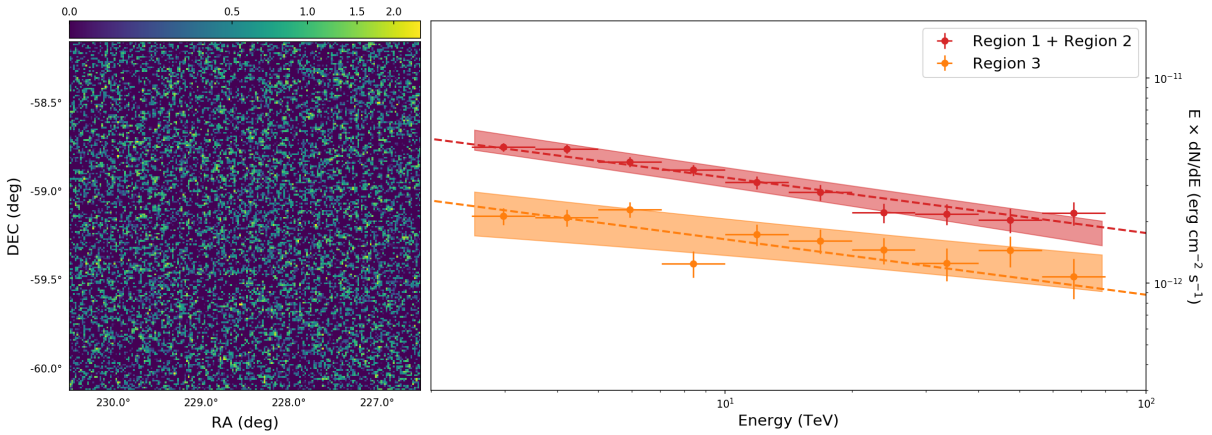

Figure 6.5: Best-fit solution for the analysis of the simulated data of MSH 15-52 with the ASTRI Mini-array in the case of one radial Gaussian profile for regions 1 and 2 and a point source for region 1. Left: residual map after the subtraction of the best-fit model. Right: Spectra compared to the input models (dashed lines).

seen from the North. The sources information are taken from TeVCat (Wakely & Horan 2008) or from the literature. For some sources, the distance was estimated using the distance of the associated pulsar reported from the ATNF pulsar catalogue (Manchester et al. 2005). Some of the PWNe are indicated with an asterisk (PWN*) and correspond to PWNe not firmly confirmed, because of the lack of detection either of PWN emission at lower energies or of the central engine (the pulsar). Also shown are two sources that are defined as "TeV Halos". These sources are a new class of very extended and evolved PWNe, much more extended than what is expected for ordinary PWNe (Linden et al. 2017a; Sudoh et al. 2019; Giacinti et al. 2019).

An interesting fact is that, while the total number of PWNe at TeV energies for the whole sky is ~ 40, those observable from the Canary Islands are 21. It will be possible also to observe the Galactic Center for about 200 hours per year but at very large zenith angles ($\sim 50° - 60°$). In this respect, the extreme case is SNR G0.9+0.1, while for all the other targets in Table 6.3 the situation is better.

What are the best-suited targets for the ASTRI Mini-array? This is a question that can be answered only making a detailed study of the sources and having the correct IRFs. However, it is possible to make reasonable predictions from what was found within the framework of the ACDC project. For example, on the basis of their VHE flux, some sources can be expected to be quite difficult to study, like 3C 58 (0.65% of the Crab flux)

Table 6.3: List of TeV known PWNe and candidate PWNe (PWN*) observable from the Observatorio del Teide (Canary Islands, Spain). The sources are taken from TeVCat (Wakely & Horan 2008).

Name	RA (deg)	Dec (deg)	Type	Dist. (kpc)	Flux (Crab %)	Age (ky)
CTA 1	1.650000	72.780000	PWN*	1.40	4.00%	$5.0 - 20.0$
3C 58	31.404300	64.828300	PWN	2.00	0.65%	> 2.0
Crab Nebula	83.633083	22.014500	PWN	2.00	100.00%	> 1.0
0FGL J0631.8+1034	97.864037	10.618231	PWN*	6.55	29.00%	> 20.0
Geminga	98.475638	17.770253	TeV Halo	0.25	23.00%	> 20.0
SNR G0.9+0.1	266.820000	-28.150000	PWN	8.50	2.00%	$2.0 - 3.0$
HESS J1813-178	273.362900	-17.848900	PWN	4.70	6.00%	$1.0 - 2.0$
HESS J1825-137	276.554410	-13.580040	PWN/TeV Halo[1]	3.90	54.00%	> 20.0
HESS J1831-098	277.850000	-9.900000	PWN*	4.30	4.00%	> 20.0
SNR G21.5-00.9	278.390050	-10.568803	PWN	4.80	2.00%	~ 1.0
HESS J1837-069	279.513040	-6.925940	PWN	6.60	53.00%	> 20.0
Kes75	281.606200	-2.987200	PWN	6.30	2.00%	~ 1.0
IGR J18490-0000	282.257630	-0.021970	PWN	7.00	1.50%	> 20.0
HESS J1857+026	284.295800	2.666700	PWN*	9.00	16.00%	> 20.0
SNR G054.1+00.3	292.629000	18.867000	PWN	4.90	2.50%	$2.0 - 5.0$
DA 495	298.057080	29.418890	PWN	1.00	10.00%	~ 20.0
0FGL J1958.1+2848	299.667092	28.765025	PWN*	1.95	21.00%	> 20.0
MGRO J2019+37	305.020000	36.720000	PWN	5.50	67.00%	> 10.0
0FGL J2021.5+4026	305.377067	40.448211	PWN*	2.15	22.00%	> 20.0
TeV J2032+4130	308.020000	41.570000	PWN/BIN	1.80	3.00%	> 20.0
Boomerang	337.250000	61.200000	PWN	0.80	44.00%	~ 10.0

[1] The interpretation of HESS J1825-137 as a TeV Halo is discussed in Sudoh et al. (2019) and Aharonian (2004, 2013)

or IGR J18490-0000 (1.5% of the Crab flux). Other sources are at the limit but could possibly be observed since the Galactic background gives a negligible contribution (e.g. SNR G21.5-00.9, Kes75, and SNR G054.1+00.3). Probably the class of the TeV Halos comprises the object of major interest for an array with the characteristic of the ASTRI Mini-array since the very big FoV and the uniform sensitivity and PSF along the focal plane will permit to study very extended objects.

Other interesting objects are the candidate PWNe. For example, HESS J1831-098 is a candidate PWN since it is spatially coincident with a pulsar (PSR J1831-0952) that has an energetics high enough to power a PWN, but it has not been detected at other wavelength (Sheidaei 2011). More recently, a TeV halo scenario has been proposed also for this source (Linden et al. 2017b). 0FGL J0631.8+1034, 0FGL J1958.1+2848 and 0FGL J2021.5+4026 have been detected with MILAGRO (The Milagro Collaboration 2001) at TeV energies (Abdo et al. 2009) but not with other Cherenkov telescopes, like MAGIC (Aleksić et al. 2010; Fernandez-Barral et al. 2017). A study of these sources, with an instrument optimized for the $\sim$ 10 TeV energy range and a much better angular resolution than the water Cherenkov telescopes, will be crucial to understand their real nature.

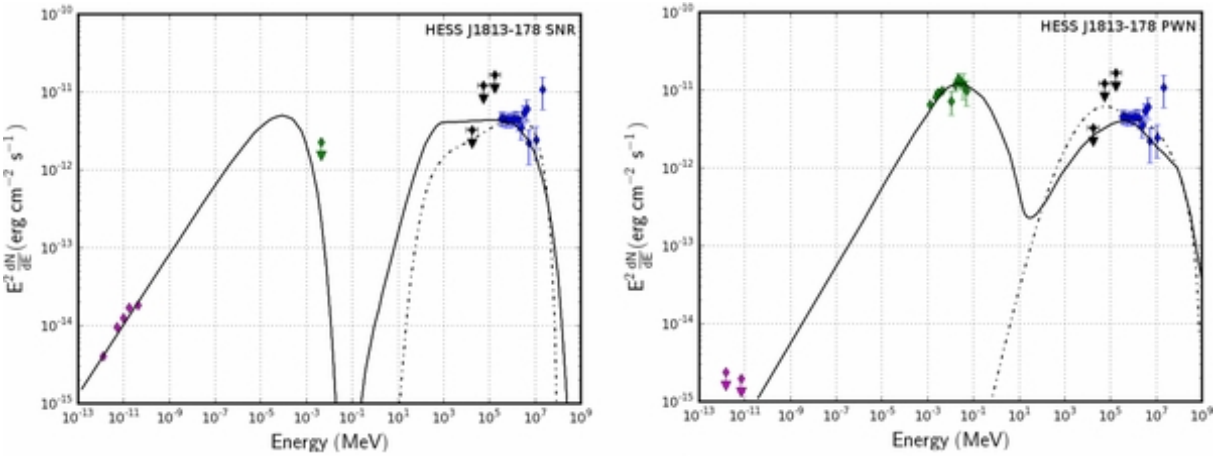

Figure 6.6: HESS J1813-178 model fitting considering the SNR scenario (left), where the emission has a hadronic origin, and the PWN scenario (right), where the emission has a leptonic origin (Acero et al. 2013).

In the context of my work, the most interesting PWNe are the young sources (HESS J1813-178, SNR G054.1+00.3, SNR G21.5-00.9, Kes75 and 3c 58). As already shown, it is possible to model the MWL emission of these sources and infer their physical parame-

ters, needed for example for understanding the acceleration mechanisms and the particle diffusion processes. One of the most interesting objects is HESS J1813-178 that is somewhat difficult to model. This source is associated with the energetic young pulsar PSR J1813-1749 and its GeV-TeV emission can originate either from the PWN, in a leptonic scenario, or from the SNR shell, in a hadronic scenario (Acero et al. 2013). The ASTRI Mini-array can improve the quality of the spectra of HESS (Aharonian et al. 2006b) at energies $\gtrsim 10$ TeV and help to disentangle between the two different scenarios.

Chapter 7

Conclusions

In this Thesis I investigated the prospects for the study of PWNe with CTA and the ASTRI Mini-array. Such systems are among the most powerful TeV emitters in our Galaxy and their investigation allows us to study in great detail the processes related to the acceleration and diffusion of relativistic charged particles. CTA and ASTRI Mini-array will be the next generation of IACTs, and they will have unprecedented sensitivity and energy coverage. This will lead to an increase of the number of observable TeV sources and to an improvement of the accuracy of the measurements, allowing a better understanding of the physical processes acting at these energies. I made use of simulated CTA and ASTRI Mini-array data and of physical models to describe and make predictions on the VHE emission of young PWNe. With this, I studied the capabilities of the arrays to resolve these sources and to extend their energy coverage. I made also a study to assess the impact of systematic uncertainties on the spectral parameters measured with CTA and tested the robustness of the data analysis chain of the ASTRI Mini-array.

I began studying a young PWN in the direction of the Galactic Center: SNR G0.9+0.1. Despite the high background rate in the region, the crowded field and the faintness of the source ($\sim 2\%$ of the Crab flux) I showed that the CTA-South array will allow us to study this PWN with a higher accuracy than that of the currently available instruments. A spatial analysis of SNR G0.9+0.1 shows that, if the VHE emission region is larger than ~ 1.5 arcmin, CTA will be able to resolve it, leading to a measurement of the size of the nebula in the VHE band. Furthermore, the spectral analysis shows that it will be possible to observe the VHE cut-off, if present. It will also be possible to detect

the source at energies higher then 100 TeV if the spectrum is a pure power law, although current leptonic models do not predict such a shape. I then performed a detailed analysis of the systematic errors, showing that the systematics related to the instrumental uncertainties dominate, especially at low energies. Despite these errors may be somewhat overestimated, they provide at least an order of magnitude estimate of the uncertainties that is crucial for the analysis.

I have then implemented a one-zone time-dependent leptonic model that computes the evolution of a young PWN inside a SNR, with the goal of obtaining physical information from the observed spectra of these sources and understanding what impact on the knowledge of PWNe CTA may have. In the case of SNR G0.9+0.1, this was needed to understand which type of spectral shape at VHE is to be expected. From the comparison of the best-fit model on currently available data to the CTA simulated data a high energy cut-off between 20 and 30 TeV is expected. This is a measurement that CTA could easily do. I found also that MWL data will lead to a precise measurement of the magnetization parameter η_B of the nebula and that it is not possible to reproduce a pure power law spectrum. If detected with CTA, this would require a drastic change in the model, such as the introduction of a hadronic component that can account for a certain fraction of the flux emitted at energies $\gtrsim 10 - 100$ TeV. I studied the effects caused by uncertainties on the ISRF and found that, leaving these parameters free the fit leads only to small differences in the computed values of α_2 and η_B. Even approximating a realistic ISRF with two diluted black bodies, the values of α_2 and η_B are not significantly affected.

The analysis was extended to another young PWN: MSH 15-52. The source shows a complex morphology and current models cannot adequately reproduce it. I used the one-zone time-dependent leptonic model and the most recent findings on this source to understand what CTA could do. Assuming that the γ-ray emission comes only from the central PWN, I found that I need a high NIR background to explain the observed IC peak ($\sim$ 30 times the expected values). Following the work by Tsirou et al. (2018), I added a Gaussian component South-East from the position of the pulsar and found that a high NIR background is no longer needed to reproduce the observed data. CTA could clearly disentangle the two regions, measuring the spectra emitted by them in great detail. If we assume a diffusion coefficient of the order of $\kappa \sim 10^{28}$ cm^2 s^{-1} (at 10 TeV) the total energetics of the particles in the Gaussian component is comparable to the energy of the particles that escape from the PWN during its entire lifetime. This could explain the peculiar morphology observed in MSH 15-52. From the analysis of the simulated

TC2 data it is found that there is an indication of an energy-dependent morphology. Observations made with CTA could measure the extension of this component at different energies and give important information on the diffusion of particles inside and outside the PWN. However, to better understand the morphological properties of MSH 15-52, we will also need more advanced multidimensional models that can better reproduce the morphology of the system.

The last work presented in this Thesis was carried out within the framework of the ASTRI/CTA Data Challenge (ACDC) project. I simulated observations of SNR G0.9+0.1 and MSH 15-52 made with the ASTRI Mini-array. SNR G0.9+0.1 has been simulated as a point source and with a spectral cut-off at 30 TeV. The best fit solution is obtained with a PLEC with spectral cut-off $E_{cut} = 35 \pm 18$ TeV (TS= 624). Also the model with a pure power law has good significance, but lower than the case with the PLEC (TS= 617) and the parameters are not consistent with the ones adopted for the simulation. Nevertheless, this simulation shows that the ASTRI Mini-array can be used to detect very faint sources, with the performance expected to increase in regions where the Galactic diffuse emission is less intense. MSH 15-52 has been simulated as superposition of radial Gaussian sources with pure power law spectra. When fitting the simulated data with the three radial Gaussian profiles, it is possible to recover the input spectra within the errors. This means that the ASTRI Mini-array will detect the three regions as point-like, as expected, but also that it can disentangle the emission coming from sources that are very close to each other. This shows that, when studying a situation like this, some assumption on the morphology is required (as often done in the studies of TeV sources), e.g. comparing the TeV morphology with that in the X-ray or radio band.

Finally, I started a study on the prospects of observing PWNe with the ASTRI Mini-array from the Northern hemisphere. I found that almost half of the known and candidate TeV PWNe can be observed from Observatorio del Teide (Canary Islands, Spain) where the ASTRI Mini-array will be installed. A number of interesting sources can be studied, like extend TeV halos and (Geminga), candidate PWNe (HESS J1831-098, 0FGL J0631.8+1034, 0FGL J1958.1+2848, and 0FGL J2021.5+4026) and young PWNe (Crab Nebula, HESS J1813-178, SNR G054.1+00.3, SNR G21.5-00.9, Kes75 and 3c 58). The most interesting source, in this context, is HESS J1813-178. This source is the most luminous young PWN (except, of course, for the Crab Nebula) and the physical origin of its emission is not well understood. The observation of this source with the ASTRI Mini-array could improve the quality of the TeV spectrum at energies higher than 10 TeV

and help to disentangle between different models.

Appendix A

Main radiation processes in PWNe

The main radiation processes in PWNe have origin from the energetic losses suffered by the electrons inside these nebulae.

As described in the main text PWNe are filled by a leptonic population that are accelerated at the termination shock. The two main emission mechanism that we observe, after the shock, are the synchrotron emission and the inverse Compton (IC) mechanism. However, is worth to mention, that also other mechanisms are responsible for the observed emissions, such as the Bremsstrahlung radiation. In some cases is observed that the Synchrotron Self-Compton (SSC), the process of IC by the same electronic population that emitted via synchrotron the seed photons, can be a dominant factor at TeV energies. This is the case, for example, of the Crab Nebula where the SSC dominate over the IC on the other radiation fields (Meyer et al. 2010).

Here we will briefly describe the two main mechanism, focusing on the final photon spectrum originating from a power law distribution of electrons $N_e dE_e = kE_e^{-p} dE_e$ (Longair 2011).

A.1 Synchrotron Radiation

The radiation spectrum coming from a single relativistic electron that moves inside a magnetic field is peaked near a critical frequency ν_c:

$$\nu_c = \gamma^2 \nu_g = \left(\frac{E_e}{m_e c^2}\right)^2 \nu_g; \qquad \nu_g = \frac{eB}{2\pi m_e} \tag{A.1}$$

where ν_g is the gyration frequency for sub-relativistic particles, e the electron charge, m_e the electron mass and B the magnetic field strength. ν_c is the frequency at which most of the radiation is emitted and so we can approximate for a single electron that $\nu \approx \nu_c$ in the next formulae.

The electrons in an energy range E_e and $E_e + dE_e$ can radiate photons with frequencies between ν and $\nu + d\nu$, and therefore the specific emissivity is:

$$J(\nu)d\nu = -\left(\frac{dE_e}{dt}\right) N_e dE_e. \tag{A.2}$$

We know the term $N_e dE_e$ (the power law distribution of the electrons) and also the term in the parenthesis, that is the energy losses rate suffered by the electrons due to the synchrotron emission:

$$-\left(\frac{dE_e}{dt}\right) = 2\sigma_T c \frac{B^2}{2\mu_0}\left(\frac{E_e}{m_e c^2}\right)^2 \sin^2\theta = \frac{4}{3}\sigma_T c \frac{B^2}{2\mu_0}\left(\frac{E_e}{m_e c^2}\right)^2 \tag{A.3}$$

where we have considered an isotropic distribution of pitch angles θ (the angle that the velocity vector makes with the magnetic field lines), so that $< sin^2\theta >= 2/3$. Considering also the following expressions for the energy (from equation A.1):

$$E_e = \left(\frac{\nu}{\nu_g}\right)^{1/2} m_e c^2; \qquad dE_e = \frac{m_e c^2}{2\nu_g^{1/2}} \nu^{1/2} d\nu \tag{A.4}$$

inserting this terms and equation A.3 in equation A.2 we find:

$$J(\nu) \propto k B^{(p+1)/2} \nu^{-(p-1)/2}. \propto \nu^{-\alpha} \tag{A.5}$$

This result shows that a power law distribution of electrons produces a power law spectrum

and the two spectral indices, p and $\alpha = (p-1)/2$, are related.

The total final spectrum is interpreted as the superposition of many contributions from the various electrons.

A.2 Inverse Compton

We now consider the case in which in the nebula there are photons with typical energies much lower than the energies of the electrons. This is the case for photons originating from stellar emissions (what we call in the main text near-infrared emissions), diffuse emissions due to the interstellar medium (what we call in the main text far-infrared emissions) and the cosmic microwave background. When the electrons have energies greater then the typical photon energy there can be a transfer of energy from the electrons to the photons. This is the process called IC.

In the IC process, the emission spectrum for a single particle is highly peaked at a frequency ν_1 that is boosted by a factor γ^2 with respect to the original frequency ν of the incident photon field (Blumenthal & Gould 1970):

$$< \nu_1 >= \frac{4}{3}\gamma^2 < \nu >= \frac{4}{3}\left(\frac{E_e}{m_e c^2}\right)^2 < \nu > \tag{A.6}$$

where $< \nu >$ is the mean frequency of the photons in the field.

In the case that the Thompson limit is valid the total energy loss rate of a single electron can be estimate as (Rybicki & Lightman 1979):

$$-\left(\frac{dE_e}{dt}\right) = \frac{4}{3}\sigma_T c u_{rad}\left(\frac{E_e}{m_e c^2}\right)^2 \tag{A.7}$$

where u_{rad} is the energy density of the photon field. If we consider a photon field that is monochromatic ($< \nu >= \nu_0$) we found similar expressions as for the synchrotron radiation. This again reflects on the relation between the spectral index of the power law distribution of the electrons and the spectral index of emitted spectrum that is $\alpha = (p-1)/2$.

In the more general case, where the incoming photons are not monochromatic, the general equation for the up-scattered photon spectrum per electron is given by (Blumen-

thal & Gould 1970):

$$\frac{dN_{\gamma,\epsilon}}{dtdE_1} = \frac{2\pi r_e^2 m_e c^3}{\gamma}\frac{n(\epsilon)d\epsilon}{\epsilon}\left[2q\ln q + (1+2q)(1-q) + \frac{(\Gamma_e q)^2}{2(1+\Gamma_e q}(1-q)\right] \tag{A.8}$$

where ϵ is the initial photon energy, $n(\epsilon)$ the radiation field density and $E_1 = \epsilon_1/E_e$ the ratio between the energy of the scattered photons and the electron energy. The two dimensionless quantities Γ_e and q can be written as:

$$\Gamma_e = \frac{4\epsilon\gamma}{m_e c^2}; \qquad q = \frac{E_1}{\Gamma_e(1-E_1)}. \tag{A.9}$$

The total IC spectrum can be then computed integrating this equation over the electron distribution and the input photon field energy. This equation is also valid in the case of the Klein-Nishima regime, when the relative electron-photon cross section decrease and the most energetic electrons ($E_e \gtrsim 1$ TeV) mainly interact with very low energy photons.

Appendix B

General form of the energy diffusion equation

Here we describe in detail the energy-diffusion equation used in this work, starting from its general, non-simplified form (Ginzburg & Syrovatskii 1964):

$$\begin{aligned}\frac{\partial N_i(E,\vec{r},t)}{\partial t} &= \nabla\cdot[D_i(E,\vec{r},t)\nabla N_i(E,\vec{r},t)] - \frac{\partial}{\partial E}[b_i(E)N_i(E,\vec{r},t)] \\ &+ \frac{1}{2}\frac{\partial^2}{\partial E^2}[d_i(E)N_i(E,\vec{r},t)] + Q_i(E,\vec{r},t) \\ &- \frac{N_i(E,\vec{r},t)}{\tau_i(E,\vec{r},t)} + \sum_k \int P_i^k(E',E)N_k(E',\vec{r},t)dE,\end{aligned} \tag{B.1}$$

$N_i(E,\vec{r},t)$ is the concentration of particles species denoted with the subscript i. The first term on the right-hand side describes the spatial diffusion of particles inside the nebula and $D_i(e,\vec{r},t)$ is the diffusion coefficient. The second term describes the continuous energy variation due to acceleration processes and energy losses, including adiabatic, synchrotron and Inverse Compton (IC) losses. The function $b_i(E)$ is the mean energy variation of the particle in unit time. The third term is related to fluctuations in this continuous variation of energy of the particles, whereas the function $d_i(E)$ is equal to the mean square of the energy variation per unit time. The term $Q_i(E,\vec{r},t)$ is the particle injection rate, which in this case originates from the acceleration of the particles at the termination shock. The fifth term accounts for the escape of particles from the system with the characteristic timescale $\tau_i(E,\vec{r},t)$. Finally, the last term accounts for the creation and annihilation of

particles with a probability distribution $P_i^k(E', E)$ (Ginzburg & Syrovatskii 1964).

The equation B.1 cannot be easily solved. Suitable approximations are usually made. First of all, we consider only one population of particles (electrons), we neglect pair creation or annihilation and we take only the mean value of the energy losses per unit energy, neglecting any fluctuations in the continuous energy variation. We also assume an isotropic distribution of electrons, an isotropic injection term inside the nebula and an isotropic magnetic field (no diffusion effect). With these approximations we can neglect the first, the third and the last term in equation B.1, that becomes equation 4.1 from Section 4.2.

Appendix C

Radius and velocity evolution of Pulsar Wind Nebulae

In this appendix we describe an iterative method similar to that from Gelfand et al. (2009), which we use to compute the radius R_{pwn} and the expansion velocity v_{pwn} of the PWN in each time step. For this, it is necessary to take into account an interaction between the SNR and the PWN expanding inside it.

First of all, we determine the properties of the ejected material between the reverse shock of the remnant and the nebula. Making a standard assumption that an inner core with initially constant density is surrounded by an outer envelope with density proportional to r^9 (Blondin et al. 2001; Truelove & McKee 1999), the density of the ejecta can be written as:

$$\rho_{ej}(r,t) = \begin{cases} \frac{10}{9\pi} E_{sn} v_t^{-5} t^{-3} & \text{for } r \leq v_t t \\ \frac{10}{9\pi} E_{sn} v_t^{-5} t^{-3} (\frac{r}{v_t t})^{-9} & \text{for } r > v_t t \end{cases}, \tag{C.1}$$

where $v_t = (40E_{sn}/18M_{ej})^{1/2}$ is the transition velocity between the constant density core and the outer envelope, E_{sn} is an energy of the supernova explosion and M_{ej} is its ejected mass. The ejecta during this stage is expanding ballistically and, therefore, its velocity is equal to $v_{ej} = r/t$. Since in this work we study young PWNe, which have not reach the reverse shock of the SNR yet, we are not aiming in further modelling of the ejecta.

We adopt a thin-shell approximation (Chevalier 2005), considering that the expanding PWN is surrounded by a thin shell of swept-up material.

The initial conditions for our iterative procedure, needed to estimate the radius and the associated expansion velocity, are determined as described below. Considering the standard approximation of an isobaric bubble inside the thin-shell, where the adiabatic losses are dominant, the equation of motion of the mass of the shell M_s can be written as (Ostriker & Gunn 1971; Chevalier 1977)

$$M_s \frac{d^2R}{dt^2} = 4\pi R_{pwn}^2 \left[P_{pwn} - \rho_{ej} \left(\frac{dR_{pwn}}{dt} - v_{ej} \right)^2 \right], \tag{C.2}$$

where ρ_{ej} and v_{ej} are computed at R_{pwn}, and P_{pwn} is the pressure inside the nebula. From the first law of thermodynamics we can write the following expression:

$$\frac{dE_{pwn}}{dt} = L(t) - 4\pi P_{pwn} R_{pwn}^2 \frac{dR_{pwn}}{dt}. \tag{C.3}$$

This equation is possible to solve in the approximation of $t_0 \ll \tau_0$ where $L(t_0) \simeq L_0$. Putting together equations C.1, C.2 and C.3, we obtain the following initial condition for the radius and expansion velocity (Chevalier 1977; Blondin et al. 2001):

$$R_{pwn}(t_0) = 1.44 \left(\frac{E_{sn}^3 L_0^2}{M_{ej}^5} \right)^{1/10} t_0^{6/5}, \tag{C.4}$$

$$v_{pwn}(t_0) \equiv \frac{dR_{pwn}}{dt}(t_0) = \frac{6}{5} \frac{R_{pwn}(t_0)}{t_0}. \tag{C.5}$$

With this initial condition we can start the iterations, computing new radius of the PWN ($R_{pwn}(t + \Delta t)$) together with the magnetic field in the nebula $B_{pwn}(t + \Delta t)$ (equation 4.11), the spin-down luminosity $L(t + \Delta t)$ (equation 4.3), the maximum energy of the electrons $E_{max}(t + \Delta t)$ (equation 4.9), and the density and the velocity of the ejecta at $R_{pwn}(t + \Delta t)$.

$$R_{pwn}(t + \Delta t) = R_{pwn}(t) + v_{pwn}(t)\Delta t. \tag{C.6}$$

As a second step, we computed the pressure inside the nebula, in order to determine the force acting on the shell and, therefore, a new value of the expansion velocity of the PWN. The net force which affects the shell is proportional to the difference between the pressure inside P_{pwn} and outside the nebula P_{ej}:

$$F_{pwn} \equiv \frac{d}{dt}(M_s v_{pwn}) = 4\pi R_{pwn}^2 (P_{pwn} - P_{ej}). \tag{C.7}$$

However, the second term of this expression can be neglected since it is expected that $P_{pwn} \gg P_{ej}$.

The total pressure inside the nebula is determined as a sum of the pressure of the magnetic field $P_{pwn,B}$ and that of the moving electrons $P_{pwn,e}$. Calculating the value of the magnetic field B_{pwn} from equation 4.11, we can determine the energy stored in the magnetic field:

$$E_{pwn,B}(t) = \left(\frac{B^2_{pwn}(t)}{8\pi}\right)\frac{4\pi}{3}R^3_{pwn}(t). \tag{C.8}$$

From equation C.8 we obtain $P_{pwn,B}$ as:

$$P_{pwn,B}(t) = \frac{E_{pwn,B}(t)}{\frac{4\pi}{3}R^3_{pwn}(t)} = \frac{B^2_{pwn}(t)}{8\pi}. \tag{C.9}$$

The contribution of the second component $P_{pwn,e}$ can be computed solving equation 4.1 and extracting the total energy from the spectrum of evolved particles:

$$E_{pwn,e}(t) = \int_{E_{min}}^{E_{max}} EN(E,t)dE. \tag{C.10}$$

Then, the electron pressure is found as follows:

$$P_{pwn,e}(t) = (\gamma_{pwn} - 1)\frac{E_{pwn,e}(t)}{\frac{4\pi}{3}R^3_{pwn}(t)} = \frac{E_{pwn,e}(t)}{4\pi R^3_{pwn}(t)}, \tag{C.11}$$

where γ_{pwn} is equal to 4/3.

Finally, we are able to compute the new expansion velocity of the nebula. If $v_{pwn}(t) > v_{ej}(t)$ the new mass of the shell becomes

$$M_s(t+\Delta t) = M_s(t) + \frac{4\pi}{3}\left[R^3_{pwn}(t+\Delta t) - R^3_{pwn}(t)\right]\rho_{ej}(t+\Delta t). \tag{C.12}$$

Otherwise, new mass $M_s(t+\Delta t)$ is simply equal to $M_s(t)$. The new velocity $v_{pwn}(t+\Delta t)$, which will be used for calculating the radius of PWN in the next iteration, can be found from the following expression:

$$v_{pwn}(t+\Delta t) = \frac{M_s(t)v_{pwn}(t) + \Delta M_s v_{ej}(t) + F_{pwn}(t)\Delta t}{M_s(t+\Delta t)}, \tag{C.13}$$

where $\Delta M_s = M_s(t + \Delta t) - M_s(t)$.

To compute an evolution of leptons using this iterative procedure, we solve advective equation 4.1 many times. In the case of high energy losses, these computations can become time-consuming. To speed up the calculations, we put an upper limit on the magnetic field inside the nebula during the first stages of evolution of the system. We impose that magnetic field does not exceed $2000\,\mu G$ during the first 5 yrs and it is $< 200\,\mu G$ until 500 yrs of evolution. These constraints introduce modest impact to the calculation of the radius of the source. The resulting value of the radius is $< 5\%$ higher than that computed with no upper limits on the magnetic field. We note that once the values needed to determine the evolution of the nebula are obtained, we recalculate the particle spectrum without any limit on the magnetic field. We also checked that the final photon spectrum does not differ significantly from the one obtained using no upper limits on the maximum value of the magnetic field.

Appendix D

Model fitting

In our fitting procedure, we first compute a grid of models spanning a large range of values of free parameters. We then compute the chi-square χ^2 statistics for each model of the grid and the observational data and choose the best-fit model with the minimal χ^2. As mentioned in Section 4.2.1, we leave free to vary only 3 parameters: α_2, η_B and ϵ. Other two parameters E_b and α_1 are fixed to values as in Zhu et al. (2018) in order to perform a comparison with their results. Finally, we estimate the uncertainties of the free parameters using the following procedure:

- We produce a three-dimensional (3D) probability grid from the χ^2 values obtained for all the models:

$$P_{3D}(\alpha_2, \eta_B, \epsilon) \propto \exp\left(-\chi^2/2\right), \tag{D.1}$$

- and normalize it:

$$\sum_{\alpha_2,\eta_B,\epsilon} P_{3D}(\alpha_2, \eta_B, \epsilon) = 1, \tag{D.2}$$

- We then extract the marginalized (1D) probability distribution for each parameter summing over other two parameters:

$$P_{1D}(\alpha_2) = \sum_{\eta_B,\epsilon} P_{3D}(\alpha_2, \eta_B, \epsilon), \tag{D.3}$$

$$P_{1D}(\eta_B) = \sum_{\alpha_2,\epsilon} P_{3D}(\alpha_2, \eta_B, \epsilon), \tag{D.4}$$

$$P_{1D}(\epsilon) = \sum_{\alpha_2,\eta_B} P_{3D}(\alpha_2, \eta_B, \epsilon). \tag{D.5}$$

- Finally, using these marginalized probability distributions, we estimate the confidence interval and 1σ error for each parameter, assuming that the distributions are Gaussian.

References

Abdo, A. A., Allen, B. T., Aune, T., et al. 2009, Milagro Observations of Multi-TeV Emission from Galactic Sources in the Fermi Bright Source List, ApJ, 700, L127

Abdo, A. A., Ackermann, M., Ajello, M., et al. 2010, Detection of the Energetic Pulsar PSR B1509-58 and its Pulsar Wind Nebula in MSH 15-52 Using the Fermi-Large Area Telescope, ApJ, 714, 927

Abeysekara, A. U., Alfaro, R., Alvarez, C., et al. 2013, Sensitivity of the high altitude water Cherenkov detector to sources of multi-TeV gamma rays, Astroparticle Physics, 50, 26

Abeysekara, A. U., Albert, A., Alfaro, R., et al. 2017, Observation of the Crab Nebula with the HAWC Gamma-Ray Observatory, The Astrophysical Journal, 843, 39

Acero, F., Aharonian, F., Akhperjanian, A. G., et al. 2010, Localizing the VHE γ-ray source at the Galactic Centre, MNRAS, 402, 1877

Acero, F., Ackermann, M., Ajello, M., et al. 2013, Constraints on the Galactic Population of TeV Pulsar Wind Nebulae Using Fermi Large Area Telescope Observations, ApJ, 773, 77

—. 2015, Fermi Large Area Telescope Third Source Catalog, ApJS, 218, 23

Acharya, B. S., Actis, M., Aghajani, T., et al. 2013, Introducing the CTA concept, Astroparticle Physics, 43, 3

Acharyya, A., Agudo, I., Angüner, E. O., et al. 2019, Monte Carlo studies for the optimisation of the Cherenkov Telescope Array layout, Astroparticle Physics, 111, 35

Ackermann, M., Ajello, M., Albert, A., et al. 2012, The Fermi Large Area Telescope on Orbit: Event Classification, Instrument Response Functions, and Calibration, ApJS, 203, 4

Ackermann, M., Ajello, M., Allafort, A., et al. 2013, The First Fermi-LAT Catalog of Sources above 10 GeV, ApJS, 209, 34

Aharonian, F. 2013, Gamma Rays at Very High Energies (Berlin, Heidelberg: Springer Berlin Heidelberg), 1–120

Aharonian, F., Akhperjanian, A. G., Aye, K.-M., et al. 2004, Very high energy gamma rays from the direction of Sagittarius A*, A&A, 425, L13

Aharonian, F., Akhperjanian, A. G., Aye, K. M., et al. 2005a, Discovery of extended VHE gamma-ray emission from the asymmetric pulsar wind nebula in MSH 15-52 with HESS, A&A, 435, L17

Aharonian, F., Akhperjanian, A. G., Aye, K.-M., et al. 2005b, Very high energy gamma rays from the composite SNR G 0.9+0.1, A&A, 432, L25

Aharonian, F., Akhperjanian, A. G., Bazer-Bachi, A. R., et al. 2006a, Discovery of very-high-energy γ-rays from the Galactic Centre ridge, Nature, 439, 695

—. 2006b, The H.E.S.S. Survey of the Inner Galaxy in Very High Energy Gamma Rays, ApJ, 636, 777

Aharonian, F., Akhperjanian, A. G., Barres de Almeida, U., et al. 2008, Exploring a SNR/molecular cloud association within HESS J1745-303, A&A, 483, 509

Aharonian, F., Akhperjanian, A. G., Anton, G., et al. 2009, Spectrum and variability of the Galactic center VHE γ-ray source HESS J1745-290, A&A, 503, 817

Aharonian, F. A. 2004, Very High Energy Cosmic Gamma Radiation (WORLD SCIENTIFIC), https://www.worldscientific.com/doi/pdf/10.1142/4657

Aharonian, F. A., Atoyan, A. M., & Kifune, T. 1997, Inverse Compton gamma radiation of faint synchrotron X-ray nebulae around pulsars, MNRAS, 291, 162

Ahnen, M. L., Ansoldi, S., Antonelli, L. A., et al. 2015, Very High Energy γ-Rays from the Universe's Middle Age: Detection of the z = 0.940 Blazar PKS 1441+25 with MAGIC, ApJ, 815, L23

—. 2017, Observations of Sagittarius A* during the pericenter passage of the G2 object with MAGIC, A&A, 601, A33

Aleksić, J., Antonelli, L. A., Antoranz, P., et al. 2010, MAGIC Upper Limits for Two Milagro-detected Bright Fermi Sources in the Region of SNR G65.1+0.6, ApJ, 725, 1629

Aleksić, J., Ansoldi, S., Antonelli, L. A., et al. 2016, The major upgrade of the MAGIC telescopes, Part I: The hardware improvements and the commissioning of the system, Astroparticle Physics, 72, 61

Aleksi, J., Ansoldi, S., Antonelli, L., et al. 2016, The major upgrade of the MAGIC telescopes, Part II: A performance study using observations of the Crab Nebula, Astroparticle Physics, 72, 76

Amato, E. 2014, in International Journal of Modern Physics Conference Series, Vol. 28, International Journal of Modern Physics Conference Series, 1460160

Amato, E., Guetta, D., & Blasi, P. 2003, Signatures of high energy protons in pulsar winds, A&A, 402, 827

An, H., Madsen, K. K., Reynolds, S. P., et al. 2014, High-energy X-Ray Imaging of the Pulsar Wind Nebula MSH 15-52: Constraints on Particle Acceleration and Transport, ApJ, 793, 90

Archer, A., Benbow, W., Bird, R., et al. 2016, TeV Gamma-Ray Observations of the Galactic Center Ridge by VERITAS, ApJ, 821, 129

Arons, J., & Scharlemann, E. T. 1979, Pair formation above pulsar polar caps: structure of the low altitude acceleration zone., The Astrophysical Journal, 231, 854

Atoyan, A. M., & Aharonian, F. A. 1996, On the mechanisms of gamma radiation in the Crab Nebula, MNRAS, 278, 525

Bednarek, W., & Idec, W. 2011, On the variability of the GeV and multi-TeV gamma-ray emission from the Crab nebula, MNRAS, 414, 2229

Bednarek, W., & Protheroe, R. J. 1997, Gamma Rays and Neutrinos from the Crab Nebula Produced by Pulsar Accelerated Nuclei, Phys. Rev. Lett., 79, 2616

Begelman, M. C., & Li, Z.-Y. 1992, An Axisymmetric Magnetohydrodynamic Model for the Crab Pulsar Wind Bubble, The Astrophysical Journal, 397, 187

Bernlöhr, K. 2008, in American Institute of Physics Conference Series, Vol. 1085, American Institute of Physics Conference Series, ed. F. A. Aharonian, W. Hofmann, & F. Rieger, 874–877

Bernlöhr, K., Barnacka, A., Becherini, Y., et al. 2013, Monte Carlo design studies for the Cherenkov Telescope Array, Astroparticle Physics, 43, 171

Bhattacharya, D. 1990, On the morphology of supernova remnants with pulsars., Journal of Astrophysics and Astronomy, 11, 125

Bigongiari, C., & CTA Consortium. 2016, The Cherenkov Telescope Array, Nuclear and Particle Physics Proceedings, 279, 174

Blandford, R., & Eichler, D. 1987, Particle acceleration at astrophysical shocks: A theory of cosmic ray origin, Phys. Rep., 154, 1

Blandford, R. D. 2002, in Lighthouses of the Universe: The Most Luminous Celestial Objects and Their Use for Cosmology, ed. M. Gilfanov, R. Sunyeav, & E. Churazov, 381

Blandford, R. D., & Romani, R. W. 1988, On the interpretation of pulsar braking indices., MNRAS, 234, 57P

Blondin, J. M., Chevalier, R. A., & Frierson, D. M. 2001, Pulsar Wind Nebulae in Evolved Supernova Remnants, ApJ, 563, 806

Blumenthal, G. R., & Gould, R. J. 1970, Bremsstrahlung, Synchrotron Radiation, and Compton Scattering of High-Energy Electrons Traversing Dilute Gases, Reviews of Modern Physics, 42, 237

Boettcher, M. 2010, Models for the Spectral Energy Distributions and Variability of Blazars, arXiv e-prints, arXiv:1006.5048

Bogovalov, S. V. 1999, On the physics of cold MHD winds from oblique rotators, A&A, 349, 1017

Brazier, K. T. S., & Becker, W. 1997, High-resolution X-ray imaging of the supernova remnant MSH 15-52, MNRAS, 284, 335

Brown, A. M., Abchiche, A., Allan, D., et al. 2016, in Society of Photo-Optical Instrumentation Engineers (SPIE) Conference Series, Vol. 9906, Proc. SPIE, 99065K

Bucciantini, N., Amato, E., Bandiera, R., Blondin, J. M., & Del Zanna, L. 2004, Magnetic Rayleigh-Taylor instability for Pulsar Wind Nebulae in expanding Supernova Remnants, A&A, 423, 253

Bucciantini, N., Arons, J., & Amato, E. 2011, Modelling spectral evolution of pulsar wind nebulae inside supernova remnants, MNRAS, 410, 381

Bucciantini, N., & Bandiera, R. 2001, Pulsar bow-shock nebulae. I. Physical regimes and detectability conditions, Astronomy and Astrophysics, 375, 1032

Bucciantini, N., Blondin, J. M., Del Zanna, L., & Amato, E. 2003, Spherically symmetric relativistic MHD simulations of pulsar wind nebulae in supernova remnants, Astronomy and Astrophysics, 405, 617

Bucciantini, N., Thompson, T. A., Arons, J., Quataert, E., & Del Zanna, L. 2006, Relativistic magnetohydrodynamics winds from rotating neutron stars, Monthly Notices of the Royal Astronomical Society, 368, 1717

Buehler, R., Scargle, J. D., Blandford, R. D., et al. 2012, Gamma-Ray Activity in the Crab Nebula: The Exceptional Flare of 2011 April, ApJ, 749, 26

Bühler, R., & Blandford, R. 2014, The surprising Crab pulsar and its nebula: a review, Reports on Progress in Physics, 77, 066901

Burtovoi, A., Saito, T. Y., Zampieri, L., & Hassan, T. 2017, Prospects for the detection of high-energy (E > 25 GeV) Fermi pulsars with the Cherenkov Telescope Array, MNRAS, 471, 431

Camilo, F., Ransom, S. M., Gaensler, B. M., & Lorimer, D. R. 2009, Discovery of the Energetic Pulsar J1747-2809 in the Supernova Remnant G0.9+0.1, ApJ, 700, L34

Carrigan, S., Brun, F., Chaves, R. C. G., et al. 2013, Charting the TeV Milky Way: H.E.S.S. Galactic plane survey maps, catalog and source populations, arXiv e-prints, arXiv:1307.4868

Caswell, J. L., Milne, D. K., & Wellington, K. J. 1981, High-resolution radio observations of five supernova remnants, MNRAS, 195, 89

Cheng, K. S., Cheung, T., Lau, M. M., Yu, K. N., & Kwok, P. W. 1990, Could very high energy gamma rays from the Crab Nebula result from p-p collision?, Journal of Physics G Nuclear Physics, 16, 1115

Cheng, K. S., Ho, C., & Ruderman, M. 1986, Energetic Radiation from Rapidly Spinning Pulsars. I. Outer Magnetosphere Gaps, The Astrophysical Journal, 300, 500

Cheng, K. S., Ruderman, M., & Zhang, L. 2000, A Three-dimensional Outer Magnetospheric Gap Model for Gamma-Ray Pulsars: Geometry, Pair Production, Emission Morphologies, and Phase-resolved Spectra, ApJ, 537, 964

Cherenkov, P. A. 1934, Visible Radiation Produced by Electrons Moving in a Medium with Velocities Exceeding that of Light, C. R. (Doklady) Akad. Sci. URSS, 2, 451

Chevalier, R. A. 1977, in Astrophysics and Space Science Library, Vol. 66, Supernovae, ed. D. N. Schramm, 53

Chevalier, R. A. 1998, Pulsar nebulae in supernovae., Memorie della Societa Astronomica Italiana, 69, 977

—. 2005, Young Core-Collapse Supernova Remnants and Their Supernovae, ApJ, 619, 839

Coroniti, F. V. 1990, Magnetically Striped Relativistic Magnetohydrodynamic Winds: The Crab Nebula Revisited, ApJ, 349, 538

CTA Consortium. 2018, CTA December 2018 Newsletter, https://mailchi.mp/41fe652a9123/cta-newsletter-dec2018#Wolfgang

—. 2019, Science with the Cherenkov Telescope Array (World Scientific Publishing Co. Pte. Ltd.), doi:10.1142/10986

Cui, W. 2009, TeV gamma-ray astronomy, Research in Astronomy and Astrophysics, 9, 841

Cumani, P., Hassan, T., Arrabito, L., et al. 2017, Baseline telescope layouts of the Cherenkov Telescope Array, International Cosmic Ray Conference, 301, 811

Daugherty, J. K., & Harding, A. K. 1982, Electromagnetic cascades in pulsars., The Astrophysical Journal, 252, 337

Davies, J. M., & Cotton, E. S. 1957, Design of the quartermaster solar furnace, Solar Energy, 1, 16

De Angelis, A., & Pimenta, M. 2018, Introduction to Particle and Astroparticle Physics (Springer), doi:10.1007/978-3-319-78181-5

de Jager, O. C., & Djannati-Ataï, A. 2009, in Astrophysics and Space Science Library, Vol. 357, Astrophysics and Space Science Library, ed. W. Becker, 451

de Jager, O. C., Harding, A. K., Michelson, P. F., et al. 1996, Gamma-Ray Observations of the Crab Nebula: A Study of the Synchro-Compton Spectrum, ApJ, 457, 253

de Jager, O. C., Slane, P. O., & LaMassa, S. 2008, Probing the Radio to X-Ray Connection of the Vela X Pulsar Wind Nebula with Fermi LAT and H.E.S.S., The Astrophysical Journal, 689, L125

de Naurois, M., & Mazin, D. 2015, Ground-based detectors in very-high-energy gamma-ray astronomy, Comptes Rendus Physique, 16, 610 , gamma-ray astronomy / Astronomie des rayons gamma

de Naurois, M., & Mazin, D. 2015, Ground-based detectors in very-high-energy gamma-ray astronomy, Comptes Rendus Physique, 16, 610

Deil, C., Zanin, R., Lefaucheur, J., et al. 2017, in International Cosmic Ray Conference, Vol. 301, 35th International Cosmic Ray Conference (ICRC2017), 766

Di Palma, I., Guetta, D., & Amato, E. 2017, Revised Predictions of Neutrino Fluxes from Pulsar Wind Nebulae, ApJ, 836, 159

Di Sciascio, G. 2019, in Journal of Physics Conference Series, Vol. 1263, Journal of Physics Conference Series, 012003

Donath, A., Deil, C., Arribas, M. P., et al. 2015, in International Cosmic Ray Conference, Vol. 34, 34th International Cosmic Ray Conference (ICRC2015), 789

Dubner, G., Castelletti, G., Kargaltsev, O., et al. 2017, Morphological Properties of the Crab Nebula: A Detailed Multiwavelength Study Based on New VLA, HST, Chandra, and XMM-Newton Images, ApJ, 840, 82

Dubner, G., Giacani, E., & Decourchelle, A. 2008, High resolution radio study of the pulsar wind nebula within the supernova remnant G0.9+0.1, A&A, 487, 1033

Dyks, J., & Rudak, B. 2003, Two-Pole Caustic Model for High-Energy Light Curves of Pulsars, The Astrophysical Journal, 598, 1201

Engel, R., Heck, D., & Pierog, T. 2011, Extensive Air Showers and Hadronic Interactions at High Energy, Annual Review of Nuclear and Particle Science, 61, 467

Evoli, C. 2018, The Cosmic-Ray Energy Spectrum, doi:10.5281/zenodo.2360277

Fang, J., & Zhang, L. 2010, Multiband emission from pulsar wind nebulae: a possible injection spectrum, A&A, 515, A20

Fermi-LAT collaboration. 2019a, Fermi Large Area Telescope Fourth Source Catalog, arXiv e-prints, arXiv:1902.10045

—. 2019b, LAT public performance, https://www.slac.stanford.edu/exp/glast/groups/canda/lat_Performance.htm

Fernandez-Barral, A., Blanch, O., Chatterjee, A., de Oña Wilhelmi, E., & Fidalgo, D. 2017, in International Cosmic Ray Conference, Vol. 35, 35th International Cosmic Ray Conference (ICRC2017), 733

Foreman-Mackey, D., Hogg, D. W., Lang, D., & Goodman, J. 2013, emcee: The MCMC Hammer, PASP, 125, 306

Forot, M., Hermsen, W., Renaud, M., et al. 2006, High-Energy Particles in the Wind Nebula of Pulsar B1509-58 as Seen by INTEGRAL, ApJ, 651, L45

Funk, S. 2015, Ground- and Space-Based Gamma-Ray Astronomy, Annual Review of Nuclear and Particle Science, 65, 245

Gaensler, B. M., Arons, J., Kaspi, V. M., et al. 2002, Chandra Imaging of the X-Ray Nebula Powered by Pulsar B1509-58, ApJ, 569, 878

Gaensler, B. M., Brazier, K. T. S., Manchester, R. N., Johnston, S., & Green, A. J. 1999, SNR G320.4-01.2 and PSR B1509-58: new radio observations of a complex interacting system, MNRAS, 305, 724

Gaensler, B. M., Pivovaroff, M. J., & Garmire, G. P. 2001, Chandra Observations of the Pulsar Wind Nebula in Supernova Remnant G0.9+0.1, ApJ, 556, L107

Gaensler, B. M., & Slane, P. O. 2006, The Evolution and Structure of Pulsar Wind Nebulae, Annual Review of Astronomy and Astrophysics, 44, 17

Gaensler, B. M., van der Swaluw, E., Camilo, F., et al. 2004, The Mouse that Soared: High-Resolution X-Ray Imaging of the Pulsar-powered Bow Shock G359.23-0.82, The Astrophysical Journal, 616, 383

Gaggero, D., Urbano, A., Valli, M., & Ullio, P. 2015, Gamma-ray sky points to radial gradients in cosmic-ray transport, Phys. Rev. D, 91, 083012

Gallant, Y. A., & Arons, J. 1994, Structure of Relativistic Shocks in Pulsar Winds: A Model of the Wisps in the Crab Nebula, The Astrophysical Journal, 435, 230

Gelfand, J. D. 2017, in Modelling Pulsar Wind Nebulae, ed. D. F. Torres, Vol. 446, 161

Gelfand, J. D., Slane, P. O., & Zhang, W. 2009, A Dynamical Model for the Evolution of a Pulsar Wind Nebula Inside a Nonradiative Supernova Remnant, ApJ, 703, 2051

Ghisellini, G., Guilbert, P. W., & Svensson, R. 1988, The synchrotron boiler, ApJ, 334, L5

Giacinti, G., Mitchell, A. M. W., López-Coto, R., et al. 2019, On the TeV Halo Fraction in gamma-ray bright Pulsar Wind Nebulae, arXiv e-prints, arXiv:1907.12121

Ginzburg, V. L. 1979, Theoretical physics and astrophysics (nternational Series in Natural Philosophy, Oxford: Pergamon)

Ginzburg, V. L., & Syrovatskii, S. I. 1964, The Origin of Cosmic Rays (Macmillan)

Giro, E., Canestrari, R., Sironi, G., et al. 2017, First optical validation of a Schwarzschild Couder telescope: the ASTRI SST-2M Cherenkov telescope, A&A, 608, A86

Goldreich, P., & Julian, W. H. 1969, Pulsar Electrodynamics, ApJ, 157, 869

Gotthelf, E. V. 2004, in IAU Symposium, Vol. 218, Young Neutron Stars and Their Environments, ed. F. Camilo & B. M. Gaensler, 225

Granot, J., Gill, R., Younes, G., et al. 2017, Learning about the magnetar Swift J1834.9-0846 from its wind nebula, MNRAS, 464, 4895

Gvaramadze, V. V. 2001, On the age of PSR B 1509-58, A&A, 374, 259

H. E. S. S. Collaboration, :, Abdalla, H., et al. 2017, Characterising the VHE diffuse emission in the central 200 parsecs of our Galaxy with H.E.S.S, ArXiv e-prints, arXiv:1706.04535

H. E. S. S. Collaboration, Abdalla, H., Aharonian, F., et al. 2018a, First ground-based measurement of sub-20 GeV to 100 GeV γ-Rays from the Vela pulsar with H.E.S.S. II, A&A, 620, A66

H. E. S. S. Collaboration, Abdalla, H., Abramowski, A., et al. 2018b, The population of TeV pulsar wind nebulae in the H.E.S.S. Galactic Plane Survey, A&A, 612, A2

Hahn, J. 2015, in 34th International Cosmic Ray Conference (ICRC2015), Vol. 34, 917

Harding, A. K. 2013, Pulsar Polar Cap and Slot Gap Models: Confronting Fermi Data, Journal of Astronomy and Space Sciences, 30, 145

Harding, A. K., Tademaru, E., & Esposito, L. W. 1978, A curvature - radiation - pair-production model for gamma -ray pulsars., The Astrophysical Journal, 225, 226

Hassan, T., Arrabito, L., Bernlör, K., et al. 2015, Second large-scale Monte Carlo study for the Cherenkov Telescope Array, ArXiv e-prints, arXiv:1508.06075

Hassan, T., Arrabito, L., Bernlhr, K., et al. 2017, Monte Carlo performance studies for the site selection of the Cherenkov Telescope Array, Astroparticle Physics, 93, 76

Helfand, D. J., & Becker, R. H. 1987, G0.9 + 0.1 and the emerging class of composite supernova remnants, ApJ, 314, 203

Hess, V. F. 1912, Über Beobachtungen der durchdringenden Strahlung bei sieben Freiballonfahrten, Phys. Z., 13, 1084

Hester, J. J., Stone, J. M., Scowen, P. A., et al. 1996, WFPC2 Studies of the Crab Nebula. III. Magnetic Rayleigh-Taylor Instabilities and the Origin of the Filaments, The Astrophysical Journal, 456, 225

Hester, J. J., Mori, K., Burrows, D., et al. 2002, Hubble Space Telescope and Chandra Monitoring of the Crab Synchrotron Nebula, The Astrophysical Journal, 577, L49

Hillas, A. M. 2013, Evolution of ground-based gamma-ray astronomy from the early days to the Cherenkov Telescope Arrays, Astroparticle Physics, 43, 19

Hinton, J., Sarkar, S., Torres, D., & Knapp, J. 2013, A New Era in Gamma-Ray Astronomy with the Cherenkov Telescope Array, Astroparticle Physics, 43, 1 , seeing the High-Energy Universe with the Cherenkov Telescope Array - The Science Explored with the CTA

Hinton, J. A., & the HESS Collaboration. 2004, The status of the HESS project, New Astronomy Reviews, 48, 331

Hirotani, K. 2006, High-Energy Emission from Pulsar Magnetospheres, Modern Physics Letters A, 21, 1319

Hofverberg, P., Kankanyan, R., Panter, M., et al. 2013, Commissioning and initial performance of the H.E.S.S. II drive system, arXiv e-prints, arXiv:1307.4550

Holder, J. 2014, Ground-Based Gamma Ray Astronomy, Brazilian Journal of Physics, 44, 450

Holler, M., de Naurois, M., Zaborov, D., Balzer, A., & Chalmé-Calvet, R. 2015, in International Cosmic Ray Conference, Vol. 34, 34th International Cosmic Ray Conference (ICRC2015), 980

Janka, H. T., Langanke, K., Marek, A., Martínez-Pinedo, G., & Müller, B. 2007, Theory of core-collapse supernovae, Phys. Rep., 442, 38

Kaspi, V. M., Manchester, R. N., Siegman, B., Johnston, S., & Lyne, A. G. 1994, On the Spin-down of PSR B1509-58, ApJ, 422, L83

Kennel, C. F., & Coroniti, F. V. 1984a, Confinement of the Crab pulsar's wind by its supernova remnant., ApJ, 283, 694

—. 1984b, Magnetohydrodynamic model of Crab nebula radiation., The Astrophysical Journal, 283, 710

Khangulyan, D., Aharonian, F., & Bosch-Ramon, V. 2008, On the formation of TeV radiation in LS 5039, MNRAS, 383, 467

Kieda, D., & Matthews, N. 2017, Stellar Intensity Interferometric Capabilities of IACT Arrays, International Cosmic Ray Conference, 301, 828

Kieda, D. B., Anton, G., Barbano, A., et al. 2019, Astro2020 White Paper State of the Profession: Intensity Interferometry, arXiv e-prints, arXiv:1907.13181

Kirk, J. G., & Lyubarsky, D. Y. 2001, Reconnection in Pulsar Winds, Publications of the Astronomical Society of Australia, 18, 415

Kistler, M. D. 2015, A Tale of Two Pulsars and the Origin of TeV Gamma Rays from the Galactic Center, ArXiv e-prints, arXiv:1511.01159

Knödlseder, J., Mayer, M., Deil, C., et al. 2016, GammaLib and ctools. A software framework for the analysis of astronomical gamma-ray data, A&A, 593, A1

Komissarov, S. S. 2002, Time-dependent, force-free, degenerate electrodynamics, Monthly Notices of the Royal Astronomical Society, 336, 759

Koo, B.-C., McKee, C. F., Suh, K.-W., et al. 2011, IRAS 15099-5856: Remarkable Mid-infrared Source with Prominent Crystalline Silicate Emission Embedded in the Supernova Remnant MSH15-52, ApJ, 732, 6

Kuiper, L., Hermsen, W., Krijger, J. M., et al. 1999, COMPTEL detection of pulsed gamma -ray emission from PSR B1509-58 up to at least 10 MeV, A&A, 351, 119

La Palombara, N., Agnetta, G., Antonelli, L. A., et al. 2013, The ASTRI Project: a mini-array of dual-mirror small Cherenkov telescopes for CTA, arXiv e-prints, arXiv:1304.6559

Li, H., Chen, Y., & Zhang, L. 2010, Lepto-hadronic origin of γ-rays from the G54.1+0.3 pulsar wind nebula, MNRAS, 408, L80

Linden, T., Auchettl, K., Bramante, J., et al. 2017a, Using HAWC to discover invisible pulsars, Phys. Rev. D, 96, 103016

—. 2017b, Using HAWC to discover invisible pulsars, Phys. Rev. D, 96, 103016

Liu, Q., & Kheirandish, A. 2019, in International Cosmic Ray Conference, Vol. 36, 36th International Cosmic Ray Conference (ICRC2019), 944

Livingstone, M. A., & Kaspi, V. M. 2011, Long-term X-Ray Monitoring of the Young Pulsar PSR B1509-58, ApJ, 742, 31

Livingstone, M. A., Kaspi, V. M., Gavriil, F. P., & Manchester, R. N. 2005, 21 Years of Timing PSR B1509-58, ApJ, 619, 1046

Lombardi, S., Antonelli, L. A., Bigongiari, C., et al. 2018, in Society of Photo-Optical Instrumentation Engineers (SPIE) Conference Series, Vol. 10707, Proc. SPIE, 107070R

Lombardi, S., & The ASTRI Collaboration. in prep., First detection of the Crab Nebula at TeV energies with a Cherenkov telescope in dual-mirror Schwarzschild-Couder configuration: the ASTRI-Horn telescope, Astronomy and Astrophysics

Longair, M. S. 2008, Galaxy Formation (Cambridge university press)

—. 2011, High Energy Astrophysics (Cambridge university press)

Lopez-Coto, R. 2015, PhD thesis, Universitat Autonoma de Barcelona

López Moya, M. 2019, Detection of the Geminga pulsar with MAGIC, International Cosmic Ray Conference, 36, 728

Lortet, M. C., Georgelin, Y. P., & Georgelin, Y. M. 1987, The region of the supernova remnant MSH 15-52 revisited : a new thermal H II region, H II G320.5-1.4., A&A, 180, 65

Lu, F.-W., Gao, Q.-G., & Zhang, L. 2017, A Self-consistent and Spatially Dependent Model of the Multiband Emission of Pulsar Wind Nebulae, ApJ, 834, 43

Lyubarskii, Y. E. 1996, A model for the energetic emission from pulsars., Astronomy and Astrophysics, 311, 172

Lyubarsky, Y. E. 2002, On the structure of the inner Crab Nebula, Monthly Notices of the Royal Astronomical Society, 329, L34

—. 2003, The termination shock in a striped pulsar wind, Monthly Notices of the Royal Astronomical Society, 345, 153

Lyutikov, M., Otte, N., & McCann, A. 2012, The Very High Energy Emission from Pulsars: A Case for Inverse Compton Scattering, ApJ, 754, 33

Maccarone, M. C., & Astri Project, C. 2017, ASTRI for the Cherenkov Telescope Array, International Cosmic Ray Conference, 301, 855

Maier, G., Arrabito, L., Bernlöhr, K., et al. 2017, Performance of the Cherenkov Telescope Array, International Cosmic Ray Conference, 301, 846

Manchester, R. N., Hobbs, G. B., Teoh, A., & Hobbs, M. 2005, The Australia Telescope National Facility Pulsar Catalogue, AJ, 129, 1993

Manchester, R. N., Tuohy, I. R., & Damico, N. 1982, Discovery of radio pulsations from the X-ray pulsar in the supernova remnant G320.4-1.2, ApJ, 262, L31

Marsden, D., Blanco, P. R., Gruber, D. E., et al. 1997, The X-Ray Spectrum of the Plerionic System PSR B1509−58/MSH 15−52, ApJ, 491, L39

Martín, J., Torres, D. F., & Pedaletti, G. 2016, Molecular environment, reverberation, and radiation from the pulsar wind nebula in CTA 1, MNRAS, 459, 3868

Martín, J., Torres, D. F., & Rea, N. 2012, Time-dependent modelling of pulsar wind nebulae: study on the impact of the diffusion-loss approximations, MNRAS, 427, 415

Mayer, M., Brucker, J., Holler, M., et al. 2012, Predicting the X-ray flux of evolved pulsar wind nebulae based on VHE gamma-ray observations, arXiv e-prints, arXiv:1202.1455

Mazin, D., Cortina, J., & Teshima, M. 2017, in American Institute of Physics Conference Series, Vol. 1792, 6th International Symposium on High Energy Gamma-Ray Astronomy, 080001

Meyer, M., Horns, D., & Zechlin, H. S. 2010, The Crab Nebula as a standard candle in very high-energy astrophysics, A&A, 523, A2

Michel, F. C. 1973, Rotating Magnetospheres: an Exact 3-D Solution, The Astrophysical Journal, 180, L133

—. 1994, Magnetic Structure of Pulsar Winds, The Astrophysical Journal, 431, 397

Mineo, T., Cusumano, G., Maccarone, M. C., et al. 2001, The hard X-ray emission from the complex SNR MSH 15-52 observed by BeppoSAX, A&A, 380, 695

Mirzoyan, R. 2019, First time detection of a GRB at sub-TeV energies; MAGIC detects the GRB 190114C, The Astronomer's Telegram, 12390, 1

Mochol, I. 2017, in Astrophysics and Space Science Library, Vol. 446, Modelling Pulsar Wind Nebulae, ed. D. F. Torres, 135

Montaruli, T., Pareschi, G., & Greenshaw, T. 2015, The small size telescope projects for the Cherenkov Telescope Array, arXiv e-prints, arXiv:1508.06472

Müller, B. 2017, in IAU Symposium, Vol. 329, The Lives and Death-Throes of Massive Stars, ed. J. J. Eldridge, J. C. Bray, L. A. S. McClelland, & L. Xiao, 17–24

Muslimov, A. G., & Harding, A. K. 2003, Extended Acceleration in Slot Gaps and Pulsar High-Energy Emission, ApJ, 588, 430

—. 2004, High-Altitude Particle Acceleration and Radiation in Pulsar Slot Gaps, The Astrophysical Journal, 606, 1143

Muzzio, J. C., & Celotti de Frecha, M. B. 1979, Faint early-type stars in the neighbourhood of the H II region RCW 38., MNRAS, 189, 159

Nakamori, T., Kubo, H., Yoshida, T., et al. 2008, Observation of an Extended Very High Energy Gamma-Ray Emission from MSH 15-52 with CANGAROO-III, ApJ, 677, 297

Nakamori, T., Katagiri, H., Sano, H., et al. 2015, in 34th International Cosmic Ray Conference (ICRC2015), Vol. 34, 774

Olmi, B., & Bucciantini, N. 2019, Full-3D relativistic MHD simulations of bow shock pulsar wind nebulae: dynamics, Monthly Notices of the Royal Astronomical Society, 484, 5755

Ong, R., & CTA Consortium. 2017, Cherenkov Telescope Array: The Next Generation Gamma-ray Observatory, International Cosmic Ray Conference, 301, 1071

Ostriker, J. P., & Gunn, J. E. 1971, Do Pulsars Make Supernovae?, ApJ, 164, L95

Pacini, D. 1912, La radiazione penetrante alla superficie ed in seno alle acque, Il Nuovo Cimento (1911-1923), 3, 93

Pacini, F., & Salvati, M. 1973, On the Evolution of Supernova Remnants. Evolution of the Magnetic Field, Particles, Content, and Luminosity, ApJ, 186, 249

Paredes, J. M., Bednarek, W., Bordas, P., et al. 2013, Binaries with the eyes of CTA, Astroparticle Physics, 43, 301

Pareschi, G. 2016, in Society of Photo-Optical Instrumentation Engineers (SPIE) Conference Series, Vol. 9906, Proc. SPIE, 99065T

Pareschi, G., Agnetta, G., Antonelli, L. A., et al. 2013, The dual-mirror Small Size Telescope for the Cherenkov Telescope Array, arXiv e-prints, arXiv:1307.4962

Park, N., & VERITAS Collaboration. 2015, in 34th International Cosmic Ray Conference (ICRC2015), Vol. 34, 771

Pétri, J. 2013, Phase-resolved polarization properties of the pulsar striped wind synchrotron emission, Monthly Notices of the Royal Astronomical Society, 434, 2636

—. 2016, Theory of pulsar magnetosphere and wind, Journal of Plasma Physics, 82, 635820502

Pierre Auger Collaboration, Allekotte, I., Barbosa, A. F., et al. 2008, The surface detector system of the Pierre Auger Observatory, Nuclear Instruments and Methods in Physics Research A, 586, 409

Pintore, F., & The ASTRI Collaboration. in prep., Scientific prospects for the ASTRI mini-arry: a data challenge, Astronomy and Astrophysics

Popescu, C. C., Yang, R., Tuffs, R. J., et al. 2017, A radiation transfer model for the Milky Way: I. Radiation fields and application to high-energy astrophysics, MNRAS, 470, 2539

Porquet, D., Decourchelle, A., & Warwick, R. S. 2003, XMM-Newton spectral analysis of the Pulsar Wind Nebula within the composite SNR G0.9+0.1, A&A, 401, 197

Porter, T. A., Moskalenko, I. V., & Strong, A. W. 2006, Inverse Compton Emission from Galactic Supernova Remnants: Effect of the Interstellar Radiation Field, ApJ, 648, L29

Porth, O., Komissarov, S. S., & Keppens, R. 2014, Rayleigh-Taylor instability in magnetohydrodynamic simulations of the Crab nebula, MNRAS, 443, 547

Prandini, E. 2017, Highlights from TeV Extragalactic Sources, arXiv e-prints, arXiv:1706.01670

Pühlhofer, G. 2017, in American Institute of Physics Conference Series, Vol. 1792, 6th International Symposium on High Energy Gamma-Ray Astronomy, 080002

Qiao, W.-F., Zhang, L., & Fang, J. 2009, Non-thermal emission from Vela X and PWN G0.9+0.1, Research in Astronomy and Astrophysics, 9, 449

Reynolds, S. P., & Chevalier, R. A. 1984, Evolution of pulsar-driven supernova remnants., The Astrophysical Journal, 278, 630

Rieger, F. M., de Oña-Wilhelmi, E., & Aharonian, F. A. 2013, TeV astronomy, Frontiers of Physics, 8, 714

Rodgers, A. W., Campbell, C. T., & Whiteoak, J. B. 1960, A catalogue of Hα-emission regions in the southern Milky Way, MNRAS, 121, 103

Romani, R. W., & Yadigaroglu, I. A. 1995, Gamma-Ray Pulsars: Emission Zones and Viewing Geometries, The Astrophysical Journal, 438, 314

Ruderman, M. A., & Sutherland, P. G. 1975, Theory of pulsars: polar gaps, sparks, and coherent microwave radiation., The Astrophysical Journal, 196, 51

Rybicki, G. B., & Lightman, A. P. 1979, Radiative processes in astrophysics (John Wiley & Sons, Inc.)

Scharlemann, E. T., & Wagoner, R. V. 1973, Aligned Rotating Magnetospheres. General Analysis, The Astrophysical Journal, 182, 951

Schöck, F. M., Büsching, I., de Jager, O. C., Eger, P., & Vorster, M. J. 2010, Spatially resolved XMM-Newton analysis and a model of the nonthermal emission of MSH 15-52, A&A, 515, A109

Scuderi, S. 2018, in Society of Photo-Optical Instrumentation Engineers (SPIE) Conference Series, Vol. 10700, Proc. SPIE, 107005Z

Scuderi, S. 2019, in European Physical Journal Web of Conferences, Vol. 209, European Physical Journal Web of Conferences, 01001

Sedov, L. I. 1959, Similarity and Dimensional Methods in Mechanics (New York: Academic press)

Seward, F. D., & Harnden, Jr., F. R. 1982, A new, fast X-ray pulsar in the supernova remnant MSH 15-52, ApJ, 256, L45

Seward, F. D., Harnden, F. R., J., Murdin, P., & Clark, D. H. 1983, MSH 15-52 : a supernova remnant containing two compact X-ray sources., ApJ, 267, 698

Sheidaei, F. 2011, in International Cosmic Ray Conference, Vol. 7, International Cosmic Ray Conference, 244

Sierpowska-Bartosik, A., & Torres, D. F. 2008, Pulsar wind zone processes in LS 5039, Astroparticle Physics, 30, 239

Sironi, L., & Spitkovsky, A. 2011, Acceleration of Particles at the Termination Shock of a Relativistic Striped Wind, The Astrophysical Journal, 741, 39

Slane, P. 2005, The devil is in the details: Compact structures in pulsar wind nebulae, Advances in Space Research, 35, 1092

Slane, P. 2008, in American Institute of Physics Conference Series, Vol. 1085, American Institute of Physics Conference Series, ed. F. A. Aharonian, W. Hofmann, & F. Rieger, 120–128

—. 2017, Pulsar Wind Nebulae (Handbook of Supernovae, Springer International Publishing), 2159

Smith, A. W., & the VERITAS Collaboration. 2015, VERITAS Observations of The Galactic Center Ridge, ArXiv e-prints, arXiv:1508.06311

Spitkovsky, A., & Arons, J. 2004, Time Dependence in Relativistic Collisionless Shocks: Theory of the Variable "Wisps" in the Crab Nebula, The Astrophysical Journal, 603, 669

Spurio, M. 2018, Probes of Multimessenger Astrophysics (Springer), doi:10.1007/978-3-319-96854-4

Stecker, F. W., de Jager, O. C., & Salamon, M. H. 1992, TeV Gamma Rays from 3C 279: A Possible Probe of Origin and Intergalactic Infrared Radiation Fields, ApJ, 390, L49

Sturrock, P. A. 1971, A Model of Pulsars, The Astrophysical Journal, 164, 529

Sudoh, T., Linden, T., & Beacom, J. F. 2019, TeV halos are everywhere: Prospects for new discoveries, Phys. Rev. D, 100, 043016

Tamura, K., Kawai, N., Yoshida, A., & Brinkmann, W. 1996, Evidence for a Pulsar Jet Producing a Hot Nebula in the Supernova Remnant MSH 15-52, PASJ, 48, L33

Tanaka, S. J., & Takahara, F. 2010, A Model of the Spectral Evolution of Pulsar Wind Nebulae, ApJ, 715, 1248

—. 2011, Study of Four Young TeV Pulsar Wind Nebulae with a Spectral Evolution Model, ApJ, 741, 40

Tauris, T. M., & van den Heuvel, E. P. J. 2006, Formation and evolution of compact stellar X-ray sources, Vol. 39 (Cambridge Astrophysics Series), 623–665

Tavani, M., Bulgarelli, A., Vittorini, V., et al. 2011, Discovery of Powerful Gamma-Ray Flares from the Crab Nebula, Science, 331, 736

Taylor, G. 1950, The Formation of a Blast Wave by a Very Intense Explosion. I. Theoretical Discussion, Proceedings of the Royal Society of London Series A, 201, 159

Tchekhovskoy, A., Spitkovsky, A., & Li, J. G. 2013, Time-dependent 3D magnetohydrodynamic pulsar magnetospheres: oblique rotators., Monthly Notices of the Royal Astronomical Society, 435, L1

The Milagro Collaboration. 2001, Status of the Milagro Gamma Ray Observatory, arXiv e-prints, astro

Tibolla, O., Komin, N., Kosack, K., & Naumann-Godo, M. 2008, in American Institute of Physics Conference Series, Vol. 1085, American Institute of Physics Conference Series, ed. F. A. Aharonian, W. Hofmann, & F. Rieger, 249–252

Timokhin, A. N., & Harding, A. K. 2015, On the Polar Cap Cascade Pair Multiplicity of Young Pulsars, The Astrophysical Journal, 810, 144

Torres, D. F., Cillis, A., Martín, J., & de Oña Wilhelmi, E. 2014, Time-dependent modeling of TeV-detected, young pulsar wind nebulae, Journal of High Energy Astrophysics, 1, 31

Torres, D. F., Cillis, A. N., & Martín Rodriguez, J. 2013a, An Energy-conserving, Particle-dominated, Time-dependent Model of 3C 58 and Its Observability at High Energies, ApJ, 763, L4

Torres, D. F., Lin, T., & Coti Zelati, F. 2019, Towards observing reverberating and superefficient pulsar wind nebulae, Monthly Notices of the Royal Astronomical Society, 486, 1019

Torres, D. F., Martín, J., de Oña Wilhelmi, E., & Cillis, A. 2013b, The effects of magnetic field, age and intrinsic luminosity on Crab-like pulsar wind nebulae, MNRAS, 436, 3112

Truelove, J. K., & McKee, C. F. 1999, Evolution of Nonradiative Supernova Remnants, The Astrophysical Journal Supplement Series, 120, 299

Trussoni, E., Massaglia, S., Caucino, S., Brinkmann, W., & Aschenbach, B. 1996, ROSAT PSPC observations of the supernova remnant MSH 15-52., A&A, 306, 581

Tsirou, M., Gallant, Y. A., Terrier, R., et al. 2018, in 42nd COSPAR Scientific Assembly, Vol. 42, E1.5–107–18

van der Swaluw, E. 2003, Interaction of a magnetized pulsar wind with its surroundings. MHD simulations of pulsar wind nebulae, Astronomy and Astrophysics, 404, 939

Van Der Swaluw, E., Achterberg, A., & Gallant, Y. A. 1998, Hydrodynamical simulations of pulsar wind nebulae in supernova remnants, Memorie della Societa Astronomica Italiana, 69, 1017

van der Swaluw, E., Achterberg, A., Gallant, Y. A., & Tóth, G. 2001, Pulsar wind nebulae in supernova remnants. Spherically symmetric hydrodynamical simulations, A&A, 380, 309

van der Swaluw, E., Downes, T. P., & Keegan, R. 2004, An evolutionary model for pulsar-driven supernova remnants. A hydrodynamical model, A&A, 420, 937

van Rensburg, C., Krüger, P. P., & Venter, C. 2018, Spatially dependent modelling of pulsar wind nebula G0.9+0.1, MNRAS, 477, 3853

Vassiliev, V., Fegan, S., & Brousseau, P. 2007, Wide field aplanatic two-mirror telescopes for ground-based γ-ray astronomy, Astroparticle Physics, 28, 10

Venter, C. 2016, in Proceedings of the 4th Annual Conference on High Energy Astrophysics in Southern Africa (HEASA 2016). 25-26 August, 40

Venter, C., & de Jager, O. C. 2007, in WE-Heraeus Seminar on Neutron Stars and Pulsars 40 years after the Discovery, ed. W. Becker & H. H. Huang, 40

Vercellone, S. 2017, in American Institute of Physics Conference Series, Vol. 1792, 6th International Symposium on High Energy Gamma-Ray Astronomy, 030001

Vercellone, S., Agnetta, G., Antonelli, L. A., et al. 2013, The ASTRI Mini-Array Science Case, arXiv e-prints, arXiv:1307.5671

VERITAS collaboration. 2019, VERITAS public performance, https://veritas.sao.arizona.edu/about-veritas-mainmenu-81/veritas-specifications-mainmenu-111

VERITAS Collaboration, Aliu, E., Arlen, T., et al. 2011, Detection of Pulsed Gamma Rays Above 100 GeV from the Crab Pulsar, Science, 334, 69

Vorster, M. J., Tibolla, O., Ferreira, S. E. S., & Kaufmann, S. 2013, Time-dependent Modeling of Pulsar Wind Nebulae, ApJ, 773, 139

Wagner, R. M. 2006, PhD thesis, Munich, Tech. U.

Wakely, S. P., & Horan, D. 2008, TeVCat: An online catalog for Very High Energy Gamma-Ray Astronomy, International Cosmic Ray Conference, 3, 1341

Weekes, T. C., Cawley, M. F., Fegan, D. J., et al. 1989, Observation of TeV Gamma Rays from the Crab Nebula Using the Atmospheric Cerenkov Imaging Technique, ApJ, 342, 379

Weiler, K. W., & Panagia, N. 1978, Are Crab-type Supernova Remnants (Plerions) Short-lived?, A&A, 70, 419

Wenger, M., Ochsenbein, F., Egret, D., et al. 2000, The SIMBAD astronomical database. The CDS reference database for astronomical objects, A&AS, 143, 9

Werner, M., Kissmann, R., Strong, A. W., & Reimer, O. 2015, Spiral arms as cosmic ray source distributions, Astroparticle Physics, 64, 18

Whiteoak, J. B. Z., & Green, A. J. 1996, The MOST supernova remnant catalogue (MSC)., A&AS, 118, 329

Wilkin, F. P. 1996, Exact Analytic Solutions for Stellar Wind Bow Shocks, The Astrophysical Journal, 459, L31

Wulf, T. 1909, On the radiation of high penetrating power that exists in the atmosphere, Phys. Zeit, 1, 124

Yao, J. M., Manchester, R. N., & Wang, N. 2017, A New Electron-density Model for Estimation of Pulsar and FRB Distances, ApJ, 835, 29

Yatsu, Y., Kawai, N., Shibata, S., & Brinkmann, W. 2009, Discovery of the Inner Ring around PSR B1509-58, PASJ, 61, 129

Zanin, R. 2017, in Modelling Pulsar Wind Nebulae, ed. D. F. Torres, Vol. 446, 101

Zhang, L., Chen, S. B., & Fang, J. 2008, Nonthermal Radiation from Pulsar Wind Nebulae, ApJ, 676, 1210

Zhu, B.-T., Fang, J., & Zhang, L. 2015, Revisiting the non-thermal radiation from the Crab nebula: requiring two distinct electron components, MNRAS, 451, 3145

Zhu, B.-T., Zhang, L., & Fang, J. 2018, Multiband nonthermal radiative properties of pulsar wind nebulae, A&A, 609, A110